METAMATERIAL LOADING OF ELECTRICALLY SMALL PATCH ANTENNAS TO ENABLE BEAM STEERING UP TO THE HORIZON

by

Vandita Rajiv Pai Raikar

A thesis submitted to the faculty of
The University of North Carolina at Charlotte
in partial fulfillment of the requirements
for the degree of Master of Science in
Electrical Engineering

Charlotte

2015

Approved by:

_____
Dr. Ryan S. Adams

_____
Dr. T.P. Weldon

_____
Dr. Asis Nasipuri

ABSTRACT

VANDITA RAJIV PAI RAIKAR. Metamaterial loading of electrically small patch antennas to enable beam steering up to the horizon. (Under the direction of DR. RYAN S. ADAMS)

This thesis research has been conducted with an aim of investigating the effects of metamaterials on microstrip patch antennas. Metamaterials exhibit interesting properties such as single negative or simultaneous double negative values of relative permittivity and permeability, due to which they have gained immense popularity. The influence of metamaterials on traditional patch antennas has been a topic of focus throughout this research. Different metamaterial unit cells have been designed to possess satisfactory behavior in terms of permittivity and permeability. The use of metamaterials as a substrate for patch antennas has been explored, highlighting the possibility of designing electrically small patch antennas. Several metamaterial unit cells and modified patch antennas have been designed and modeled in Ansys HFSS, a highly competent full wave electromagnetic solver. On achieving a satisfactory results from a single patch antenna, the same concept has been applied to design a planar phased array patch antenna having 8×8 elements. The planar phased array antenna will be designed to enable beam steering from broadside toward the horizon.

ACKNOWLEDGEMENTS

I would like to acknowledge a lot of near and dear ones for the successful completion of my Masters thesis. But first, I would like to thank God Almighty without whom nothing is impossible. I would like to thank Him for all the happy and challenging moments in my life, for showing me light when there was no hope, for providing me with wonderful opportunities which have made me the person I am today.

I would like to sincerely thank the faculty of William States Lee College of Engineering for letting me fulfill my dream of pursing a Masters degree in Electrical engineering. I am especially grateful to my adviser Dr. Ryan S. Adams, who has been an exceptionally amazing mentor to me through out my graduate studies, whose constant guidance and encouragement helped carve this research. I am greatly thankful to Dr. Adams for providing me the opportunity of conducting research under him.

I would like to extend my deepest gratitude towards Dr. Thomas Weldon and Dr. Asis Nasipuri, who took time from their busy schedules to review my research.

I am forever indebted to my parents Rajiv and Manju for providing me with a comfortable life and the best education. I would like to show my appreciation to them for supporting me financially and morally especially while I was pursuing my masters degree.

I am obligated towards the Pai Kane family, who provided me with a home, miles away from home.

I would like to thank my colleagues from the Electromagnetic devices lab; Kathryn, Omar, Varun who have helped and adviced me whenever I needed them. I would also extend my appreciation towards my friends outside the Lab; Anusha, Karishma, Gatha, Uday, Adithya and my sister Varada who have constantly motivated me.

DEDICATION

To my parents,

I am what I am today because of all that you have sacrificed for me. Thank you so much for your constant support and motivation.

I will always love you.

TABLE OF CONTENTS

LIST OF FIGURES

LIST OF TABLES

LIST OF ABBREVIATIONS

DPS	Double Positive
DNG	Double Negative
SNG	Single Negative
ENG	Epsilon Negative
MNG	Mu-Negative
PEC	Perfect Electrical Conductor
PMC	Perfect Magnetic Conductor
EM	Electromagnetic
HFSS	High Frequency Structural Simulator
CLS	Capacitively Loaded Strip
ESA	Electrically Small Antenna
CSRR	Complimentary Split Ring Resonator
DSRR	Double Split Ring Resonator

CHAPTER 1: INTRODUCTION

Communication between electronic devices require a transmission medium to carry information between the receiver and transmitter. Communication channels that facilitate this transfer of energy maybe guided like transmission line or optical fiber or wireless such as air (or free space). The proliferation of cellular networks, wireless sensor networks and wireless data networks such as WiFi or Bluetooth and other technologies has led to crowding of signals in free space. To distinguish between signals travelling in free space, a distinct range of frequencies is assigned to each signal, depending on the application that generates them. The largest possible range of frequencies over which the free space medium can be used is called as the Electromagnetic spectrum and is broadly divided into the following regions:

1. Radio frequency (3 kHz - 300 GHz)
2. Microwave frequency (300 MHz - 300 GHz)
3. Terahertz frequency (300 GHz - 3 THz)
4. Infrared(300 GHz - 430 THz)
5. Visible Light (430 THz - 770 THz)
6. Ultraviolet (800 THz - 30 PHz)
7. X-rays (30 PHz - 30 EHz)
8. Gamma rays (30 EHz and higher)

The radio frequency region in the electromagnetic spectrum is further broken down into smaller frequency regions to be used in different applications such as Wireless

LAN, cellular networks, GPS, GSM and bluetooth to name a few. The most popular frequency bands in the radio frequency region are outlined in Table 1.1 along with specific applications in each band.

Table 1.1: Standard frequency bands and their uses

Frequency Band	Frequency Range	Application
Low frequency	30-300kHz	AM longwave broadcasting, RFID, Amateur radio
Medium frequency	300-3000kHz	AM mediumwave broadcasting, Avalanche beacons, Amateur radio
High frequency	3-30MHz	AM shortwave broadcasting, Military and government communication systems, over the horizon radar systems
Very High frequency	30-300MHz	FM radio and television broadcasting, long range data communication, land mobile radio systems
Ultra High frequency	300-3000MHz	Microwave devices and communication,mobile phones, wireless LAN, Bluetooth, ZigBee, GPS, amateur radio

Because of significant crowding within these established frequency bands, a need has arisen to explore less crowded regions of the spectrum. One significant factor that limits the use of lower frequency bands is the antenna that plays a crucial role in transmission and reception. For optimal performance of the antenna, its overall size increases as the operating frequency decreases. So, operation at lower frequencies can lead to utilization of bulky antenna structures.

However, new advancements in handset technologies has resulted in a drastic reduction in the size and weight of the device as a whole and hence, antennas that are incorporated in these handheld devices are required to be correspondingly smaller than in previous technology. This conflict (larger antenna but smaller handsets) suggests that alternative antenna options must be pursued.

One popular antenna topology, that has been extensively employed in wireless systems, is the microstrip patch. Microstrip antennas were first discussed by Deschamps

in 1953 [11] and have been heavily researched ever since. Such an antenna topology consists of a metal patch placed at a height above a large ground plane separated by a dielectric substrate. Microstrip antennas exhibit many benefits such as lightweight, inexpensive, easy integration with other microstrip circuits, easily fed and simple fabrication methods. Typical patch antennas are half wavelength long at the operating frequency. This leads to size problems at lower frequencies, as previously discussed. Some researchers have presented methods to reduce antenna size without significantly sacrificing performance. One such method suggests that one edge of the metal patch should be shorted to the ground plane to add an inductive and capacitive component to the antenna structure [10] . The resulting antenna was a quarter wavelength in size. While this improvement is useful, it is not sufficient to viably integrate into low-frequency devices that require revolutionary size reduction.

1.1 Background

The primary aim of this research has been to find a technique that would lead to a dramatic reduction in the size of the patch antenna. To achieve this reduction in size of the antenna structure, the concept of metametarials was explored. From previous literature, it can be learned that research on metamaterials began in the 19th century, when Jagdish Chandra Bose conducted the first experiment on twisted structures which were referred to as chiral media [30]. Following this work, another scientist, Karl F. Lindman, synthesized microwave chiral media embedding small helices from copper wire in a cardboard box with random orientation [16]. Research on metamaterials resumed just after World War II with research mainly focusing on artificial dielectrics in the microwave regime for antenna beam shaping. Research on periodic artificial structures by W.E Kock and Sergei Schelkunoff among others, achieved prominence due to its contribution to antenna theory [1] [13] [24]. W.E Kock also conducted studies on metallic delay lenses and wire lens antennas thus providing insights on lightweight metallic microwave lens antennas.

The occurrence of simultaneous negative values of permittivity and permeability was much later explored theoretically by Victor Veselago in 1964. He investigated the propagation of a plane monochromatic wave through a double negative material, which resulted in his conclusion that the direction of the Poynting vector is antiparallel to the direction of the phase velocity. Inspired from Veselago's research, many scientists attempted to create such materials that possessed negative values of μ and ϵ. One such researcher was John Pendry, who along with his colleagues attempted to develop materials with negative permeability. Pendry was able to achieve negative permeability using an array of metallic cylinders and metal hoops, which were later simplified into split ring resonators [22]. Pendry also successfully managed to create negative permittivity when an electric field was applied parallel to an array of thin metallic wires [21]. Following Pendry's research on split rings and metallic wires, Smith and his colleagues at the University of California, San Diego presented a composite medium of split ring resonators printed on a dielectric substrate and an array of metallic posts that together exhibited simultaneous double negative values of permittivity and permeability [25]. Another scientist R.W Ziolkowski suggested different geometries such as rectangular split rings and capacitively loaded strips and a combination of the two geometries that exhibited double negative properties. He also presented novel methods to extract these double negative properties from these metamaterial cells [32].

The notion of metamaterials appeals to the concept of macroscopic electromagnetism as formulated in the constitutive parameters ϵ_r and μ_r. The formation of these parameters assumes the discrete charges and currents that are associated with individual electrons and molecules are electrically very small, and a bulk material made up of these particles can be treated as a uniform continuous material. In a similar way, meta-atoms and meta-molecules can be formed that are electrically small, but are large enough that they can be rigorously designed and built of common ma-

terials like metals and dielectrics. For a material made of these meta-particles to operate in a similar way to standard dielectrics, the particles must be electrically small, or less than $\lambda/10$.

Since meta-particles can be designed for a particular purpose, it is possible to design a particular value of ϵ_r and/or μ_r for a given purpose. In fact, values of $\epsilon_r < 0$ and $\mu_r < 0$ are possible, even though they are not generally attainable in nature. Such a material has been shown to exhibit backward propagation in which the phase velocity of a wave propagating through it moves in a direction opposite to the direction of power flow. Such materials are the enabling technology for such devices as invisibility cloaks and ideal flat lenses.

1.2 Related Work

Metamaterials have been used in conjunction with microstrip patch antennas in order to achieve different objectives such as size reduction [5], gain enhancement [18] and bandwidth enhancement [19]. To accomplish such goals, metamaterial unit cells have been integrated into the substrate region beneath the patch or as a superstrate over the patch. Metamaterials have also been integrated into the ground plane of patch elements with the aim of improving the gain and/or the bandwidth of the antenna.

Recent research conducted by Andrea Al$\grave{u}$ et al. suggested a novel method wherein the dielectric substrate beneath the patch was partially replaced by an SNG or a DNG material [5]. The ratio of the DPS to DNG filling beneath the patch determined the limitation on how much the patch could be reduced in dimension. Following Al$\grave{u}$'s research, Mahdy and his colleagues [17] developed an algorithm that helped in optimizing the DPS To DNG/SNG filling ratio leading to a desirably miniaturized patch antenna.

In addition to miniaturization, other aspects of patch antenna performance improvement by utilizing the properties of metamaterials were explored by many other

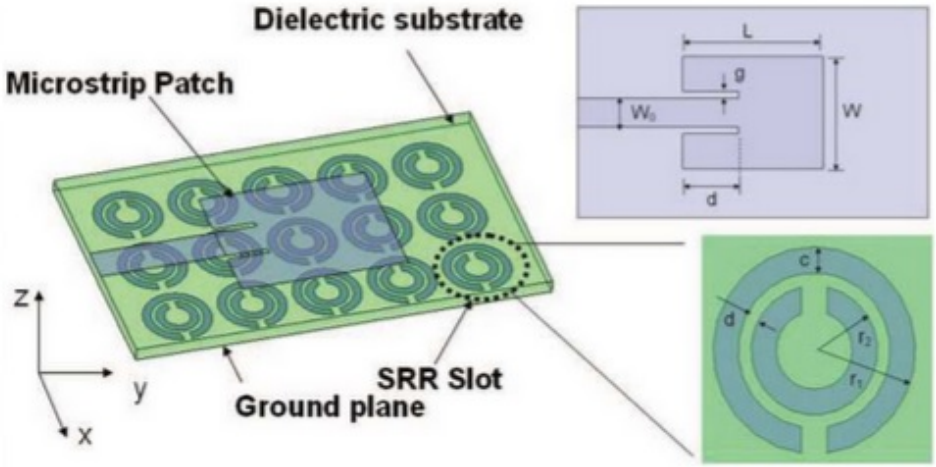

Figure 1.1: Patch antenna with CSRR loaded ground plane [14]

authors. One such publication explores the idea of replacing a solid metal ground plane with a ground plane periodically etched with complimentary split ring resonators (CSRR) [14]. The authors of this paper continued to use a positive dielectric slab while loading the ground plane with CSRR. Thus, etching out split rings from the copper ground plane resulted in an improved bandwidth when compared to a traditional patch antenna. Along with bandwith enhancement, the patch antenna structure achieved a significant size reduction and an interesting zeroth order resonance.

Additionally, metamaterials have also been used as a superstrate placed over the patch element. Arrays of double negative materials have been placed above a patch element and have been found to improve antenna performance. One such publication proposed a combination of rectangular split ring resonators and capacitively loaded strips that exhibit negative values of ϵ_r and μ_r [18]. Rows of these DNG unit cells were placed above a microstrip patch antenna. These rows of metamaterials placed above the patch element behave as a superstrate for the antenna model. The gain of the antenna was observed to have increased significantly owing to the addition of

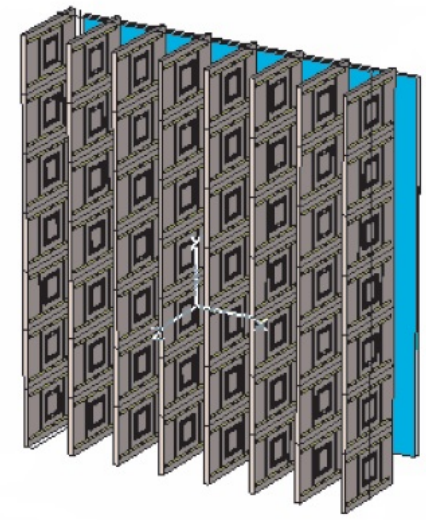

Figure 1.2: Patch antenna with DNG metamaterial used as superstrate [18]

a metamaterial superstrate layer. In addition to gain enhancement, the bandwidth of the patch antenna was also improved in comparison to a traditional patch. This interesting antenna structure consisting of a metamaterial superstrate is displayed Fig.1.2.

From the above discussion it can be noted that the influence of metamaterials on patch antennas can demonstrate significant improvement in antenna performance. The most notable effect of integration of these novel metamaterial structures is the reduction in patch sizes. This significant reduction in dimensions has led to the possibility of production of electrically small patch antennas. Achieving this size reduction is one step forward towards increasing the demand for patches in mobile handheld devices. The next section in this chapter discusses electrically small antennas and their fundamental limitations in detail.

1.3 Electrically Small Antennas

H.A. Wheeler defined a small antenna as an antenna structure occupying a small fraction of one raidansphere in space [31]. A radiansphere is the spherical volume having a radius of $1/2\pi$ wavelength, and is generally the space around the antenna

that contains its stored electric and magnetic field. Many examples of electrically small antennas have been proposed and discussed in the literature. [2]. These antennas typically have a dominant reactive component that is either capacitive or inductive and a small real component. The simplest electrically small antenna topology is a small electric dipole, which is a linear wire antenna with length less than $\lambda/10$. The input impedance associated with this antenna has a finite reactive component and a small resistive component. Being electrically small, the gain and directivity of the short dipole is much smaller when compared than a half wavelength dipole. Another popular example of an electrically small antenna is a circular loop antenna, whose radius is very much smaller than a wavelength.

One major challenge in the design of an electrically small antenna was discussed by Chu [15] in which he stated a relationship between antenna size, antenna gain and efficiency. Chu explained that it is not always possible to achieve small antenna size, high gain and low loss simultaneously. Thus small antennas exhibit either low gain or high loss. However, the challenge of achieving adequate gain with small antennas can be overcome, when these electrically small tuned antennas are arranged as a set of multiple antennas preferably with a factor of 2 in the form of an array. This technique of placing the individual small antenna elements in close proximity can appear very promising in communication and radar systems. However, the biggest limitation faced by these equally appealing electrically small antenna array is due to its narrowband impedance response. In practice, each individual small antenna element is characterized by a high reactive component and a low radiation resistance, which brings out the need to add a matching network to cancel out its reactance. But, with the advent of non-Foster circuits and its employment for the development of matching networks exhibiting negative reactive components, this limitation can also be overcome to some extent.

1.3.1 Objective and Structure of Thesis

This thesis broadly discusses two main topics; metamaterials and electrically small patch antennas. This research mainly attempts to produce an electrically small microstrip patch antenna by utilizing metamaterials. Peculiar properties possessed by metamaterials were studied and attempted to be integrated into the patch antenna topology. Single microstrip patch antennas were developed in conjunction with the different meta-structures that were designed. Once satisfactory patch antenna models were designed, the same concept was extended to develop a patch antenna array that would exhibit a much higher gain and also produce a narrow main beam, that can be steered from broadside toward the horizon.

This thesis is composed of six chapters. The first chapter provides an introduction and insight into the inspiration for this topic. It briefly gives an overview into the history of metamaterials and discusses some popular work done with metamaterial inspired antennas. Additionally, it also gives readers a synopsis of electrically small antennas and their fundamental limitations. This chapter also draws an outline of the structure of this document, explaining its organization and structure.

The second chapter dwells extensively on the concept of metamaterials, discussing some of the pioneer work done by some notable researchers. First, an in depth discussion is done on theoretical analysis done by Victor Veselago on double negative materials. This is then followed by a discussion of work done by John Pendry and his colleagues and by Smith on a practical medium exhibiting single negative and double negative responses.

In the third chapter, microstrip patch antennas are discussed in great detail, with analysis done on the topology, the cavity model and also the design procedure for a traditional patch antenna. Once the discussion on a single patch antenna is done, the notion of phased array patch antennas are discussed. In this section, some light was shed on concepts such as array factor that helps in determining the sidelobe levels and

phase adjustments required to point the beam in a particular direction. This chapter also discusses some work done by Andrea Al*ù* in terms of loading metamaterials with microstrip antennas to achieve miniaturization goals. Finally, this chapter ends with an example of a traditional patch antenna at 200MHz, designed and simulated in HFSS, that will be used for comparison with metamaterial loaded patch antennas.

Several metamaterial unit cells have been discussed and designed in the fourth chapter. This chapter presents two major geometries that are tuned to demonstrate SNG or DNG properties. The first geometry is the double split ring resonator designed and simulated to exhibit mu-negative properties. The next structure is a 10 turn thin wire spiral designed to exhibit double negative and/or single negative properties. The spiral resonators have been tuned to obtain these properties in specific frequency ranges.

The fifth chapter is the main chapter that focuses on microstrip patch antennas integrated with metamaterials as substrates beneath the patch. Metamaterials designed in the fourth chapter were placed beneath the patch and the patch dimensions were optimized to achieve subwavelength resonance. Spiral resonators were then chosen to integrate with patch elements that contributed towards the development of an electrically small patch antenna array. This chapter is primarily comprised of simulation discussion and results in terms of return loss, input impedance and radiation patterns (2D and 3D diagrams).

The last chapter concludes the thesis and summarizes important points of this thesis.

CHAPTER 2: METAMATERIALS

The response of a material to an incoming electromagnetic wave can be attributed to the relative permeability and permittivity possessed by the material. Electric permittivity (ϵ_r) is associated with how a material responds to an applied electric field and is related to the energy stored in the incident electric field. In the same way, relative magnetic permeability (μ_r) describes the ability of a medium to support the formation of magnetic fields. Hence, permeability is related to the energy stored in a magnetic field. This chapter discusses the effect, these electromagnetic properties have on a plane monochromatic wave propagating through a medium. It also describes new emerging materials possessing negative ϵ_r and/or μ_r followed by intriguing qualities like negative refraction and back propagation exhibited by them.

2.1 Classification of Media

The response of a medium to an incident electromagnetic wave is largely described by its relative permeability and permittivity. The combination of ϵ_r and μ_r and the possibility of $\epsilon_r < 0$ and/or $\mu_r < 0$, has led to a new system to classify materials, as can be seen in Fig.2.1. This new categorization of materials gives four possible quadrants in which materials may be placed.

The first quadrant is an assortment of materials readily available in nature such as regular dielectrics. These materials possess a combination of $\epsilon_r > 0$ and $\mu_r > 0$ and are rightly labeled as double positive materials (DPS). Air is a very common medium of transmission whose relative permittivity and permeability are both approximately equal to 1. Having positive values of permittivity and permeability, DPS materials conventionally obey Snell's law. When a ray of light travels from one DPS media to

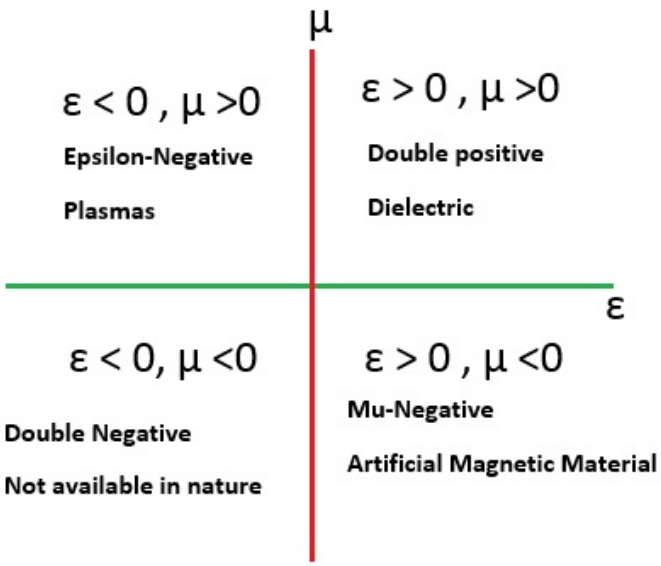

Figure 2.1: ϵ-μ diagram

another, some of the light gets refracted into the second medium and some reflects back into the first medium. The refracted ray will experience a change in direction as it enters the second medium. The new angle of propagation is defined positive from the normal to the boundary of the two media. The refracted ray will lie on the opposite side of the normal with reference to the incident ray.

Media lying in the second and fourth quadrant are broadly described as single negative materials (SNG). As such, materials whose permittivity is negative and permeability is positive lie in the second quadrant, and are commonly called epsilon-negative materials (ENG). Certain noble metals such as gold exhibit negative ϵ in optical and infrared frequency regions. On the other hand, materials lying in the fourth quadrant possess values of positive relative permittivity and exhibit negative permeability and are popularly called Mu-negative materials (MNG). In certain frequency domains, some gyrotropic materials exhibit these properties. It is interesting to note that the refractive index of materials displaying negative values of either permittivity or permeability is imaginary and hence do not have propagating capabilities.

The last combination of materials exhibiting simultaneous negative values of rela-

tive permittivity and permeability gives us an intriguing material not readily available in nature. These materials lying in the fourth quadrant can be referred to as double negative materials (DNG) and can be tuned for specific applications. The theoretical existence of such a material was first discussed in 1964 by V.G. Veselago which will be discussed in great detail in the latter part of this chapter. Surprisingly, these materials were found to be of propagating nature and supported a so called "backward propagation" owing to the negative refractive index possessed by such a material. These materials, with all these astonishing properties, were named "Meta-materials"

Meta in Greek is synonymous with 'beyond' or 'altered'. Metamaterials derive their properties from their structure rather than composition. Hence, metamaterials can be loosely defined as artificially engineered materials that can be designed to possess properties that have not been found in nature. Interestingly, the size of a metamaterial unit cell is much smaller than its operating wavelength, typically less than $\lambda/10$ or smaller.

The history of metamaterials shows plenty of invaluable research done by scientists beginning from the 19th century. The notion of the existence of metamaterials began with discussion of chiral media, metal lenses and so on. However, the notion of meta-particles gained popularity following research conducted by Victor Veselago, when he began to theoretically consider the existence of such a double negative material as a propagating medium for a plane monochromatic light. The next section discusses in particular, the findings of this theory that has attracted many other scientists towards these double negative substances.

2.2 Theoretical Discussion on Double Negative Material

In 1964, V.G. Veselago theoretically described the behavior of a double negative material, where he assumed a medium having simultaneous negative values of ϵ and μ [29]. In his paper, he considered relations in which ϵ and μ appear separately.

According to Maxwell's equations in a source-free region,

$$\begin{aligned} \nabla \times \vec{E} &= -\frac{\partial \vec{B}}{\partial t} \\ \nabla \times \vec{H} &= \frac{\partial \vec{D}}{\partial t} \end{aligned} \tag{2.1}$$

The electric flux density D and magnetic flux density B shown in Maxwell's equations above are related to the permittivity ϵ ($\epsilon = \epsilon_0 \epsilon_r$) and permeability μ ($\mu = \mu_0 \mu_r$) as given below.

$$\begin{aligned} \vec{B} &= \mu \vec{H} \\ \vec{D} &= \varepsilon \vec{E} \end{aligned} \tag{2.2}$$

When a plane monochromatic wave is incident on a double negative material (ϵ and μ both < 0), the relationship between wave vector $\vec{k}$, electric field $\vec{E}$ and magnetic field $\vec{H}$ can be represented in the context of equations 2.1 and 2.2 as follows:

$$\begin{aligned} \vec{k} \times \vec{E} &= \omega \mu_0 \mu_r \vec{H} \\ \vec{k} \times \vec{H} &= -\omega \varepsilon_0 \varepsilon_r \vec{E} \end{aligned} \tag{2.3}$$

Since $\epsilon < 0$ and $\mu < 0$, $\vec{k}$, $\vec{E}$ and $\vec{H}$ behave opposite to the right hand rule, forming a left handed triplet. The Poynting vector $\vec{S}$, determines the directional power flow of the wave. The relationship between $\vec{S}$, $\vec{E}$ and $\vec{H}$ is given as usual by equation 2.4

$$\vec{S} = \vec{E} \times \vec{H} \tag{2.4}$$

Due to negative values of ϵ and μ, $\vec{S}$ forms a right handed set with $\vec{E}$ and $\vec{H}$. From the relation between $\vec{k}$, $\vec{E}$, $\vec{H}$ and $\vec{S}$ shown in Fig.2.2 we can observe that the Poynting vector $\vec{S}$ travels in a direction opposite to the wave vector $\vec{k}$.

Thus, in a metamaterial having simultaneous negative values of ϵ and μ, the Poynting vector $\vec{S}$ travels in a direction opposite to the wave vector $\vec{k}$. Due to which a double negative medium exhibits "backward propagation". Hence, double negative metama-

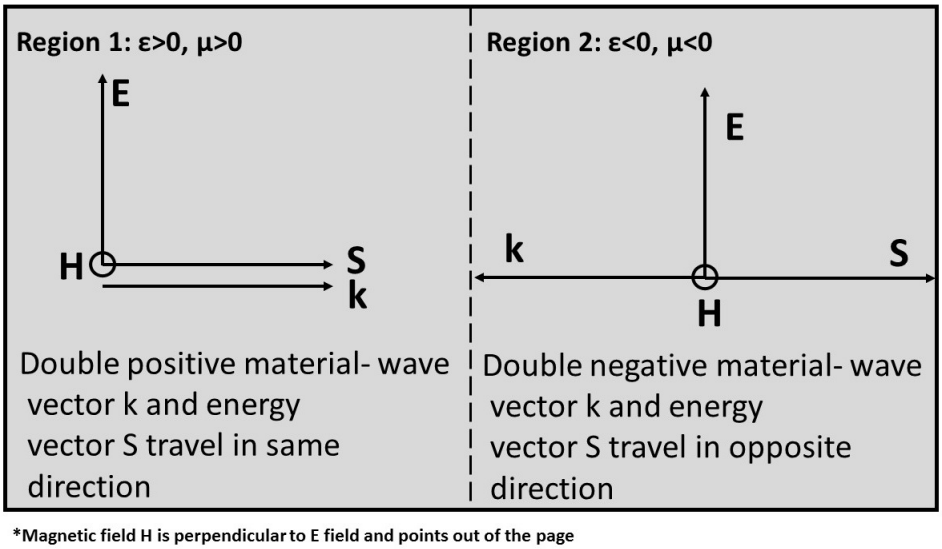

Figure 2.2: Left-handedness of material

terials can also be referred to as left-handed materials.

Another interesting property discussed by Veselago in his paper is that of refraction of a ray between two media, one of which has double positive property (DPS) and the second medium which possesses double negative property (DNG). The refractive index 'n' of a material describes how light propagates through the medium. As we know, n=$\sqrt{\epsilon_r \mu_r}$. In a double negative medium, $\epsilon \leq 0$ and $\mu \leq 0$. Hence, n=$\sqrt{-\epsilon_r} \times \sqrt{-\mu_r} = j\sqrt{\epsilon_r} \times j\sqrt{\mu_r}$ = -$\sqrt{\epsilon_r \mu_r}$.

Snell's law states that the ratio of refractive index n_1 and n_2 of the two media is equivalent to the reciprocal of the ratios of the sines of the angles of incidence θ_1 and refraction θ_2. Equation 2.5 describes Snell's law mathematically where θ_1 is the incident angle and θ_2 is the refracted angle.

$$\frac{n_1}{n_2} = \frac{\sin\theta_2}{\sin\theta_1} \tag{2.5}$$

Reordering this equation, Snell's law can be represented by $n_1 \sin\theta_1 = n_2 \sin\theta_2$. When a ray of light travels from a double positive medium ($n_1 > 0$) into a second medium,

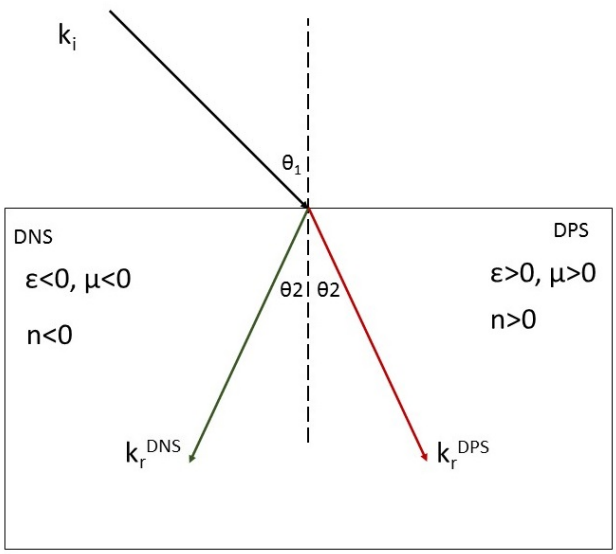

Figure 2.3: Negative refractive index of DNG material

some of the light will propagate through the second medium and some will reflect back into the first medium. If the second medium is a double positive material whose refractive index is positive ($n_2 > 0$), the refracted ray will travel at an angle θ_2 measured from the normal ray. This refracted ray will lie on the opposite side of the normal with respect to the incident ray. However, if the second propagating medium is DNG, the refractive index n_2 will be negative. The refracted ray will travel through the material making the same angle θ_2, but will lie on the same side of the normal as the incident ray. If the second propagating medium is single negative i.e either ϵ or μ is less then zero, the refractive index will be an imaginary number. A ray of light incident on such an object would not propagate through such a material as the waves are evanescent. All of the incident ray will reflect back unless the width of such a medium is very small, in which case a small fraction of incident ray would pass through the material in a process known as resonant tunneling.

Artificial materials can be physically engineered to consist of these negative values ϵ_r and μ_r. This was made possible by J.B Pendry et al in 1998, when they suggested a photonic structure consisting of a 3D array of thin wires arranged periodically,

that exhibit negative permittivity below the plasma frequency [21]. The authors of this publication analyzed the electromagnetic response of an array of thin wires. Pendry also showed that materials exhibiting negative permeability can be made using split ring resonators [22]. The next section analyzes how negative permeability and permittivity can be obtained using wires and split rings.

2.3 Artificial Materials Designed to Have Negative ϵ_r and μ_r

Consider an array of metallic cylinders arranged along the X-Y axis and aligned along the Z-axis as shown in Fig.2.4. An electric field is applied parallel to these wires.

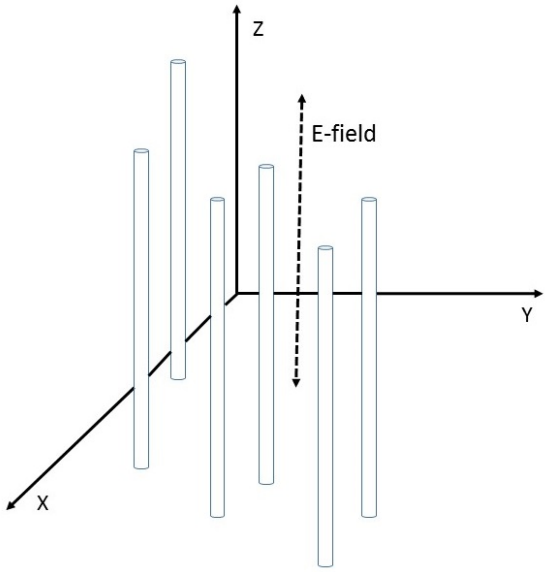

Figure 2.4: Array of wires aligned along Z-axis

Metals show response to electromagnetic radiation due to the plasma resonance of electrons. The dielectric constant of the metal is related to the plasma frequency ω_p by the following relation:

$$\varepsilon = 1 - \frac{\omega_p^2}{\omega^2} \tag{2.6}$$

Here, the plasma frequency ω_p is related to the electron density n, charge e and electron mass m_e according to,

$$\omega_p = \frac{ne^2}{\varepsilon_0 m_e} \tag{2.7}$$

Since the electric field is applied parallel to the structure, electrons are forced to move within wire structures. Since only a part of the space which is filled by metal is affected by the applied electric field, the average electron density is reduced. The effective electron density is given by the following equation,

$$n_{eff} = n\frac{\pi r^2}{a^2} \tag{2.8}$$

where, n is the electron density in the wires, r is the radius of the wires and a is the distance between wires. When current flows throughout the metallic wires, a strong magnetic field is established around the wires given by,

$$\vec{H} = \frac{\pi r^2 nve}{2\pi R} \tag{2.9}$$

The numerator in this equation determines the current flowing in the wire given by I=$\pi r^2 nve$. The H field can also be expressed as,

$$\vec{H} = \frac{1}{\mu_0}\nabla \times A \tag{2.10}$$

where A, is given by the following equation,

$$A = \frac{\mu_0 \pi r^2 nve}{2\pi} \ln\left(\frac{a}{R}\right) \tag{2.11}$$

The electrons in a magnetic field contribute to the momentum by eA and momentum per unit length of the wire can be given by,

$$\pi r^2 neA = \frac{\mu_0 e^2 (\pi r^2 n)^2 v}{2\pi} \ln\left(\frac{a}{r}\right) = m_{eff}\pi r^2 nv \tag{2.12}$$

where m_{eff} in Equation 2.12 is the effective mass of electrons. m_{eff} is given by,

$$m_{eff} = \frac{\mu_0 e^2 \pi r^2 n}{2\pi} \ln\left(\frac{a}{r}\right) \tag{2.13}$$

The new plasma frequency is given by,

$$\omega_p^2 = \frac{n_{eff} e^2}{\varepsilon_0 m_{eff}} = \frac{2\pi c^2}{a^2 \ln\left(\frac{a}{r}\right)} \tag{2.14}$$

By decreasing the electron density, we can obtain negative permittivity below the resulting plasma frequency.

Another publication by Pendry et al. discusses the possibility of artificial structures exhibiting negative permeability ($\mu < 0$) [22]. The authors assume a square array of metallic cylinders with external magnetic field applied parallel to the structure. Considering a single cylinder, a capacitive element was added to the structure by providing spacing in the circumference of the cylinder. The cylinder now exhibits a split ring configuration as shown in Fig.2.5. It is interesting to note that the gap in the ring breaks the flow of current through the ring. This gap between the metal

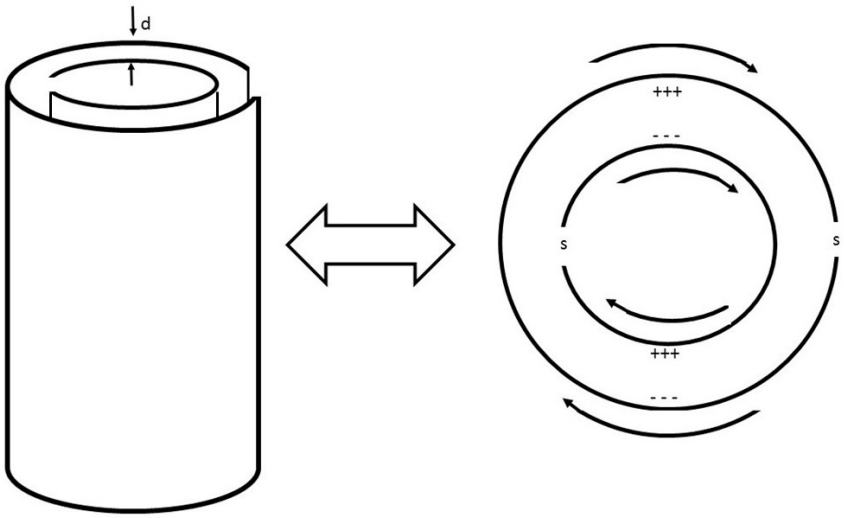

Figure 2.5: Split ring cylinder and equivalent ring model

rings give rise to capacitance in the gap which allows a displacement current to flow through the gap. Additionally, the gap between two adjacent cylinders also gives rise to capacitance between them. Capacitance per unit area between the two rings is given by,

$$C = \frac{\varepsilon_0}{d} = \frac{1}{dc^2\mu_0} \tag{2.15}$$

where d is the distance between two rings. Since the individual cylinder is part of an array of cylinders, the fractional volume of the cell occupied by the interior of the cylinder is given by,

$$F = \frac{\pi r^2}{a^2} \tag{2.16}$$

Effective permeability can expressed in terms of F and C according to,

$$\mu_{eff} = 1 - \frac{F}{1 + \frac{2\sigma i}{\omega r\mu_0} - \frac{3}{\pi^2\mu_0\omega^2 Cr^3}} \tag{2.17}$$

Here, σ in Equation 2.17 is the conductivity of the cylinder surface per unit area. With added capacitance in the structure, the inductance is balanced and hence we obtain a resonant effective permeability. Equation 2.17 can be rearranged as follows,

$$\mu_{eff} = 1 - \frac{F\omega}{\omega^2 + \frac{2\omega\sigma i}{r\mu_0} - \frac{3}{\pi^2\mu_0 Cr^3}} \tag{2.18}$$

The resonant frequency becomes,

$$\omega_0 = \sqrt{\frac{3}{\pi^2\mu_0 Cr^3}} = \sqrt{\frac{3dc^2}{\pi^2 r^3}} \tag{2.19}$$

The magnetic plasma frequency ω_{mp} is then

$$\omega_{mp=}\sqrt{\frac{3dc^2}{\pi^2 r^3\left(1 - \frac{\pi r^2}{a^2}\right)}} \tag{2.20}$$

A typical response of permeability exhibited by split ring resonating structures is shown in Fig.2.6. The figure shows negative μ_{eff} occurs when $\omega_0 \leq \omega \leq \omega_{mp}$. The bandwidth between ω_0 and ω_{mp} is usually very narrow. The magnitude of negative μ obtained in this frequency range depends on the capacitance and inductance exhibited by the structure. In order to simplify the structure, we can neglect the length of the cylinder and just consider concentric split rings which will show similar behavior.

Observing the split ring structure closely displayed in Fig.2.7, where the thickness of each ring is 't' and the inner and outer rings have gap of 'w' between them, then μ_{eff} can be expressed in terms of the physical parameters of the rings. The resonant frequency of the structure can be altered by changing the radius of the inner ring 'r', thickness of the metal rings and gap between the rings. These parameters also affect the negative permeability exhibited by the structure.

Split ring structures can be thought of as LC resonators, where the metal rings provide inductance to the structure. The capacitance mostly is due to the gap between the two concentric rings and the split in each individual ring. Hence, the resonant frequency of the structure can also be related by $\omega_0 = \frac{1}{\sqrt{LC}}$. For ease of fabrica-

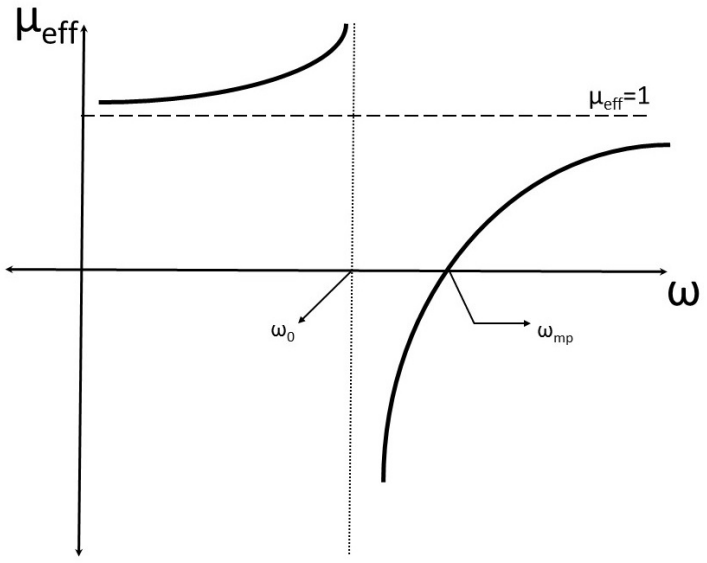

Figure 2.6: Effective permeability shown by split rings

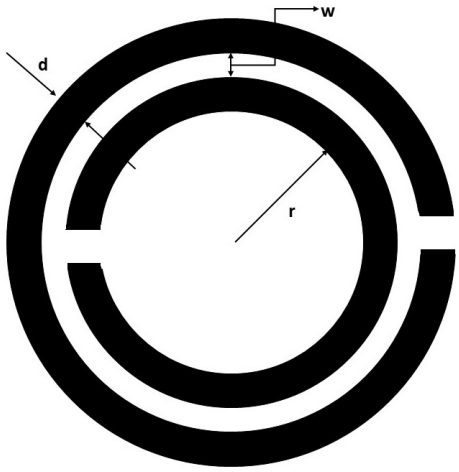

Figure 2.7: Individual split ring resonator structure

tion, split ring structures can be printed on copper clad dielectric slabs such as FR-4 epoxy. Printing split rings on dielectric slabs makes the structure robust, when the metamaterial cell needs to be incorporated into other electromagnetic structures like waveguides and antennas. Also, the rings can have different shapes e.g square, rectangular, circular, hexagonal and so on.

Another popular structure that exhibits negative permeability is a spiral resonating structure. One publication [7] focused its discussion on spiral metamaterial structures, wherein a traditional split ring geometry was modified into spiral form by interconnecting two concentric rings with a metal trace. This geometry is displayed in Fig.2.8.

Studying the spiral structures in detail, it is observed that they form an equivalent LC resonator similar to a split ring resonator. The net capacitance and inductance in a spiral structure are greater than in a split ring resonator network and hence it can exhibit a lower resonant frequency in comparison to a split ring resonator. Hence, adding more turns in a spiral resonator can decrease the resonance shown by the structure without further increasing the dimensions of the outer ring.

Fig.2.9 (a) shows an equivalent circuit of a split ring resonator model. The inductance of the rings can be averaged to L. The total capacitance between the rings is C_0 where, the upper half of the ring exhibits a capacitance of $C_0/2$ and lower half

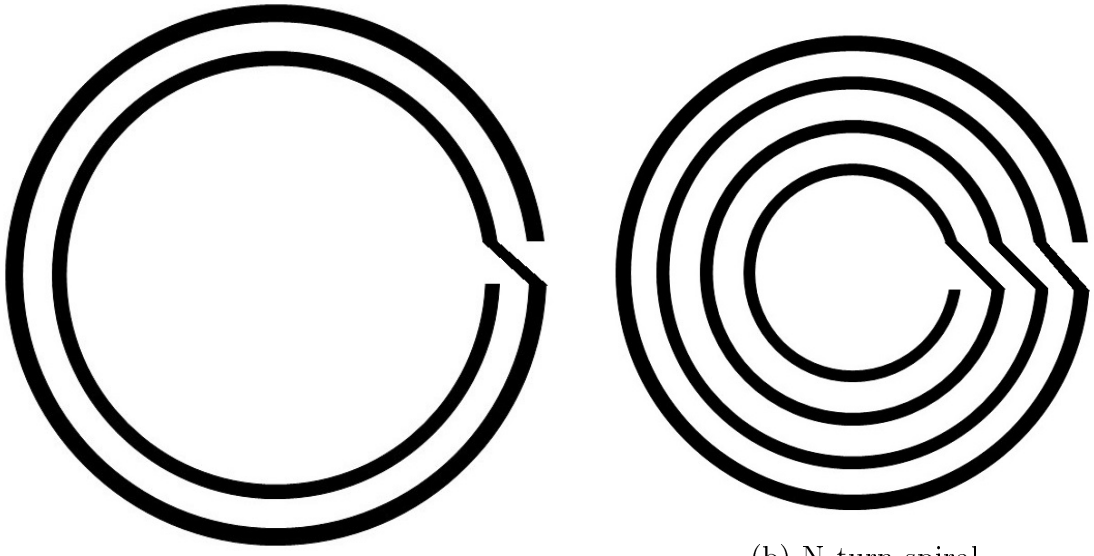

(a) SRR modified spiral

(b) N turn spiral

Figure 2.8: Spiral resonator metamaterials

exhibits a capacitance of $C_0/2$ as well. The two capacitances are in series and hence the total capacitance in the circuit will be $C_0/4$.

Considering an SRR modified to be a spiral geometry, the total capacitance in the circuit is C_0 due to the gap between the two turns (Fig.2.9 (b)). Hence, the net capacitance present in a spiral structure is larger than in a split ring geometry and hence it is safe to conclude that a spiral structure will have lower resonance than a split ring resonator of the same overall size. It is interesting to note that as the number of turns increase, the capacitance and inductance keep getting added in parallel with each turn, resulting in a subsequent increase in the total capacitance and inductance. Hence, by increasing the number of turns or by adding more rings to the spiral, we can obtain a lower resonant frequency. The equivalent lumped circuit models of split rings and spirals have been discussed in great detail in [8].

Split rings and electrically polarized metal rods can be simultaneously simulated to obtain double negative properties in the structure. The resulting composite structure will possess a combination of a negative μ value contributed by the split ring structure and a wide negative ϵ below the plasma frequency of the rod. A simple method to

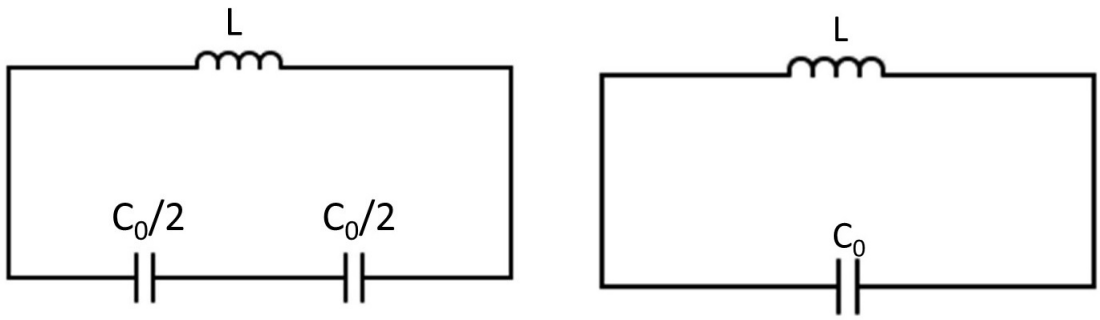

(a) Split ring resonator (b) Spiral resonator-single turn

Figure 2.9: Equivalent electrical circuit model

build such a structure is to print a split ring structure on one side of a copper clad dielectric material and metallic trace stretching along the length of the structure on the other side of the dielectric. such that it is exposed to E-field applied parallel to the trace. This combination of SRR and wire structure proposed in [26] constitutes of an array of split ring resonators printed on a dielectric substrate, which provides negative μ to the medium. The negative ϵ is contributed by a metal post medium that is made by drilling holes in an aluminum plated dielectric slab and inserting metal rods into these holes. In order to make this bulky structure more feasible, the rings and wires were fabricated on a double sided copper clad dielectric substrate. One side of the substrate consisted of printed split rings and the second side consisted of strips of metal printed along the entire length of the substrate, a prototype of which is shown in Fig.2.10.

The bulk of the discussion on metamaterials in this chapter assumes arrays of multiple structures that together exhibit negative values of relative permittivity and permeability. In contrast, this research focuses on development of individual meta-structures that maintain a size limit imposed upon them, while still exhibiting sufficient negative permittivity and permeability. Various geometries of metamaterial units cells have been proposed that can lead to a possibility of replacing them with regular dielectrics. In spite of single negative materials being non-propagating in na-

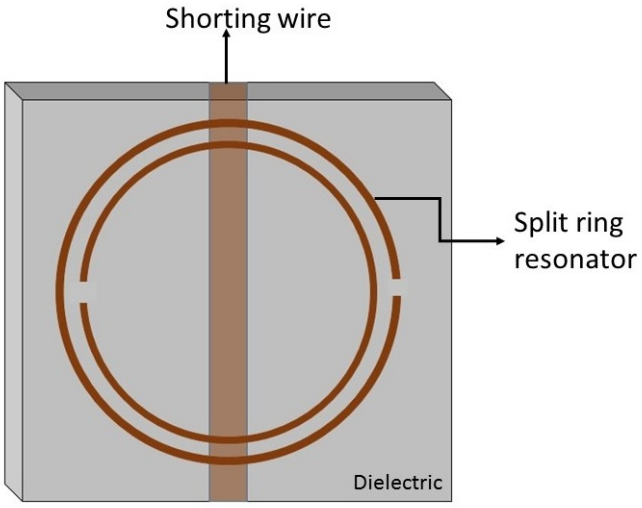

Figure 2.10: SRR and wire combination exhibiting double negative properties

ture, an attempt has been made to observe the effects of a dielectric having negative permittivity and/or permeability on the fields in the underlying cavity of a patch antenna. Consequently, the unit cells designed for this purpose will have resonant frequencies lying between 100 MHz and 1 GHz.

CHAPTER 3: MICROSTRIP PATCH ANTENNA

IEEE describes an antenna as that part of a transmiter and receiver system which is designed to radiate and/or receive electromagnetic waves. An antenna is a device that is capable of radiating electromagnetic energy in a desired direction and are comprised of metallic conductors that are often fed with an electric signal with the help of transmission lines.

Heinrich Hertz, a German physicist built one of the first antennas in 1888-an electric dipole [6]. Hertz proved the existence of electromagnetic waves by proposing a metal wire pair as a radiator with a coil driven spark gap. He also added capacitive spheres at the ends of the metal wire pair to adjust the circuit resonance. This simple setup was modified later by replacing the spark gap with a generator and is now called a simple half wave dipole. This paved way to develop the first family of antennas universally called wire antennas. Inspired from the simple wire antenna, many topologies of antennas were then developed during the later years, some of which are mentioned below.

1. Wire Antennas- A wire of a particular length when fed in the center can be made to radiate. A well known example of this type of antenna is the half wavelength dipole. The dipole radiates in an omnidirectional pattern. The two arms of the dipole can be folded and connected at its end to increase gain and decrease the space that the dipole occupies. This modified dipole is called a folded dipole. Applying image theory, the length of a dipole can be reduced by half. Monopole antennas are made up of one arm of the dipole and the other arm is replaced by a conducting ground plane. Loop antennas are another type of wire antenna.

The radius of the loop is much smaller than the operating wavelength. Being small in size and having gain and an omnidirectional pattern just like a dipole, loop antennas have found extensive use in communication devices like the cell phone and pager.

2. Microstrip Antennas- Antennas can be printed on a dielectric substrate with a ground plane forming a microstrip structure and are called microstrip antennas. These antennas are highly directional and have higher gain than an equivalent dipole antenna. The most common microstrip antenna is a patch antenna that is very widely used in telecommunication. Another type of microstrip antenna is the inverted F antenna whose length is half of a patch antenna. Inverted F antennas are formed by simply shorting one of the ends of the patch to the ground plane.

3. Frequency Independent Antennas- When the two arms of a dipole antenna are increased in size and rotated around the feed center in opposite directions, it forms a spiral structure called a spiral antenna. These antennas are extremely broadband and directional. Other examples of broadband antennas are log periodic antennas, the Yagi-Uda antenna and helical antennas to name a few. These antenna structures produce a circularly and/or linearly polarized electromagnetic wave and are known to radiate with a very high gain.

4. Aperture Antennas- Antennas that are excited with a propagating wave are referred to as aperture antennas. Open-ended waveguides, horn antennas and slotted waveguides are some examples of aperture antennas. The fields within the aperture are used to determine the radiation pattern of such antennas. Optimizing the aperture size of such antennas can provide high gain radiation.

5. Reflector Antennas- In order to increase the directivity of an antenna, we place a conductive reflective structure behind a feed antenna to make it radiate with

more directivity and improve the antenna gain. Some common structures used for reflection are paraboloids. These antenna structures consist of a feed antenna like a waveguide horn and they reflect the signals radiated by the feed antenna to increase directivity. Reflector antennas can be analyzed using a geometrical optics approximations at high frequency.

In summary, different topologies of antennas are available that are designed to accomplish desired radiation characteristics specific to the application. However, the focus of discussion in this chapter will be on a rectangular antenna topology that belongs to the family of microstrip antennas- a traditional patch. The structure, cavity model, design procedure and radiation characteristics of a patch antenna element is discussed in great detail. This is followed by a simple demonstration of a patch antenna modeled using HFSS.

3.1 Patch Antennas

Patch antennas are comprised of a flat sheet of metal typically rectangular, square or circular placed at a uniform distance above a flat ground plane. The ground plane and metal patch are separated by a dielectric substrate having a finite permittivity. Patch antennas are planar, low profile, lightweight and can be easily fabricated using printed circuit technology; patch antennas can be easily designed for dual polarization and multi-frequency applications. These numerous technologies have made patch antennas very suitable for use in aerial vehicles. Because of its flat topology and various other qualities, microstrip patch antennas have gained popularity in commercial mobile and wireless communication systems.

Let us begin by considering a typical rectangular metal patch of length 'L' and width 'W' sitting on a dielectric material of thickness 'h' having a dielectric constant ϵ_r. This whole structure sits on a metal ground plane which typically extends $\lambda/4$ from the radiating metal patch, as described in Fig.3.1.

A patch is typically half wavelength long within the dielectric substrate. When

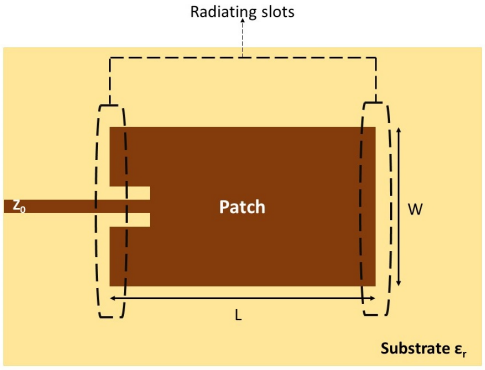

(a) Top View

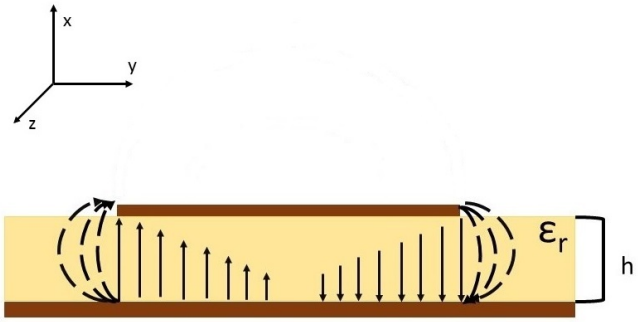

(b) Side View

Figure 3.1: Structure and dimensions of a microstrip patch antenna

a microstrip patch is fed with an energy source, a charge distribution is established on the bottom and top surface of the metal patch and the ground plane. Since the patch is electrically $\lambda/2$ long, positive charges arise at the beginning of the patch and negative charges occur at the end of the patch. Exact opposite charges are seen on the surface of the ground plane. These repulsive charges from the ground plane push some charge from the bottom surface of the patch, around its edges to the top of the patch. This movement of charges gives rise to current densities on the top and bottom of the patch. This flow of current to the top of the patch gives rise to a very weak magnetic field tangential to the edges of the patch. Thus the patch can be treated as a cavity with its four side walls having magnetic conductivity and the top and bottom walls being electrically conducting. It should be noted that only TM configuration is

considered as a propagating mode in the patch cavity, with TM_{010} being the dominant mode with the lowest frequency of operation. The resonant frequency exhibited by the patch is given by Equation 3.1

$$f_{r_{mnp}} = \frac{1}{2\pi\sqrt{\mu\varepsilon}}\sqrt{\left(\frac{m\pi}{h}\right)^2 + \left(\frac{n\pi}{L}\right)^2 + \left(\frac{p\pi}{W}\right)^2} \tag{3.1}$$

For a patch antenna, L > W > h, so the dominant resonant mode is the TM^x_{010} (assuming that the antenna structure lies in the Y-Z plane), and thus the lowest resonant frequency that the patch is capable to operate at is given in Equation 3.2

$$f_{r_{010}} = \frac{1}{2\sqrt{\mu\varepsilon}L} = \frac{1}{2\sqrt{\mu_0\varepsilon_0\varepsilon_r}L} = \frac{c}{2L\sqrt{\varepsilon_r}} \tag{3.2}$$

The fields on the PMC boundaries are responsible for radiation occurring in a direction perpendicular to the plane of the antenna. These edges of the patch along its length are called radiating slots of the antenna.

In the far-field zone, the electric fields radiated by each radiating slot are given by [3]

$$E_\phi = j\frac{k_0 hW E_0 e^{-jk_0 r}}{2\pi r}\left\{\sin\theta\frac{\sin X}{X}\frac{\sin Z}{Z}\right\} \tag{3.3}$$

where,

$$X = \frac{k_0 h}{2}\sin\theta\cos\phi \tag{3.4}$$

$$Z = \frac{k_0 W}{2}\cos\theta \tag{3.5}$$

The height of the substrate of a patch antenna typically lies between $0.003\lambda_0 \leq h \leq 0.05\lambda_0$. Since the height h is small, the electric field equation is well approximated with,

$$E_\phi \simeq j\frac{hE_0 e^{-jk_0 r}}{\pi r}\left\{\sin\theta\frac{\sin\left(\frac{k_0 W}{2}\cos\theta\right)}{\cos\theta}\right\} \tag{3.6}$$

Equation 3.6 gives the E-field due to one radiating slot. Rectangular patch antennas

have two radiating slots separated by an effective length L_e. Thus the total electric field for the two slots combined will be

$$E_\phi^t \simeq j\frac{2hE_0e^{-jk_0r}}{\pi r}\left\{\sin\theta\frac{\sin\left(\frac{k_0W}{2}\cos\theta\right)}{\cos\theta}\right\}\cos\left(\frac{k_0L_e}{2}\sin\theta\sin\phi\right) \tag{3.7}$$

The principle E- plane of the patch antenna radiation pattern lies in the x-y plane, where, $\theta = 90°$, $0° \leq \phi \leq 90°$ and $270° \leq \phi \leq 360°$. The radiated E fields in the E plane can be obtained using the following equation:

$$E_\phi^t \simeq j\frac{k_0WhE_0e^{-jk_0r}}{\pi r}\left\{\frac{\sin\left(\frac{k_0h}{2}\cos\phi\right)}{\frac{k_0h}{2}\cos\phi}\right\}\cos\left(\frac{k_0L_e}{2}\sin\phi\right) \tag{3.8}$$

The principle H plane lies in the X-Z plane, where, $\phi = 0°$, $0° \leq \theta \leq 180°$. The electric fields in the H plane can be written as,

$$E_\phi^t \simeq j\frac{k_0WhE_0e^{-jk_0r}}{\pi r}\left\{\sin\theta\frac{\sin\left(\frac{k_0h}{2}\sin\theta\right)}{\frac{k_0h}{2}\sin\theta}\frac{\sin\left(\frac{k_0W}{2}\cos\theta\right)}{\frac{k_0W}{2}\cos\theta}\right\} \tag{3.9}$$

From the equations describing electric fields radiated by a patch antenna, it is evident that the width of the patch, W, strongly affects the radiation pattern exhibited by the antenna. The length of the patch contributes to the resonating mode of the antenna which in turn produces a resonant frequency in the patch.

Directivity is a figure of merit which describes the direction of maximum propagation of fields and energy. Typically, the directivity of a patch antenna ranges from 6-9 dB, and can be expressed as

$$D = \begin{cases} 8.2dB & (W \ll \lambda_0) \\ 8(\frac{W}{\lambda_0}) & (W \gg \lambda_0) \end{cases} \tag{3.10}$$

The input impedance of the patch antenna, which is complex, varies as a function of frequency. The resistive and reactive part of the input impedance exhibit symme-

try about the resonant frequency. The width of the patch element strongly affects the antenna's input impedance; increasing the width of the patch can decrease the impedance.

Different methods to feed a traditional patch antenna have been suggested [23] [9]. Typical configurations include microstrip feed, probe feed and aperture coupled feed and each type of feeding method has its own advantages as well as disadvantages. Each of these configurations is shown in Fig.3.2. The position of the feed plays a very crucial role in optimizing the input impedance of the antenna.

A patch antenna fed by microstrip transmission line is the easiest configuration to fabricate and match with the antenna impedance. The microstrip transmission line is a metal strip of width w_1 having a characteristic impedance Z_0. The characteristic impedance is easy to control by changing the width of the microstrip line. Impedance matching can be easily done by controlling the inset position of the feed. Since current at the edge of the patch is minimum, the input impedance of a patch fed at the edge as shown in Fig.3.1a is high. Hence, it is desirable that the microstrip transmission feed line position be inset in order to control the input impedance of the patch as shown in Fig.3.2a. A patch antenna can also be matched with the feed transmission line using a quarter wave transformer.

A coaxial probe fed patch antenna is shown in Fig.3.2b. A coaxial cable is a type of transmission line consisting of an inner conductor and an outer conductor separated by a dielectric such as polyethylene. The characteristic impedance of the coaxial cable can be controlled by controlling the radii of the inner and outer conductors. In order to feed the patch, the inner conductor is connected to the metal patch sitting on top of the substrate. The outer conductor is connected to the metal ground plane on which the entire antenna structure sits. The position of the feed can be altered to improve the input impedance of the antenna in order to assure that maximum power is delivered to the antenna. The coaxial feed adds inductance to the patch which

can be neglected if the height of the substrate is small. However, if the height of the patch is large, the inductance impacts the impedance of the patch and hence its performance. Since the inner and outer conductors of the probe are made of a PEC material, the probe radiates as well, which may be undesirable.

Fig.3.2c shows a microstrip patch antenna with aperture coupling to a microstrip line. The structure is comprised of a ground plane with a small aperture separated by two dielectric substrates. On the lower side of the bottom substrate, a microstrip feed line is located. Energy in the transmission feed line is coupled to the patch through a hole in the ground plane separating the two substrates. The bottom substrate is usually made up of a high dielectric material to produce tightly coupled fields to avoid unwanted radiation. A lower permittivity dielectric material is used as a top substrate to produce loosely coupled electric fields. The ground plane isolates the feed line from the radiating patch in order to avoid spurious radiation. The feed line width, slot dimensions and position of the slot can be modified to optimize the antenna design.

Substrates typically used in patch antennas have dielectric constants ranging from 2.2 to 12. Smaller permittivity dielectrics produce loose fringing fields, extending away from the patch, producing better radiation. In contrast, a higher permittivity dielectric results in tighter coupling, producing less radiation. The bandwidth of a rectangular patch antenna is inversely proportional to $\sqrt{\epsilon_r}$ [3]. It is normally observed that patch antennas are extremely narrow band antennas with a bandwidth of approximately 3-5%.

3.1.1 Design Procedure

Consider a patch antenna to be designed on a dielectric substrate of height h having a dielectric constant of ϵ_r. The patch antenna is to be designed for frequency f_r. The following steps are used to obtain the dimensions of a patch antenna operating at resonating frequency f_r [4]:

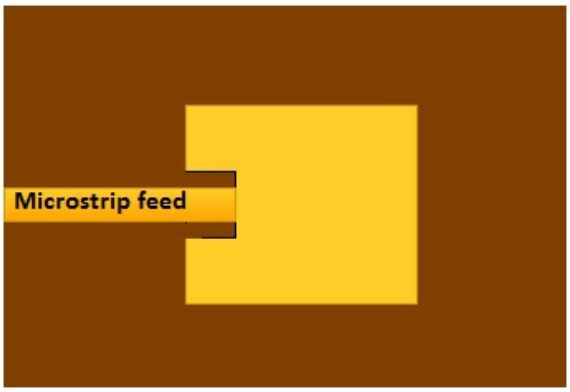

(a) Microstrip line feed

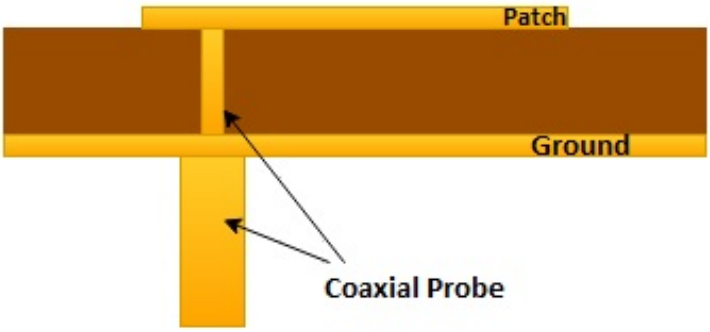

(b) Probe feed

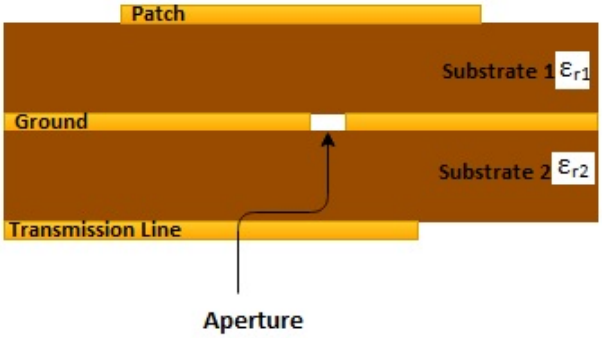

(c) Aperture-coupled feed

Figure 3.2: Typical feeding techniques for patch antenna

1. Find Width W according to the desired feed.

   If the patch antenna is designed to have a microstrip feed, we use the following

formula for calculating the width of the patch.

$$W = \frac{c}{2f_r}\sqrt{\frac{2}{\varepsilon_r + 1}} \tag{3.11}$$

For a probe fed microstrip patch antenna, the width can be calculated using the following formulas,

$$W = \sqrt{h\lambda_d}\left[\ln\left(\frac{\lambda_d}{h}\right) - 1\right] \tag{3.12}$$

here $\lambda_d = \frac{\lambda_0}{\sqrt{\varepsilon_r}}$ and λ_0 is wavelength in free space.

2. Next we find the effective permittivity ϵ_e. Since some of the fields of the microstrip patch exist in air and some lie in the cavity under the patch, the effective permittivity is less that the dielectric constant of the substrate. ϵ_e is a function of $\frac{W}{h}$. For microstrip patch antennas, $\frac{W}{h} > 1$, hence ϵ_e is given by the equation,

$$\varepsilon_e = \frac{\varepsilon_r + 1}{2} + \frac{\varepsilon_r - 1}{2} \times \frac{1}{\sqrt{1 + 12\left(\frac{h}{W}\right)}} \tag{3.13}$$

3. Because of fringing effects, the length of the patch appears greater than its physical dimensions. The dimension of the patch have been extended by a distance of ΔL.

$$\Delta L = 0.412 \times h \times \left(\frac{\varepsilon_e + 0.3}{\varepsilon_e - 0.258}\right) \times \left(\frac{\frac{W}{h} + 0.264}{\frac{W}{h} + 0.8}\right) \tag{3.14}$$

ΔL is a function of ϵ_e and W/h ratio.

4. Since the dimension of the patch is extended by ΔL, the effective length is L_{eff} = L+2ΔL.

$$L = \frac{1}{2f_r\sqrt{\mu_0\varepsilon_0}\sqrt{\varepsilon_e}} - 2\Delta L \tag{3.15}$$

Following these design steps, we sometimes obtain W greater than L. Hence, we choose W_{new}= 0.75W_{old} and repeat the procedure.

In case of a microstrip patch antenna fed by a probe, the location of the probe is given by, $a = \frac{L}{2\sqrt{\varepsilon_{e_L}}}$. ε_{e_L} here is represented by the following equation,

$$\varepsilon_{e_L} = \frac{\varepsilon_r + 1}{\varepsilon_r - 1} + \frac{\varepsilon_r - 1}{2} \frac{1}{\sqrt{1 + 12\left(\frac{h}{L}\right)}} \tag{3.16}$$

While designing a microstrip patch antenna, it is preferable to design the antennas on an infinite ground plane as it prevents back radiations and provides better radiation patterns. However, using electrically large ground planes increases the overall size of the antenna. Due to this, the ground plane is often truncated at a distance of $\lambda/4$ from the edges of the patch.

The radiated E field of a patch antenna varies in a single direction due to which patch antennas generally support linear polarization, either vertically or horizontal depending on the orientation. However, the antenna topology can be modified to support circular polarization by exciting orthogonal TM_{01} and TM_{10} modes simultaneously with a 90 degree phase difference between them. Additionally, the microstrip antenna model can be easily modified to operate at multiple frequencies.

Despite being robust, patch antennas have a few limitations. Patch antennas produce low gain as compared to many other antenna topologies that are used. Since the thickness of the substrate is small, patch antennas can handle low power. They are not very efficient and are subjected to spurious radiation due to the transmission lines that are used to feed the patch. Patch antennas radiate in broadside and it is very difficult to make them radiate endfire. This can be an issue for applications that require patch antennas to radiate near the horizon.

3.1.2 Phased Array Patch Antenna

Patch antenna elements can be used to form an array of multiple patches. This can be used to overcome the shortcomings of a single patch antenna. Adding multiple patches in an array can increase the overall gain of an antenna with a much narrower and directed beam. Single elements are grouped together in an array and have the capability to cancel out interference from a particular direction. Another interesting function of an antenna array is to steer the beam in a particular direction by applying suitable phases to individual elements of the array. Patches, as shown in Fig.3.3, can be arranged in a single line linearly or in two dimensions to form a planar structure. The antenna elements have to be identical and placed at equal distances from each other. The distance between patches also affects the radiation pattern of the array. As such, the spacing between individual elements has to be at least $\lambda/2$ to avoid mutual coupling.

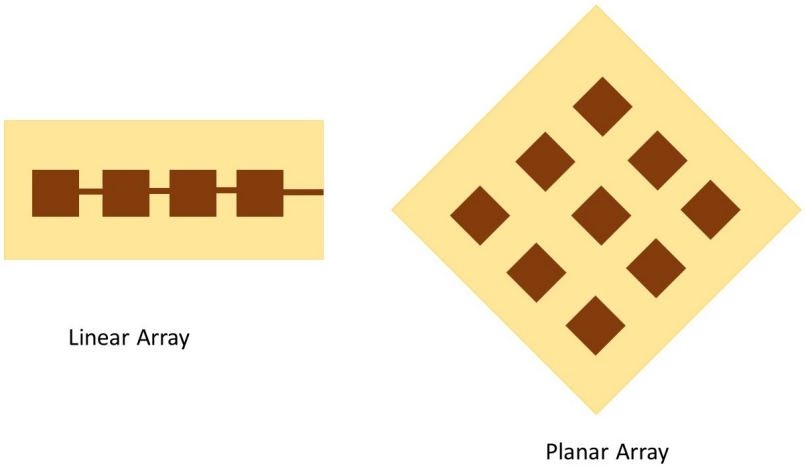

Figure 3.3: Array configurations

A phased array antenna is a type of antenna array that enables the main beam to be steered to point in a desired direction. A phased array antenna structure consists of back-end circuitry that facilitates input signal amplification as well as phase shifting. The input signal that is fed to the antenna is first divided to feed multiple elements

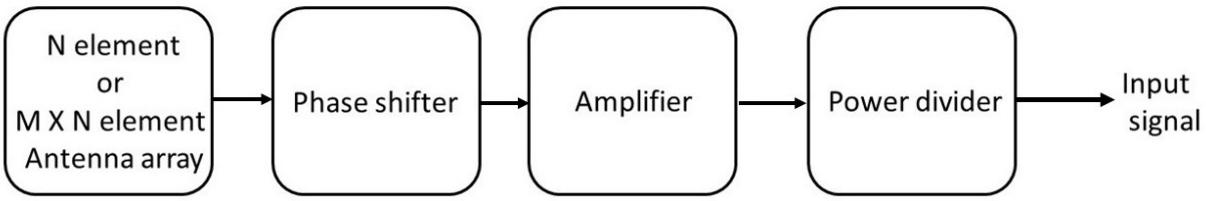

Figure 3.4: Block diagram of phased array system

of the array using power dividers. The divided input signal is then amplified and fed to individual elements of the array. The magnitude of amplitudes fed to each element determines the sidelobe level of the radiation pattern. Before feeding the amplified signals to the individual patch elements, they are phase shifted. The phase given to individual elements determines the angle/direction in which the main beam is intended to point. The block diagram in Fig.3.4 describes a typical phased array system explained above. Patch antennas radiate with maximum radiation along the axis perpendicular to the plane of the antenna. A patch antenna array will also generally radiate in the same way as a single patch and can be categorized as a broadside array.

The total electric field of such an array system would be equal to the electric field of a single element placed at the origin multiplied by a weighting factor called array factor. For a linear array with N elements, the array factor can be expressed as,

$$AF = \sum_{n=1}^{N} A_n e^{j(n-1)(kdcos\theta+\beta)} \tag{3.17}$$

It can be simplified as,

$$AF = \begin{cases} \sum_{n=1}^{M} a_n \cos[(2n-1)u] & N \; is \; even \\ \sum_{n=1}^{M+1} a_n \cos[(2n-1)u] & N \; is \; odd \end{cases} \tag{3.18}$$

The array factor is dependent on various features such as the number of elements, the spacing between elements, their relative magnitudes and phases. In Equation 3.17, 'k' is the phase velocity, 'd' is the spacing between two elements and β is the progressive phase shift. The coefficient a_n in Equation 3.18 is the relative magnitude of each element in the array. These variables can be obtained using the Dolph-Tchebysheff polynomials. The values of relative magnitudes determine the sidelobe and grating lobe levels. In order to determine the values of a_n, the following procedure is used [4].

1. Select the appropriate equation for array factor from Equation 3.18, if the number of elements N is even or odd.

2. Expand the array factor such that it depends only on the power of $\cos(u)$.

3. Choose a Tchebysheff polynomial of the order N-1 ($C_{N-1}(z)$)

4. Determine the point $z = z_0$ at which $C_{N-1}(z_0) = r_0$, where $r_0 = 10^{\frac{SLL}{20}}$. SLL represents the desired sidelobe levels in dB.

5. Substitute $\cos(u)$ with $\frac{z}{z_0}$ in step 2.

6. Equate the array factor to $C_{N-1}(z)$ and solve for coefficients a_n

Since a patch antenna array radiates maximally at broadside, the first maximum of the array factor will occurs when

$$\psi = kd\cos\theta + \beta|_{\theta=90^\circ} = 0 \tag{3.19}$$

To avoid the occurrence of grating lobes, the distance between individual elements should ideally be less than λ. Some antenna arrays have the ability to steer the main beam to point in a direction away from broadside with the help of external phase shifters fed to individual elements of the array and are termed as phased array antennas. This can be done by providing individual array elements with progressive phase shifts given by

$$\alpha_{\pm n} = \begin{cases} \mp \left(\frac{2n-1}{2}\right) kd\cos\theta_0 & \text{for even elements} \\ \mp (n-1)\, kd\cos\theta_0 & \text{for odd elements} \end{cases} \tag{3.20}$$

Equation 3.20 is used to point a beam θ_0 from broadside. If we have a planar array, whose main beam has to point in θ_0 from broadside(Z-axis) and ϕ_0 from X-axis, then the phases can be calculated as described below. Firstly, we need to calculate phases β_x depending on the number of elements using the equation that follows below.

$$\beta_{x_{\pm n}} = \begin{cases} \mp(p-1)kd\sin\theta_0\cos\phi_0 \\ \mp(2p)kd\sin\theta_0\cos\phi_0 \end{cases} \tag{3.21}$$

Next, we calculate β_y for elements along the y-axis, using equation given below.

$$\beta_{y_{\pm n}} = \begin{cases} \mp(p-1)kd\sin\theta_0\sin\phi_0 \\ \mp(2p)kd\sin\theta_0\sin\phi_0 \end{cases} \tag{3.22}$$

Now that we have individual phases of elements along x and y axis, we then add the two phases corresponding to the same element. This gives us a matrix of elements that provides us with phases for each element of the array and the corresponding tilt of the beam.

After having discussed the theory that is involved in the operation of a traditional patch antenna as well as an antenna array, we now proceed to demonstrate a single microstrip patch antenna. The next section consists of an example of a patch antenna

designed to operate at 200 MHz. The S-parameters, radiation characteristics, input impedance and other factors important in the design of an efficient patch antenna will be discussed.

3.2 HFSS Simulation of a Patch Antenna

In this section, we have designed a probe fed microstrip patch antenna and simulated it using a 3-D full wave electromagnetic simulator provided by Ansys - HFSS. The antenna is designed to have a resonant frequency f_r at 200 MHz. This frequency is chosen in order to demonstrate the size constraint an antenna faces as the resonant frequency lowers from GHz to MHz to KHz.The antenna is built on an FR-4 epoxy substrate with a dielectric constant of 4.5. Fig.3.5 shows a screenshot of the probe fed microstrip antenna designed in Ansys HFSS.

A rectangular patch made of a conducting material like copper sits on an FR-4 epoxy substrate having a thickness of 6mm. The patch has a width W=257mm and length L= 345.29mm. The substrate must be substantially larger than the dimensions of the patch. The whole structure sits on a metal ground plane that does not extend infinitely. The antenna is fed with a coaxial probe having a characteristic impedance of 50Ω. The probe is located at a distance of L/4 from one of the radiating slots. The location of the feed has an impact on the input impedance of the antenna. The inner conductor of the probe is drilled through the substrate and connected to the metal patch. The outer conductor is connected to the ground plane underneath the structure. A waveport is assigned to the free end of the coaxial cable to excite the antenna model.

The antenna is simulated in an airbox having radiation boundaries to obtain far-field results for analysis. To obtain accurate radiation results, the radiating boundaries are placed at least $\lambda/4$ from all conductive surfaces of the antenna structure. We also apply a mesh operation to limit the size of the tetrahedrons on the air box surface to no greater than $\lambda/6$.

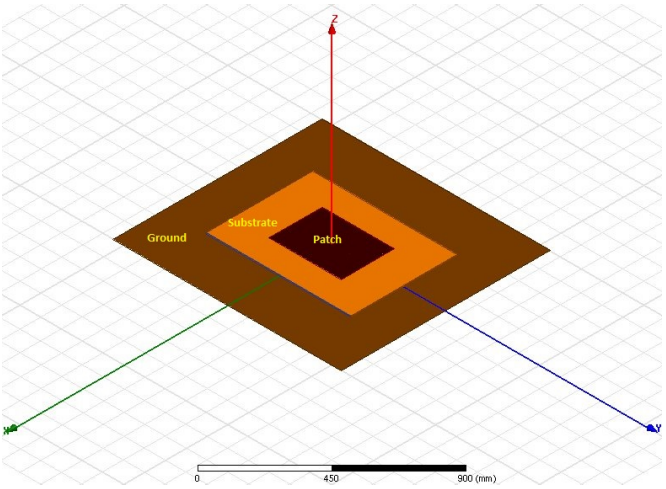

Figure 3.5: Probe Fed Patch Antenna

The designed antenna model is simulated over a frequency span from 100 to 300 MHz with 200 MHz being the center frequency. Since the antenna is a one port device, we obtain the return loss, which varies with frequency. A plot of return loss in dB versus frequency obtained from simulation in HFSS is shown in Fig.3.6. As can be seen, the antenna shows a resonant frequency of 200 MHz having a return loss of -25.25 dB. The bandwidth of the antenna having a return loss of -10dB approximately 10%.

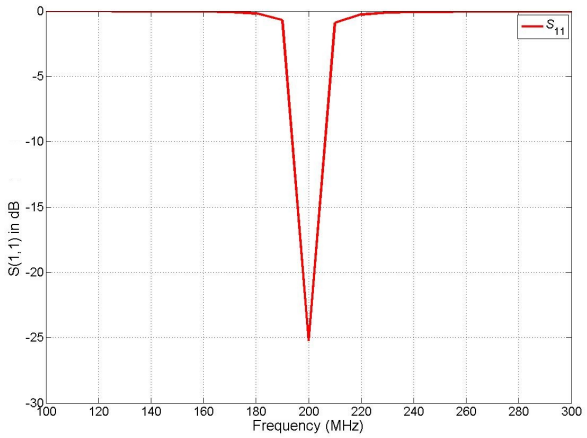

Figure 3.6: Return Loss obtained on simulation

The real part of the input impedance represents the power that is radiated from

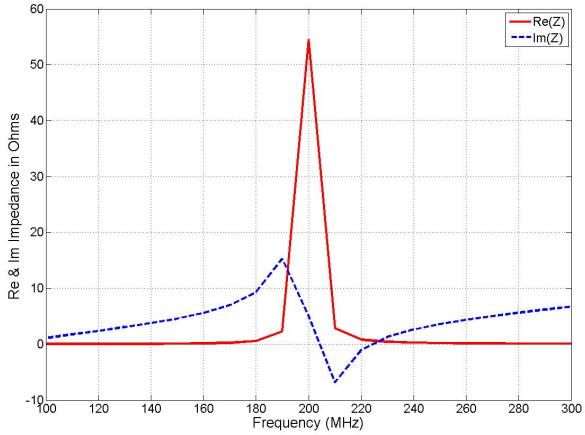

Figure 3.7: Input Impedance of Simulated Antenna Model

the antenna. The imaginary part is the non radiated power that represents the power that is stored in the near field of the antenna. The antenna input impedance shows a peak resonant resistance equal to 54.5Ω at 200 MHz. The reactance has a very small positive value of 5 ohms. This can be accounted for by the feed reactance due to the coaxial cable. The feed reactance is typically small for thin substrates and can be approximated as an average of the maximum and minimum reactance value when seen as a function of frequency. This can be observed from Fig.3.7 which shows the real and imaginary part of input impedance Z(1,1) plotted over frequency which appear to be symmetric about the resonant frequency. The reactive part is very close to zero at the resonance frequency. The finite reactance that is seen in the plot of input impedance is attributed to the feed reactance of the probe. TM_{010} is the dominant mode in the cavity of the patch and gives rise to resonance in the patch antenna. The length of the patch antenna is approximately half wavelength long. The E-fields along the non-radiating slots shown in Fig.3.8 give rise to boundary fields which eventually leads to radiation.

Antenna radiation pattern in the far-field was obtained on simulation. The gain of the antenna in the far field is obtained and plotted as a function of θ and ϕ. To analyze the radiation pattern of the patch antenna, normalized gain in dB was plotted on a

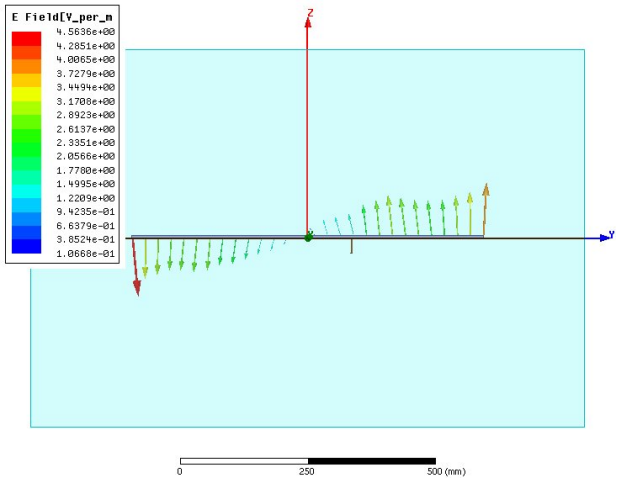

Figure 3.8: Current densities along the length of the non-radiating slots

polar plot for $0° \leq \theta \leq 360°$. The radiation patterns are plotted in the two principle planes i.e $\phi = 0°$ and $\phi = 90°$ as displayed in Fig.3.9.

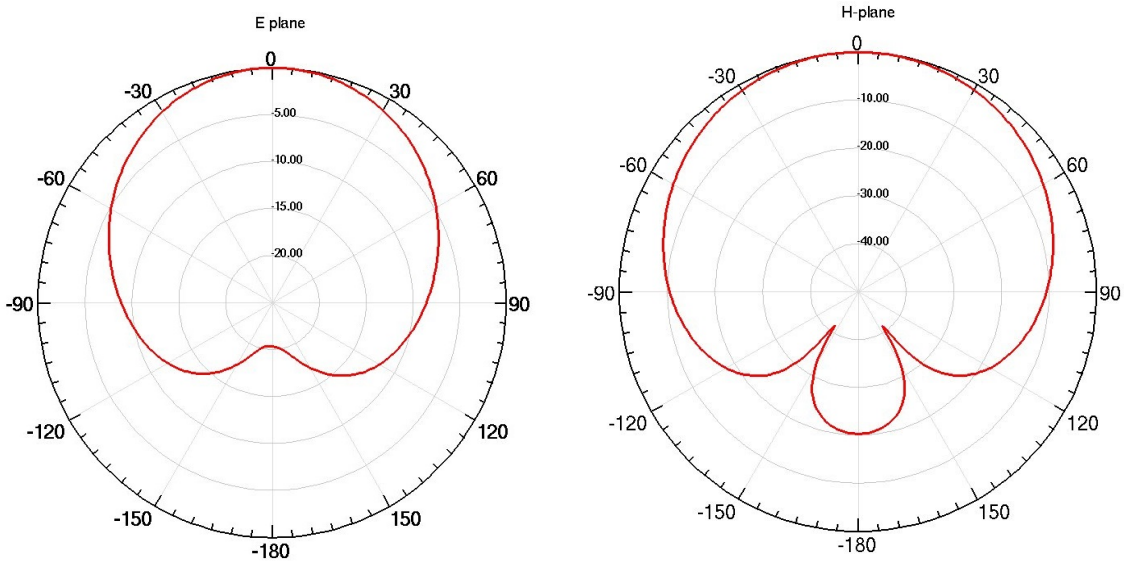

(a) E-plane($\phi = 90°$) (b) H-plane($\phi = 0°$)

Figure 3.9: (a) 2D radiation pattern in principal planes (ϕ=0,90 degrees)

Patch antennas show a directional antenna pattern with most of its energy radiating in the broadside i.e 90° from the plane of the antenna structure. From Fig.3.5 we can see that the antenna structure lies in the X-Y plane with its length along the Y-axis and radiation mostly occurs in the positive Z-direction. The radiation pattern

of the patch antenna can also be analyzed by plotting directivity in dB as a function of θ and ϕ. As can be observed from Fig.3.10, the maximum directivity of 6.24dB is obtained in the broadside direction.

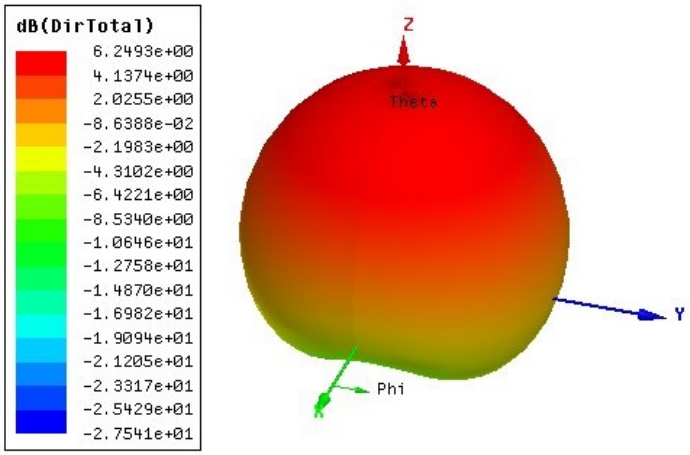

Figure 3.10: Directivity of simulated antenna model

A patch antenna operating at 200 MHz is designed in this section. The patch is observed to be at least one fourth of a meter long. The patch antenna is observed to be very narrowband as discussed above. The antenna radiates with a broad radiation pattern directed perpendicular to the plane of the antenna.

Since patch antennas are very popular in modern communication systems, there is a need to miniaturize the antenna structure in order for it to be accommodated in the small communication circuits. This issue was addressed by Al$\grave{u}$ et al [5] in 2007, when he suggested that the dielectric substrate used in a traditional patch antenna be partially replaced by SNG/DNG metamaterial slabs. The section below outlines some of the findings of Al$\grave{u}$ in his publication.

3.3 Discussion of Metamaterial Inspired Patch Antenna

In 2007, Andrea Al$\grave{u}$ et. al., introduced a novel method which involved partially replacing the dielectric substrate that fills the cavity beneath the patch element with metamaterials [5]. The authors of this publication suggested that the cavity under

the patch can be partially filled with a single negative (either ϵ or $\mu < 0$) or double negative metamaterial (ϵ and $\mu < 0$) slab along with a double positive dielectric slab (Fig.3.11). The ratio of the two media underneath the patch was referred to as filling factor (η) by the authors.

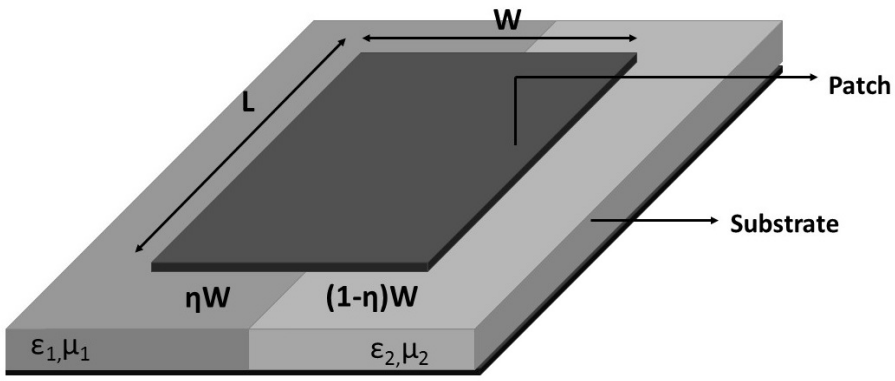

Figure 3.11: Patch antenna partially filled with metamaterial slab

The inhomogeneous substrate under the patch excited a modified TM_{0m0} which helped in reducing the size of the patch by a considerable amount. The resonant frequency of this modified TM_{0m0} mode was given by the following dispersion equation as stated in [5]:

$$\frac{k_1}{\omega\mu_1}\tan\left[k_1\eta W\right] = -\frac{\omega\varepsilon_2}{k_2}\tan\left[k_2(1-\eta)W\right] \tag{3.23}$$

where $k_i = \omega\sqrt{\varepsilon_i\mu_i}$. The resonant frequency supported by this modified TM mode is seen to be a function of the filling factor η. This resonant frequency was referred to as the subwavelength frequency as it did not correspond with the dimensions of the patch element.

Another such publication [17] proposed patch antenna structures that were similar to that suggested in [5] . The authors of this paper proposed an algorithm to design a rectangular patch antenna loaded with a single negative metamaterial medium. For a substrate comprised of Mu-negative metamaterial, $k_1\eta W$ lies between 135° and 180°.

μ_1,ϵ_1, W and ϵ_2 are chosen such that the product $k_1\eta W$ lies in the range. The remaining variables can be chosen accordingly to obtain the desired resonant freqency. Similarly, if the metamaterial under the patch is an epsilon-negative medium, $k_1\eta W$ lies between 180° and 225°. These proposed patch antenna structures radiate in the broadside direction like a traditional patch antenna. Patches loaded with metametarials undergo significant reduction in size.

Inspired from these, and several other publications, the effects of meta-substances on patch antennas were studied in great detail. In the chapter that follows, different metamaterial structures have been engineered and tuned to obtain appropriate single negative or double negative behavior of ϵ_r and μ_r that will be most suitable to be used in conjunction with a patch antenna. In addition, an attempt will also be made to substantially decrease the dimensions without compromising radiation aspects, performace and efficiency of the antenna model.

CHAPTER 4: PROPOSED METAMATERIAL STRUCTURES-DESIGN AND SIMULATION

The previous chapters dealt in great detail with the development of metamaterials and a theoretical discussion on properties possessed by such meta-structures. Additionally, the advantages and disadvantages of microstrip antennas have also been discussed and the notion of using meta-materials in conjunction with patch antennas to address the issue of size constraints was also touched upon. This chapter discusses different meta-materials designed to be integrated with a traditional microstrip patch antenna. Two main geometries have been considered and finely tuned to exhibit negative response of permittivity and/or permeability; the split ring and thin wire multiple turn spiral.

The geometries that have been suggested to be included in the patch antenna topology will be modeled and simulated in Ansys HFSS. Simulation results provide transmission-reflection coefficients extracted through an extensive electromagnetic computation done on the 3D model. Several methods have been discussed to extract permittivity and permeability from S-parameter response [32] [28]. One method that has been applied in the design procedure has been proposed by Zsolt Szabo*ó* et al and is discussed in the next section.

4.1 Extraction Method to Obtain Effective μ_r and ϵ_r

In order to extract μ_r and ϵ_r parameters from the designed structures, appropriate boundary conditions have to be satisfied. As such, these meta-structures are enclosed in a parallel plate waveguide whose side walls are made of magnetic boundaries and the top and bottom surfaces assigned perfect electric boundaries as shown in Fig.4.1. The H fields travel along the X-axis and the E fields travel along the Z-axis. The remaining

walls of the rectangular waveguide are assigned as waveport excitations with vertically oriented E-fields. Since this structure has two ports, we can obtain S-parameters of a metamaterial cell placed inside the waveguide. The S-parameters obtained from simulation can be further used to extract ϵ_r and μ_r parameters exhibited by the metamaterial structure under test. Zsolt Szab*ó* et al proposed a method to extract

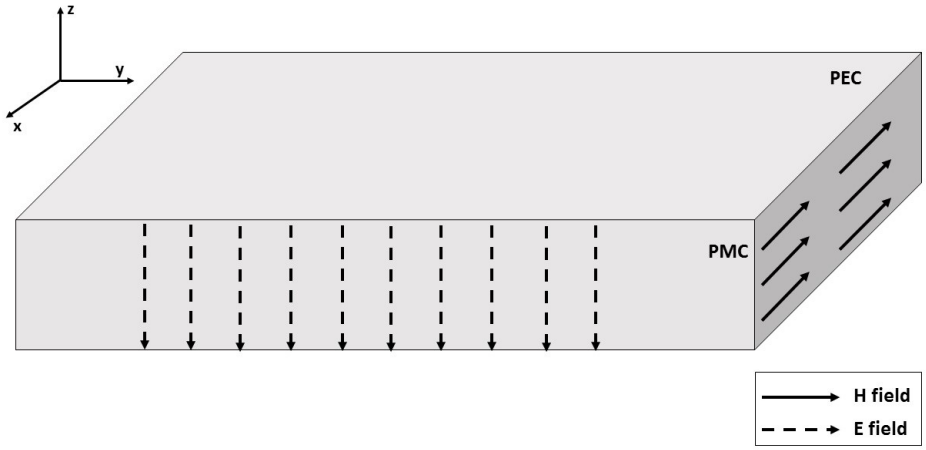

Figure 4.1: Parallel plate waveguide structure

ϵ and μ paramaters from metamaterials based on the Kramer's-Kronig relationship [28]. S-parameters are obtained by placing a metamaterial unit cell in a rectangular waveguide. For this algorithm, we need to consider the thickness of the cell. The thickness here refers to the length of the unit cell enclosed in the waveguide along the direction of propagation. If there are multiple unit cells in the waveguide, the effective thickness is the sum of the lengths of all the unit cells. To obtain accurate transmission-reflection parameters, the observation points should be far enough from the surface of the metamaterial cell to avoid near-field effects.

S parameters can be related to the wave impedance and refractive index for a plane wave incident on the metamaterial structure. The return loss S(1,1) and insertion loss S(1,2) can be represented by formulas given by equations 4.1 and 4.2.

$$S_{11} = \frac{R_{01}(1 - e^{i2N_{eff}k_0 d_{eff}})}{1 - R_{01}^2 e^{i2N_{eff}k_0 d_{eff}}} \tag{4.1}$$

$$S_{12} = \frac{(1 - R_{01}^2)e^{iN_{eff}k_0 d_{eff}}}{1 - R_{01}^2 e^{i2N_{eff}k_0 d_{eff}}} \tag{4.2}$$

R_{01} here, is a function of Z_{eff} which is the complex wave impedance given by the equation given below.

$$R_{01} = \frac{Z_{eff} - 1}{Z_{eff} + 1} \tag{4.3}$$

The complex refractive index is given by $N_{eff} = n_{eff} + ik_{eff}$, n_{eff} is the refractive index and k_{eff} is the extinction coefficient, i.e. the imaginary part of the complex refractive index N_{eff}. All the terms mentioned above are a function of angular frequency ω. Therefore, Z_{eff} can be expressed as follows:

$$Z_{eff} = \pm\sqrt{\frac{(1 + S_{11})^2 - S_{12}^2}{(1 - S_{11})^2 - S_{12}^2}} \tag{4.4}$$

Also,

$$e^{iN_{eff}k_0 d_{eff}} = \frac{S_{21}}{1 - S_{11}R_{01}} \tag{4.5}$$

The complex refractive index is given by,

$$N_{eff} = \underbrace{\frac{\mathrm{Im}[\ln(e^{iN_{eff}k_0 d_{eff}})] + 2m\pi}{k_0 d_{eff}}}_{n_{eff}} + i\underbrace{\frac{-\mathrm{Re}[e^{iN_{eff}k_0 d_{eff}}]}{k_0 d_{eff}}}_{k_{eff}} \tag{4.6}$$

the integer 'm' in this Equation 4.6, is the branch index. Applying the Kramer's-Kronig relation to k_{eff} to simplify it further, we can obtain the real part of N_{eff} over a defined range of frequencies. Thus, [28] states the following relations for N_{eff} and Z_{eff} in terms of μ_{eff} and ϵ_{eff};

$$N_{eff} = \sqrt{\varepsilon_{eff}\mu_{eff}} \tag{4.7}$$

$$Z_{eff} = \sqrt{\frac{\mu_{eff}}{\varepsilon_{eff}}} \tag{4.8}$$

The effective permittivity and permeability can be calculated using the following relations:

$$\varepsilon_{eff} = \frac{N_{eff}}{Z_{eff}} \tag{4.9}$$

$$\mu_{eff} = N_{eff} Z_{eff} \tag{4.10}$$

Following the steps mentioned above, the authors of [28] created an algorithm and implemented it in MATLAB to extract effective μ and ϵ values [27]. The inputs given to this code to extract these parameters are:

1. Frequency in GHz: This code requires a sufficient number of frequency points to obtain accurate parameters. Since this algorithm requires the use of Kramer's-Kronig integral, we need to provide S parameters obtained over large frequency range.
2. Magnitude of S(1,1)
3. Phase of S(1,1) in radians
4. Magnitude of S(1,2)
5. Phase of S(1,2) in radians
6. Effective length of the structure in meters.

On reviewing Szabó's extraction method, and establishing boundary conditions required for this parameter extraction method, these concepts are applied to the process of designing meta-materials. Different geometries were analyzed to be integrated into a patch antenna topology. These structures were engineered and finely tuned to exhibit the desired response of relative permittivity and permeability. While designing these metamaterials, considerable attention was given to limit the size of the unit cells to avoid bulkiness of the modified patch antenna structures. The metamaterials were designed to operate at frequencies ranging from 100 MHz to 1 GHz, which

correspond to the desired subwavelength frequencies to be achieved by the proposed patch antennas.

4.2 Double Square Shaped Split Ring Resonator Design and Simulation

Motivated from conventional split ring resonators discussed by Pendry [22], a square shaped double split ring resonator structure, having resonance in the microwave frequency band, was designed and simulated with HFSS. Two concentric rings are placed on an FR-4 epoxy dielectric having ϵ_r equal to 4.5. The dielectric substrate on which the split rings are printed has a thickness of $\frac{1}{16}$ inch. The outer square ring has a length $\ell_\circ$ = 19mm and length of inner ring ℓ_i = 15 mm. The concentric rings are separated by a small distance of 1.25mm. Each of these rings is 0.75mm thick and have small gap that provides capacitance to the split ring structure. The gaps added in each ring produces a capacitance that each large enough that facilitates the continuous flow of current in each of the rings. This split ring resonator structure can be represented by an equivalent LC resonator circuit which provides resonance to the structure. It is interesting to note that the natural resonance of this structure will lie at round 1.5 GHz. The lengths of the rings, gap and trace widths were optimized in order to obtain a desired resonance from the structure. Modifying these dimensions of the split ring structure consequently changes the inductance and capacitance possessed by it. One way to lower the resonant frequency of the structure is to increase the capacitance in the circuit by including additional capacitances to the gaps in the rings. Hence, two external capacitors of 4.7pF have been inserted into the gaps of the two rings. Thus, the proposed split ring resonator structure now resonates at 300 MHz. The model of the split ring resonator also consists of a capacitively loaded vertical strip that is 4mm wide. This square shaped double split ring resonator structure is shown in Fig.4.2.

To extract ϵ_r and μ_r parameters from the designed split ring structure, the model is placed in a parallel plate waveguide transmission line as shown in Fig.4.3. Magnetic

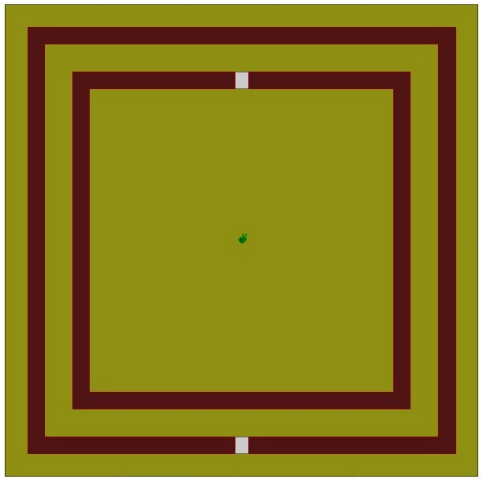

Figure 4.2: Double split ring resonator (DSRR) structure

boundaries are applied parallel to the cell with the magnetic field directed along the X-axis. Perfect electric (PEC) boundaries are applied to the walls of the waveguide perpendicular to the structure along the Z- axis. An incident wave is applied along the Y-axis by assigning waveports to the remaining walls of the rectangular waveguide. The wave is excited from the the positive Y direction (port 1 to 2), and the split ring resonator structure is placed in the center of the waveguide. A vertical post is also added to the back of the split ring structure; the post is not connected to either of the PEC walls. The shorting post was added in the later part of the research in order drive energy from the ground plane and obtain antenna resonance at 300 MHz.

The split ring resonator exhibits resonance at 300MHz which can be deduced from the plot of S_{11} and S_{12} that is given in Fig.4.4. S(1,2) represents transmission parameter which measures the amount of power transmitted through the waveguide with metamaterial structure placed in the center while S(1,1) represents its reflection coefficient. From Fig.4.4, we can observe that S(1,2) lies above -2dB over most of the frequency sweep, indicating that transmission occurs in the waveguide irrespective of the presence of the metamaterial structure. As we know, the H field is applied perpendicular to the simulated structure. However, at resonant frequency due to the presence of negative permeability exhibited by the structure, H field is repelled by

the structure due to which S(1,2) changes to −10.9 dB at 300 MHz. Reflection in the waveguide in the presence of metamaterial cell is depicted by S(1,1) trace in the figure whose value is −2.9dB at resonant frequency.

In order to extract ϵ and μ parameters from the structure, we need to obtain magnitude and phase (in radians) of S-parameters. Plots of magnitude and phase of the S(1,1) and S(1,2) versus frequency were obtained as shown in Fig.4.6 and Fig.4.7, and used to extract ϵ and μ at resonant frequency using Szabo's code [27] mentioned earlier.

Fig.4.8 shows the extracted values of effective ϵ and μ parameters. The designed split ring resonator structure shows strong magnetic resonance with μ= −15.89 at 300 MHz. The vertical post added to the structure does not exhibit a negative permittivity at the 300 MHz. In fact, the resonance of the vertical post exhibits lies at a much higher frequency at which negative permittivity will be observed. However, adding the trace on the rear side improves the permeability exhibited by the split ring structure. It can be also observed that the metamaterial structure shows a positive ϵ value of 4.38 at this frequency.

The double split ring resonator metamaterial unit cell exhibits a strong negative

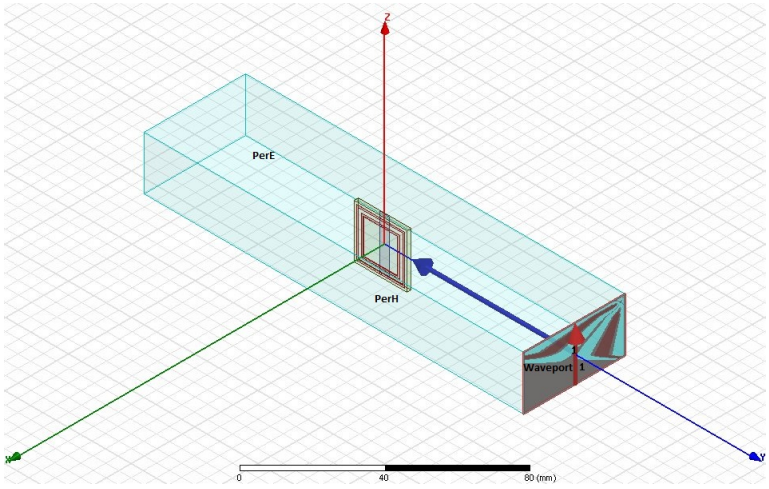

Figure 4.3: Waveguide to simulate DSRR metamaterial

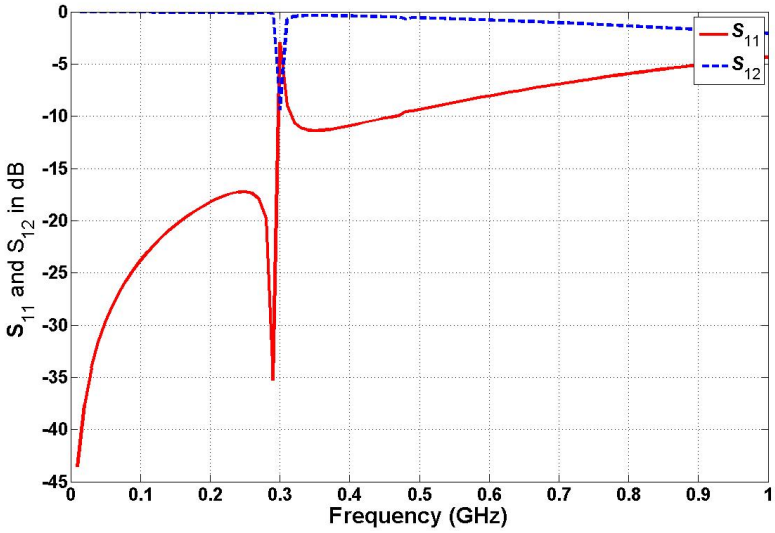

Figure 4.4: S parameters(dB) of simulated DSRR metamaterial

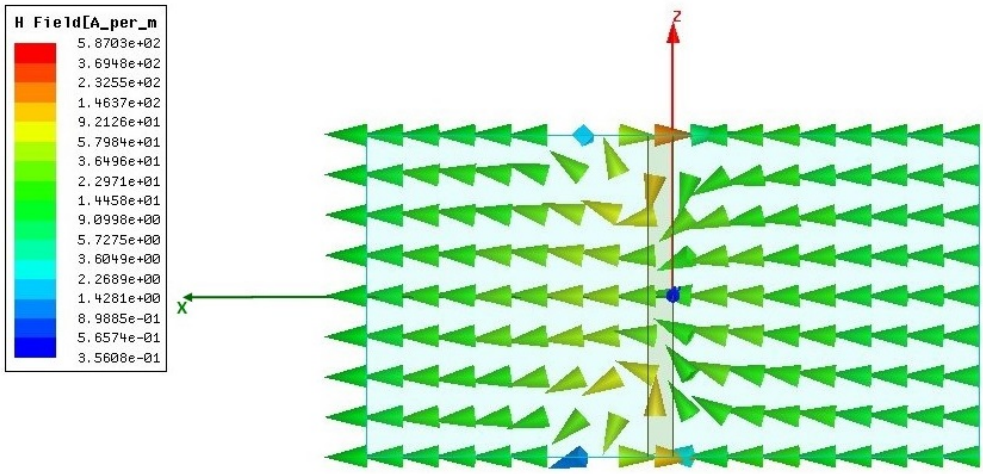

Figure 4.5: H field applied to the double split ring resonator

permeability at 300MHz and positive permittivity values over the entire simulated range of frequencies. It is interesting to note that the metamaterial structure designed is very electrically small, on the order of $\lambda/50$, compared to the dimensions in free space at the resonant frequency.

Next we wish to design a metamaterial structure that possesses double negative

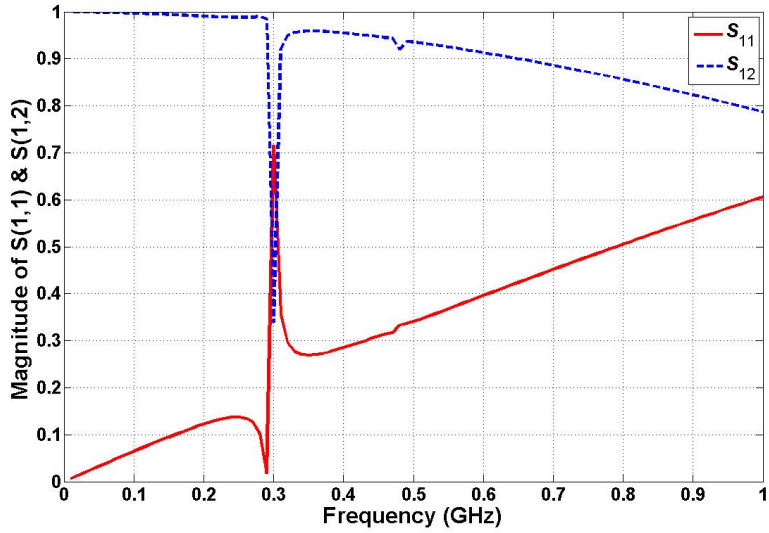

Figure 4.6: S parameters(Magnitude) of simulated DSRR structure

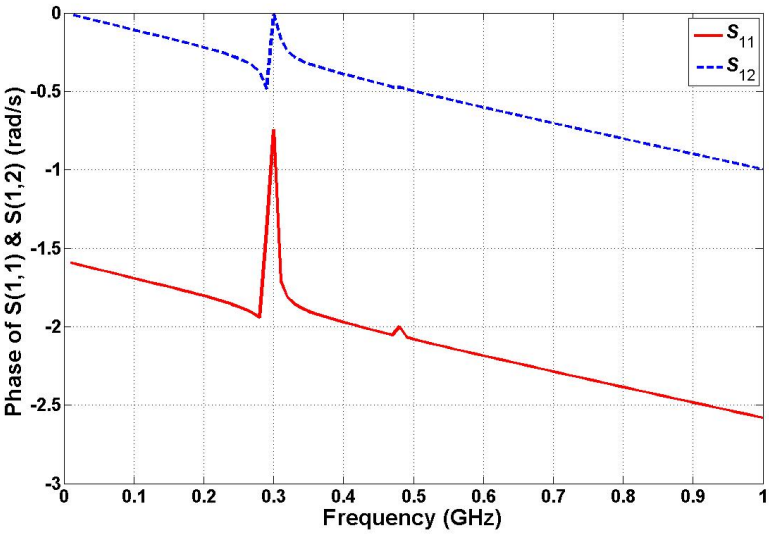

Figure 4.7: Phase of S parameters of simulated DSRR structure

values of permittivity and permeability. We can obtain double negative properties from the split ring structure by simply adding a shorting rod to the back of the substrate. But loading this structure into a patch antenna would lead to shorting of the patch with the ground plane and the resulting structure will not represent a patch antenna. Hence, we explore the possibility of simultaneously simulating a partially

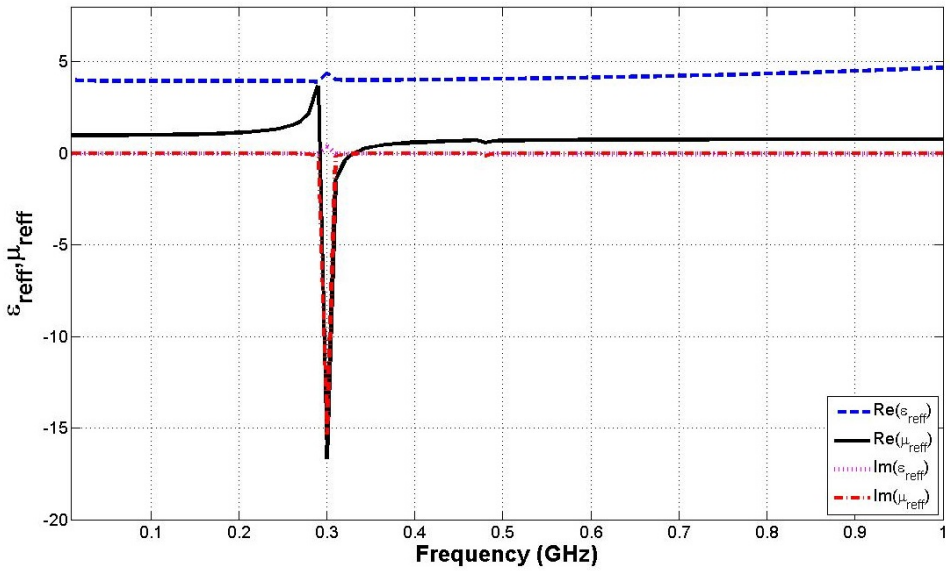

Figure 4.8: Extracted graph of ϵ and μ over frequency exhibited by DSRR structure

polarized shorting rod with a multiple turn spiral structure in the next section.

4.3 Spiral Resonating Metamaterial Structure

The next proposed structure consists of a geometry that includes the concept of using a spiral resonator and a thin wire in the same structure to exhibit double negative response. Inspired from a structure proposed in [19], a spiral structure having multiple turns was proposed. First, a five turn double sided spiral structure was designed and a thin wire was later added to the spiral geometry as shown in Fig.4.9. The metal traces were 0.4mm thick and were printed on either sides of an FR-4 epoxy dielectric slab which is 1/16th of an inch thick. This proposed unit cell is an almost square structure of length 12.7mm and width 12.3mm and the spiral rings are separated by a gap of 0.6mm. The thin vertical wire printed on one side of the dielectric slab is shorter than on the other side of the structure. This thin strip of copper is intentionally shortened in order to obtain a desired resonant frequency.

The designed spiral structure is placed in the center of a parallel plate waveguide in a manner similar to the split ring resonator discussed previously. A perfect magnetic boundary is applied to the walls parallel to the structure and an electric boundary is

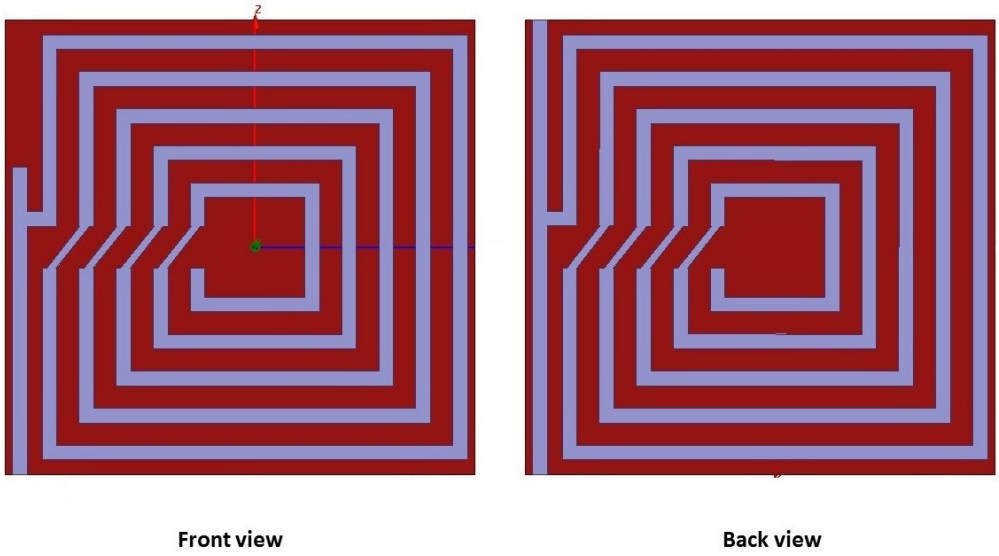

Figure 4.9: Double sided spiral structure designed to exhibit negative ϵ and μ

applied to the top and bottom walls of the waveguide, such that the vertical E fields polarize the vertical strips of copper. It is to be noted that rectangular waveguide and the designed unit cell have the same height, such the the longer vertical trace is shorted to the PEC walls of the waveguide. The remaining two walls are assigned as waveports. Fig.4.10 below shows S(1,1) and S(1,2) obtained over a several frequency points ranging from 0.1 GHz to 1 GHz .

As you can observe from S parameters shown in Fig.4.10, S(1,1) is very high at most frequencies that were swept. Also, observing the transmission parameter S(1,2) plotted against frequency, the insertion loss shows an exact opposite behavior. This tells us that most of the energy entering the waveguide is reflected back and hence transmission of energy through the waveguide is significantly reduced. The values of magnitude and phase of S(1,1) and S(1,2) obtained from simulation are imported into MATLAB along with the length of the structure and the resulting extracted parameters are displayed in Fig.4.12. Thus, the metamaterial exhibits narrowband negative μ_r around 200MHz and a very wideband strong negative ϵ_r over most of the simulated frequency range.

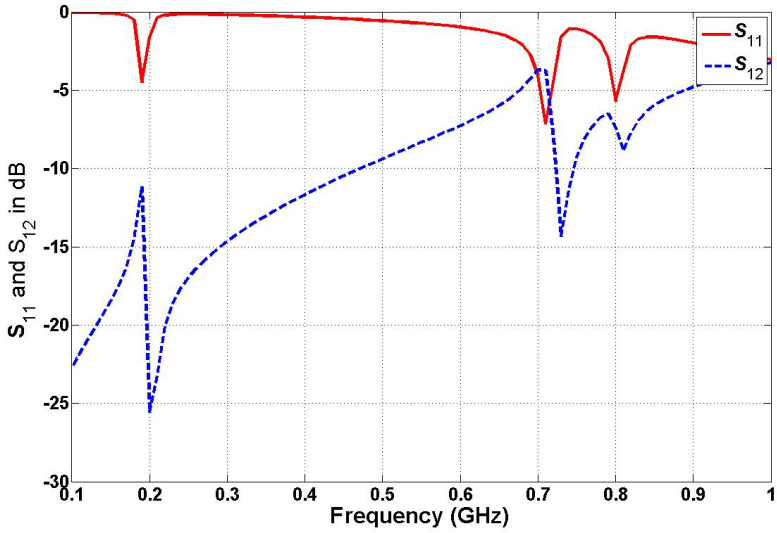

Figure 4.10: S-parameters of double sided spiral structure shown in Fig.4.9 obtained on simulation

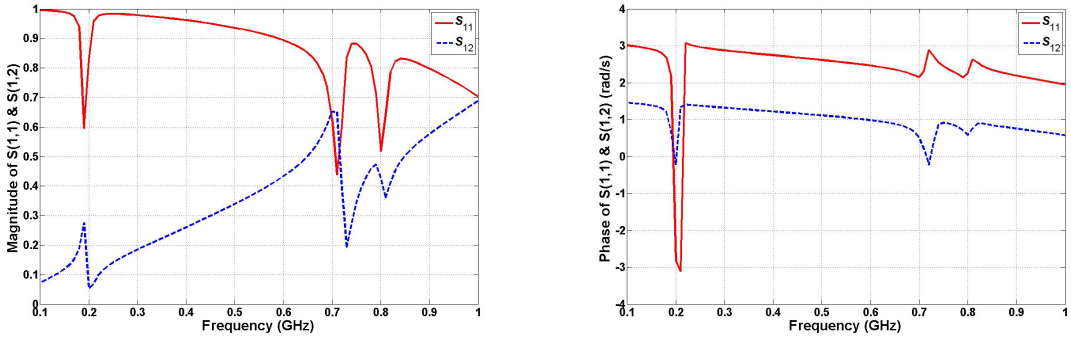

(a) Magnitude of S-parameters (b) Phases of S-parameters

Figure 4.11: Magnitude and phase of S parameters of spiral structure shown in Fig.4.9 used for extraction of ϵ and μ

Fig.4.12 shows that at 200MHz, the structure exhibits negative effective permeability which is very narrow band with its peak at -8.5. This negative μ_r can be attributed to the spiral geometry of the structure. From the same figure, it can also be observed that there is a very strong negative ϵ present due to the longer metal wire present on the back side of the substrate which is vertically polarized by the E fields in the waveguide. Around 200 MHz, we observe a sharp oscillation of ϵ_r from negative to positive and back which maybe caused by the partially polarized shorter

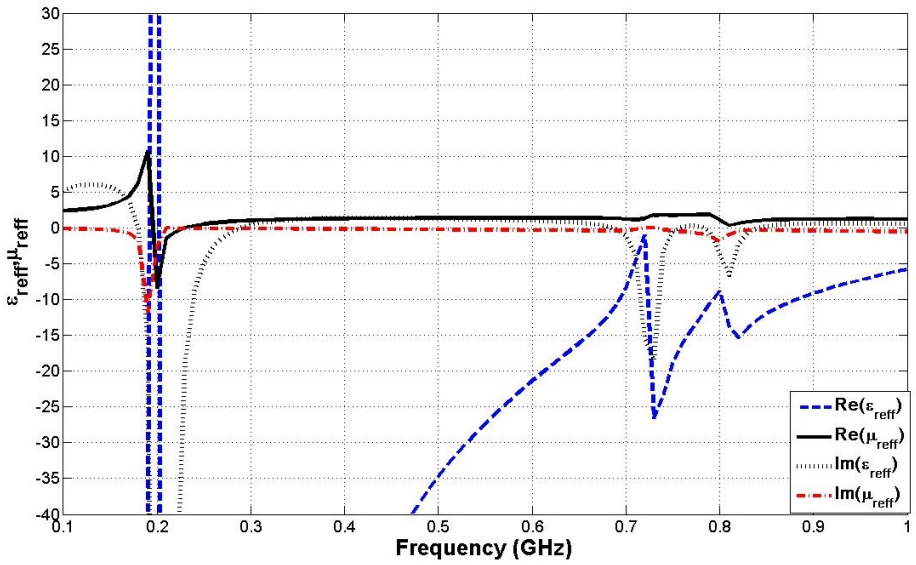

Figure 4.12: Extracted negative μ and ϵ of double sided spiral structure shown in Fig.4.9

vertical trace present on the front side of the substrate. The shorted vertical trace makes contact with one of the PEC walls of the waveguide. The fields inside the trace tend to couple from the open end of the trace to the other PEC wall of the waveguide. This gives rise to some additional capacitance in the structure which causes this sharp transition in the ϵ_r response that has been discussed earlier. Overall, a wide negative permittivity response is observed over most of the frequency range, which is a typical behavior observed from vertically polarized thin wire medium discussed by Pendry [21].

The metal traces of the spiral resonator provide inductance and the gap between traces provide capacitance. The structure resonates due to this balanced L-C combination. The total capacitance of this circuit is given by,

$$C_{tot} = (N-1) \times C_0 \tag{4.11}$$

where C_0 is the Capacitance between two adjacent rings given by,

$$C_0 = 2\pi r_0 C_{pul} \tag{4.12}$$

C_{pul} here, is the capacitance per unit length. From Equation.4.11, we see that the total capacitance increases by increasing the number of turns. Hence by increasing the total capacitance, we can obtain a lower resonant frequency from the spiral resonator structure.

The metamaterial cell proposed above consists of a structure printed on a double sided copper clad dielectric slab. Hence, the next structure will be a modified version which will consist of a spiral resonator and metal trace printed on a single side of the dielectric slab. In order to obtain a low resonant frequency from the structure, a larger number of turns will be added to the structure. Additionally, the dimensions of the rings and the spacing between them will be optimized to reach a desired resonant frequency. While doing so, equal attention will be paid to maintain an overall size limit.

The metamaterial cells are designed to be placed between the metal patch and the ground plane. As such, the area under the patch maybe utilized to optimize the dimensions of the metamaterial unit cells. The unit cell thus designed, will be wider and its height will be restricted to avoid bulkiness of the resulting patch antenna model.

The sections that follow discuss a single sided metamaterial unit cell whose length is almost twice its height. The structure comprises a multi-turn spiral geometry and a thin vertical trace both printed on the same side of the dielectric substrate. The length of the vertical trace influences the relative permittivity response exhibited by the unit cell. Addition of multiple turns to the spiral, tunes the relative permeability response to the desired frequency.

4.3.1 Single Sided Spiral Structure with Capacitively Loaded Vertical Trace

This section proposes a single sided metamaterial unit cell whose length and height are 20.145mm and 10.85mm respectively. The resulting metamaterial structure is made up of 10 concentric rectangular rings connected together with thin metal traces thus forming a spiral geometry. The gap between two consecutive rings is greater along its length (0.7mm) and less along its height (0.25mm). This structure also consists of a thin vertical metal trace conjoined to the spiral geometry with a small metal trace. The trace width of the whole structure is 0.25mm. The vertical trace is shorter than the height of the the unit cell by a distance of 0.125mm. The gap between two consecutive rings is greater along its length (0.7mm) and less along its height (0.25mm). The trace made contact with one of the electric walls of the waveguide in which the unit cell is placed. This combination of spiral geometry and vertical trace is placed on an FR-4 epoxy ($\epsilon_r = 4.5$) substrate of $\frac{1}{32}$ inch thickness. The single spiral structure described above is shown in Fig.4.13.

The spiral structure is also simulated in similar conditions in a parallel plate waveguide, with H fields penetrating through the metamaterial structure. Observing Fig.4.14 we see that the wave vector is excited in the negative Y direction. The incident wave first interacts with the spiral section of the structure circulating towards the vertical trace. As we know, one end of the vertical trace makes contact with one of the electric walls of the parallel plate waveguide. This gives partial polarization in the vertical trace and also builds some additional capacitance between the free end of the trace and the second PEC wall.

Fig.4.15 shows the simulated results of S(1,1) and S(2,1) in dB simulated over frequencies ranging from 0.1GHz to 1GHz. From S-parameter results, we observe that the metamaterial structure is able to achieve resonance at multiple frequencies within the simulated range i.e 0.25, 0.56 and 0.84 GHz . At these frequencies, we observe that S(2,1) varies from -7 to -10 dB. Similarly the return loss S(1,1) maintains values

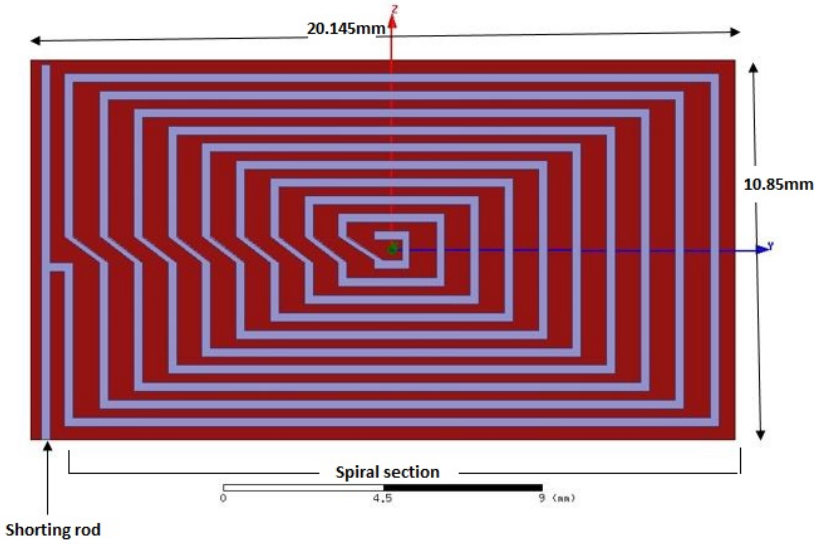

Figure 4.13: HFSS model of single sided spiral resonator metamaterial with capacitively loaded vertical trace

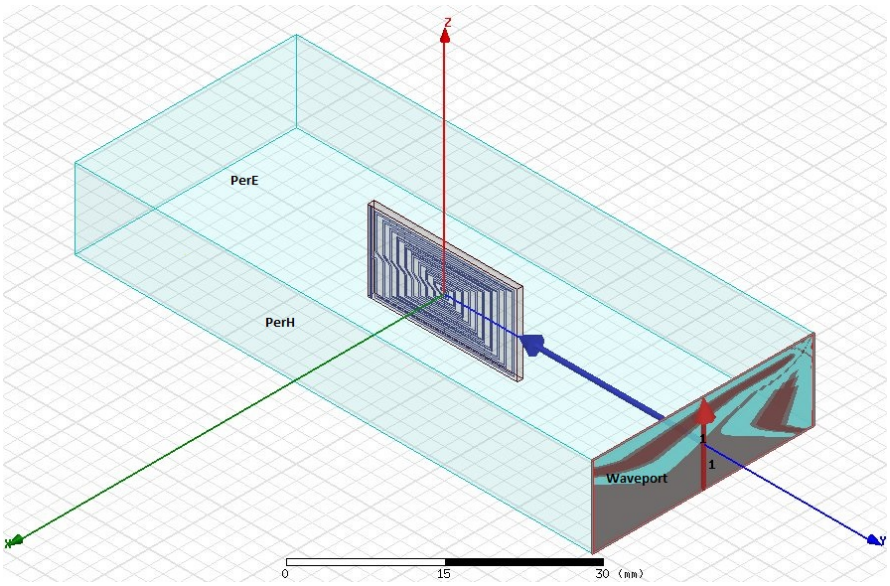

Figure 4.14: Single sided spiral resonator metamaterial structure in parallel plate waveguide

around −2 dB. Under normal conditions, the H fields in the waveguide travel in the negative X-direction, penetrating through the metamaterial. However at resonant frequencies, the metamaterial exhibits negative characteristics and hence the direction of H fields is reversed. Thus, we obtain transmission and reflection parameters as

depicted in Fig.4.15.

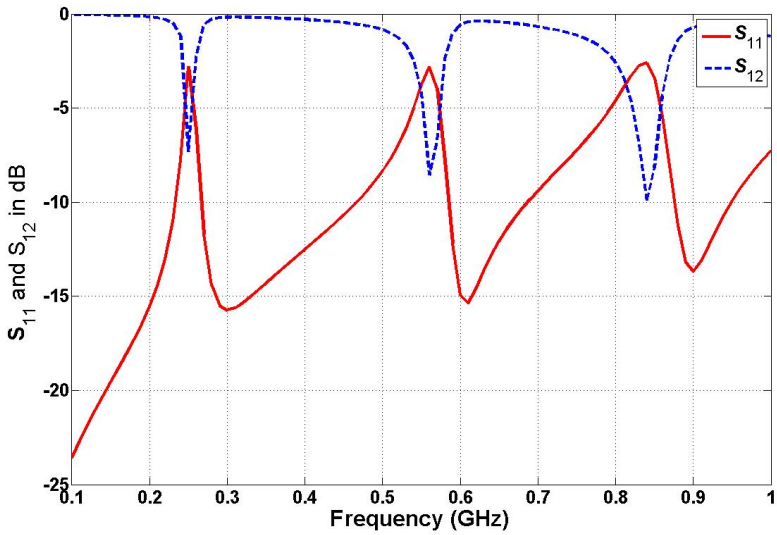

Figure 4.15: Simulation results of S parameters of spiral resonator from Fig.4.13

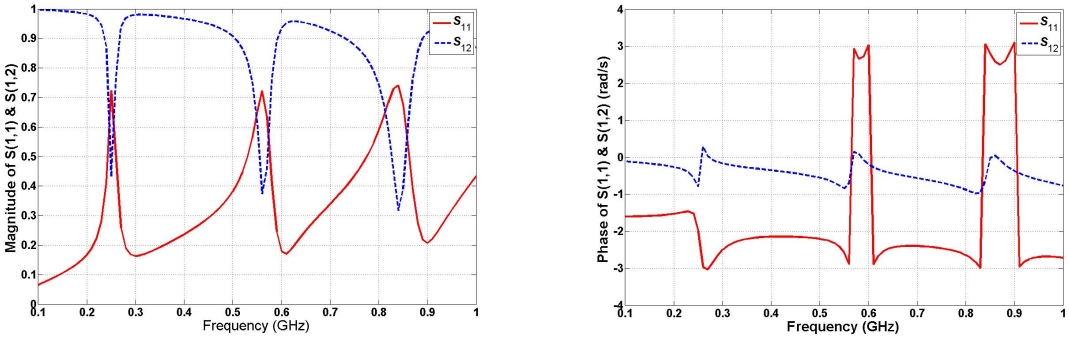

(a) Magnitude of S-parameters (b) Phases of S-parameters

Figure 4.16: Simulation results of magnitude and phase of S parameters of spiral resonator from Fig.4.13 used for extraction of ϵ and μ

Fig.4.16 gives a plot of the magnitudes and phases of S-parameters that contribute to the extraction of effective values of μ_r and ϵ_r exhibited by the single sided spiral metamaterial structure. From Fig.4.17, we can observe that the metamaterial structure exhibits periodic strong negative relative permittivity response at resonant frequencies (0.26, 0.57 and 0.85 GHz). This periodic behavior of effective relative permittivity can be attributed to the vertical trace present in the metamaterial unit

cell. It can be also observed that the structure has relative magnetic permeability $\mu_r = -5.005$.

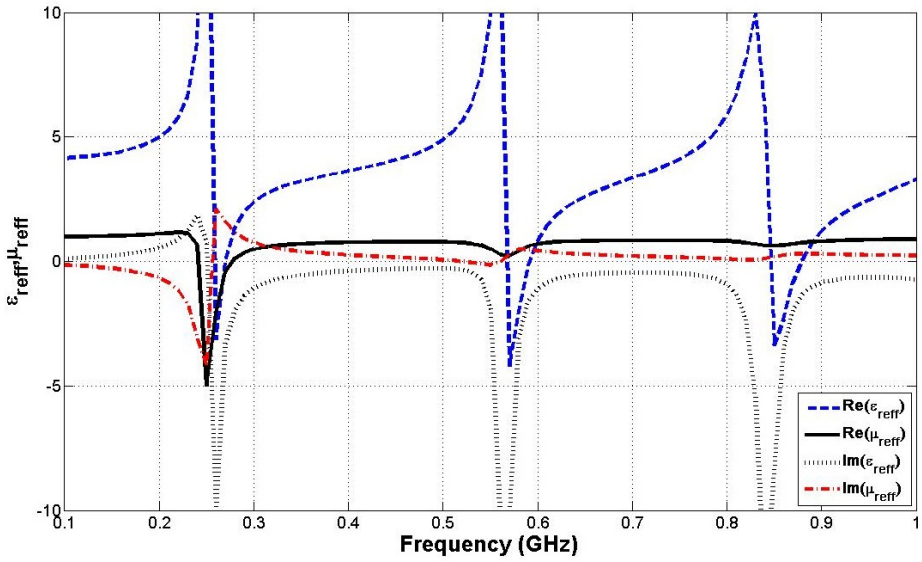

Figure 4.17: Extracted ϵ and μ parameters of metamaterial structure shown in Fig.4.13

When the direction of incident wave applied to the structure in Fig.4.14 is reversed (i.e in the positive X direction), the incident wave first interacts with the vertical trace before entering the spiral part of the metamaterial structure. As the wave travels through the spiral traces, it tends to acquire losses from the resonating structure.

4.3.2 Single Sided Spiral Resonator Structure with Shorted Vertical Trace

The same structure was modified wherein the length of the vertical trace is equal to the height of the designed unit cell. Both ends of the vertical trace makes contact with the two electric walls of the waveguide as shown in Fig.4.20. A very strong E field is applied to the vertical trace and induces a current that continuously flows between the two parallel electric walls using the metal vertical trace as a medium.

From Fig.4.21, we can observe that resonance occurs at three frequencies when simulated from 100 MHz to 1 GHz i.e 0.25GHz, 0.56GHz and 0.84GHz. Fig.4.22 shows values of relative ϵ and μ extracted from the model from Fig.4.20. This structure

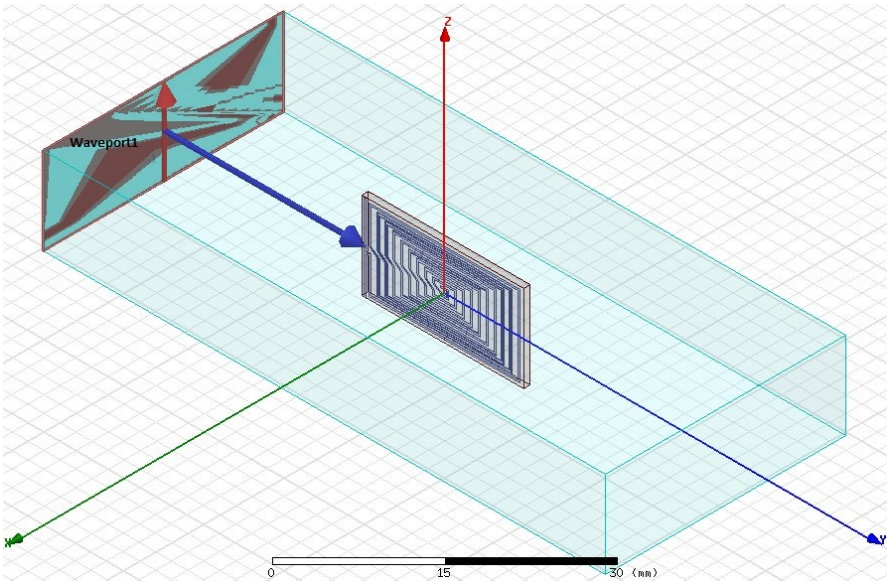

Figure 4.18: Incident wave applied in opposite direction

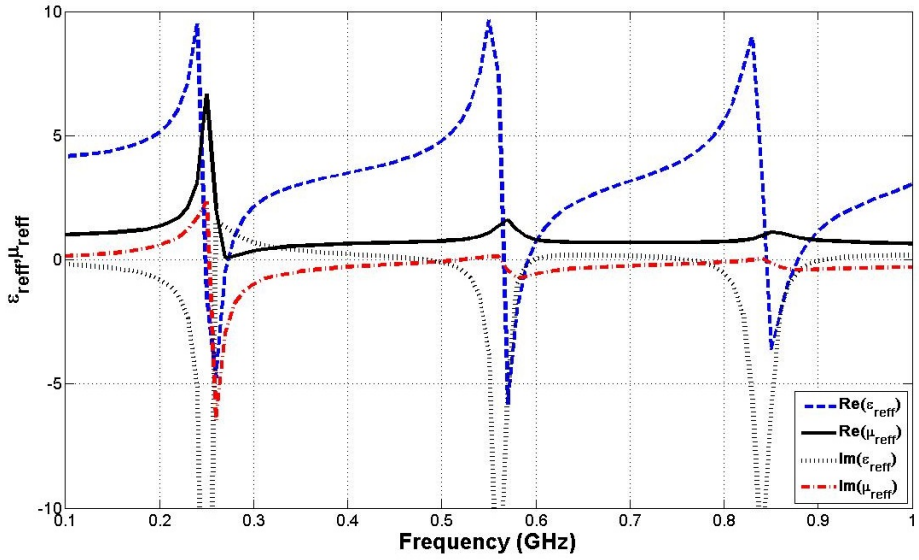

Figure 4.19: Extracted graph of ϵ and μ v/s frequency for spiral structure shown in Fig.4.18

exhibits very high negative permittivity at 0.27 GHz that decreases at the next highest resonant frequency. It can be clearly concluded that the structure exhibits negative permittivity due to the presence of the shorted vertical trace included in the model. It can be observed that negative permittivity exhibited by the unit cell decreases as frequency increases and this relative permittivity will continue to weaken as the metal

trace nears its plasma frequency. Observing Fig.4.22 closely, it can be noted that the structure exhibits negative permeability at 0.25 GHz (μ_r=−7.219).

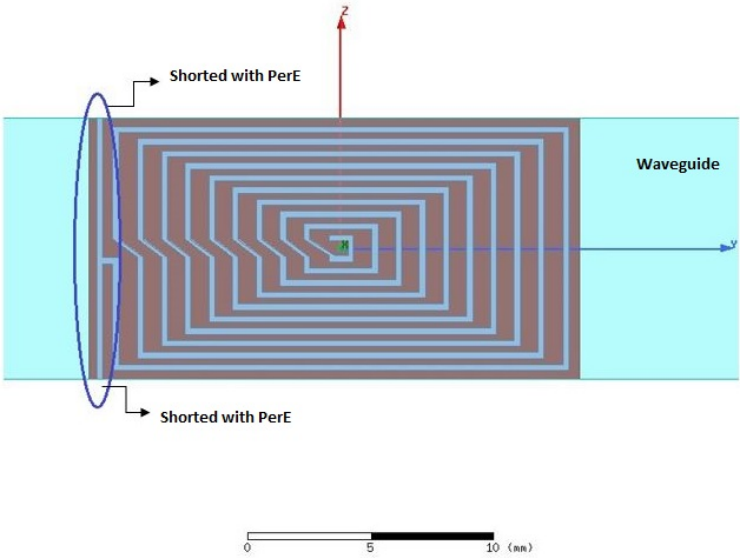

Figure 4.20: Single sided metamaterial cell with shorted vertical trace

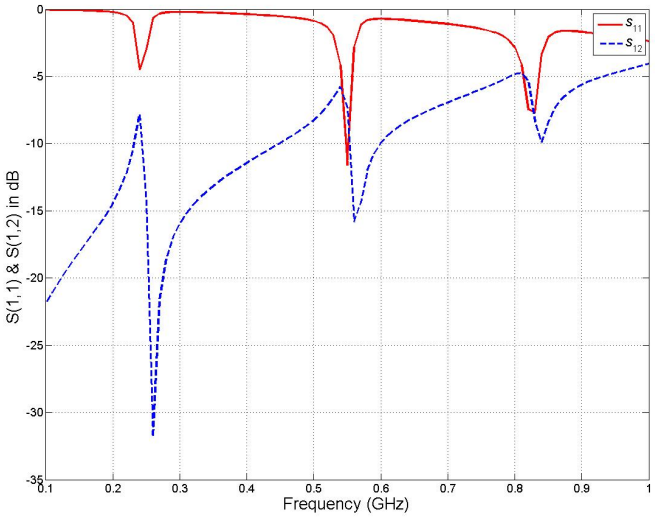

Figure 4.21: Simulation results of S parameters of spiral resonator from Fig. 4.20

4.3.3 Single Sided Spiral Resonator Structure with Unshorted Vertical Trace

The next modification of the spiral structure includes a vertical trace that does not make contact with either of the prefect electric walls of the rectangular waveguide

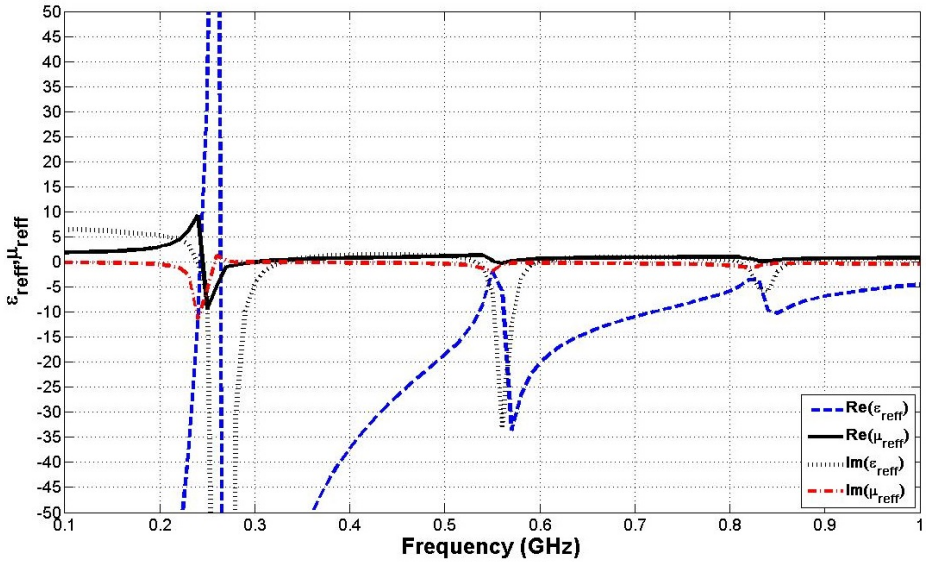

Figure 4.22: Extracted graph of ϵ and μ v/s frequency for spiral structure shown in Fig.4.20

(Fig.4.23). An incident wave is applied in the negative Y direction which first impinges upon the spiral section of the metamaterial before interacting with the vertical trace. Fig.4.24 shows the S-parameters obtained by simulating this model placed in a parallel

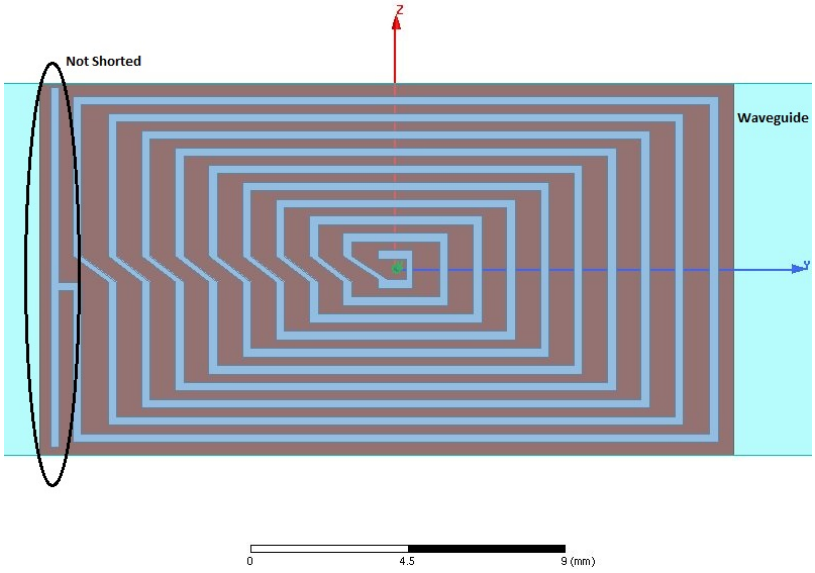

Figure 4.23: Single sided spiral structure whose vertical trace is not shorted

plate waveguide. Resonance is observed at 0.28, 0.6 and 0.86 GHz. From the graph

of S-parameters plotted over a range of frequencies, a negative permeability can be predicted to occur at lowest resonant frequency (0.28 GHz).

From the magnitudes and phases of S(1,1) and S(1,2) obtained from simulation, μ_r and ϵ_r response was extracted. Fig.4.25 shows the structure exhibiting negative permeability of -1.926 at 0.28 GHz. This version of the spiral resonator does not exhibit negative permittivity throughout the simulated frequency sweep.

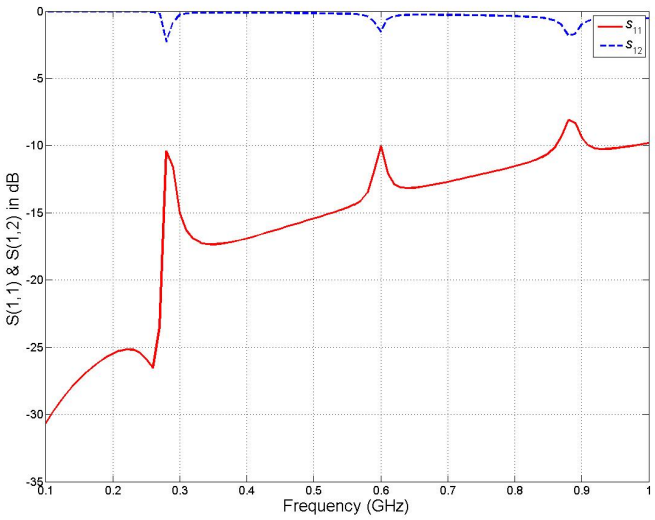

Figure 4.24: Simulation results of S parameters of spiral resonator from Fig.4.23

Thus, the combination of a spiral geometry and a vertical trace can be modified in different ways to control the resonance in the structure and thereby tune the permittivity and permeability response exhibited by the unit cell

From the proposed variations of the spiral geometry, one design will be used to replace the traditional dielectric employed in the design of a patch antenna. The design used in Section 4.3.1 is chosen to be incorporated into the patch antenna design. The intention behind this decision is because the vertical trace will not short the metal patch and the ground plane and thus preserve the patch antenna topology.

The unit cell described in Fig.4.13 is further modified to obtain resonance at around 200MHz. This metamaterial unit cell is designed and modified to be incorporated in a

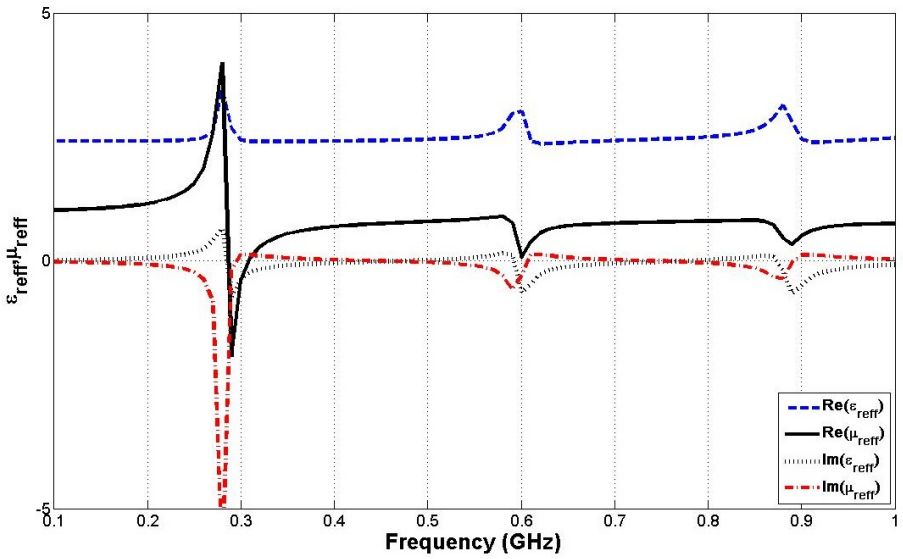

Figure 4.25: Extracted graph of ϵ and μ v/s frequency for spiral structure shown in Fig.4.23

phased array patch antenna that will be discussed in the next chapter. The dimensions of the new metamaterial cell structure are increased to $21.5mm \times 11.75mm$. By increasing the dimensions of the structure by almost 1 mm in each direction, we can obtain resonance at approximately 200 MHz. The gap between two rings lengthwise is 0.8mm while the gap along the width remains the same at 0.25mm. The trace width of the rings and the vertical trace is 0.25mm. The spiral section of the structure comprises ten concentric rings. Fig.4.26 shows a model of the spiral structure designed in HFSS.

Fig.4.27 shows the graph of S(1,1) and S(1,2) versus indicating resonance occurring at 210, 480, 720 and 970 MHz. Extracting μ and ϵ exhibited by this spiral structure, it is observed that a value of effective permeability $\mu_{eff} = -9.8$ is obtained at 210 MHz. The structure also exhibits a positive permittivity with its peak value being $\epsilon_{eff} = 27.8$ at 210 MHz.

The proposed metamaterial cells will be used as substrates in the patch antennas proposed in the next chapter. The influence of negative permittivity and permeability on the behavior of patch antennas will be studied. The metamaterials that have been

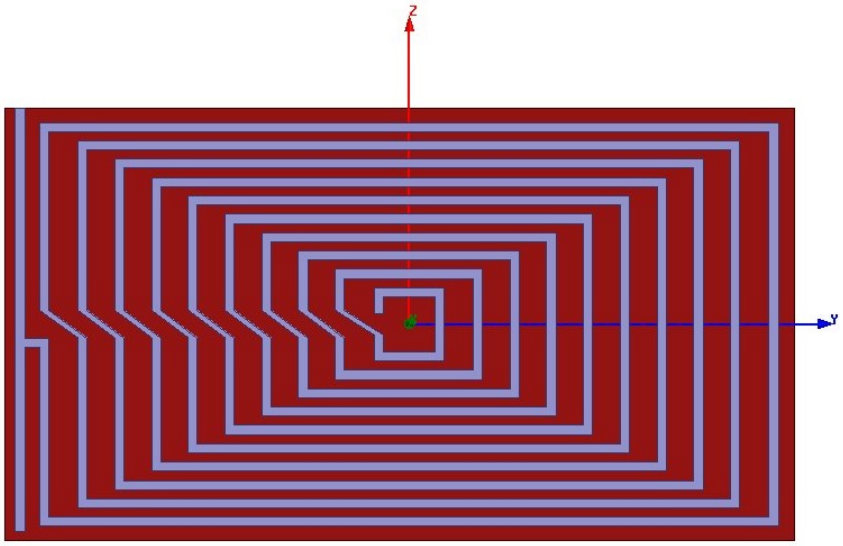

Figure 4.26: Single sided spiral resonator having lowest resonance at 210 MHz.

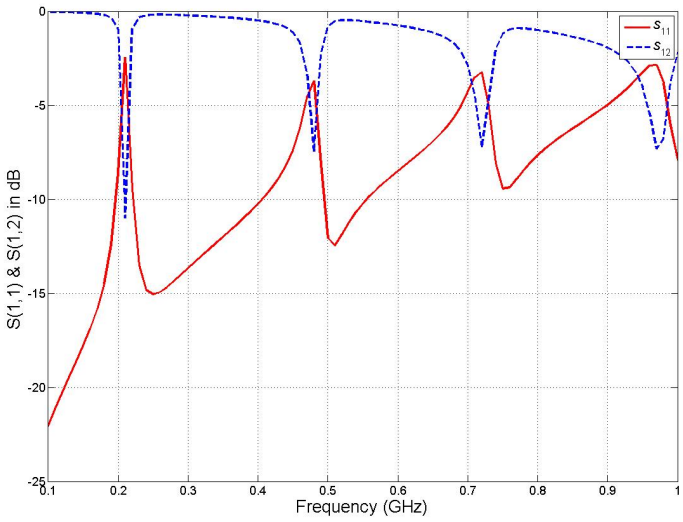

Figure 4.27: Simulation results of S parameters of spiral resonator from Fig.4.26

designed are tuned to have resonant frequencies to correspond with the subwavelength frequency of the patch antenna that will be proposed. The metamaterial cells are designed on a dielectric substrate in order to support the patch above it. The lowest resonant frequency of the metamaterial structures designed in this chapter lie below 300 MHz (to correspond with subwavelength frequencies of the antenna models).

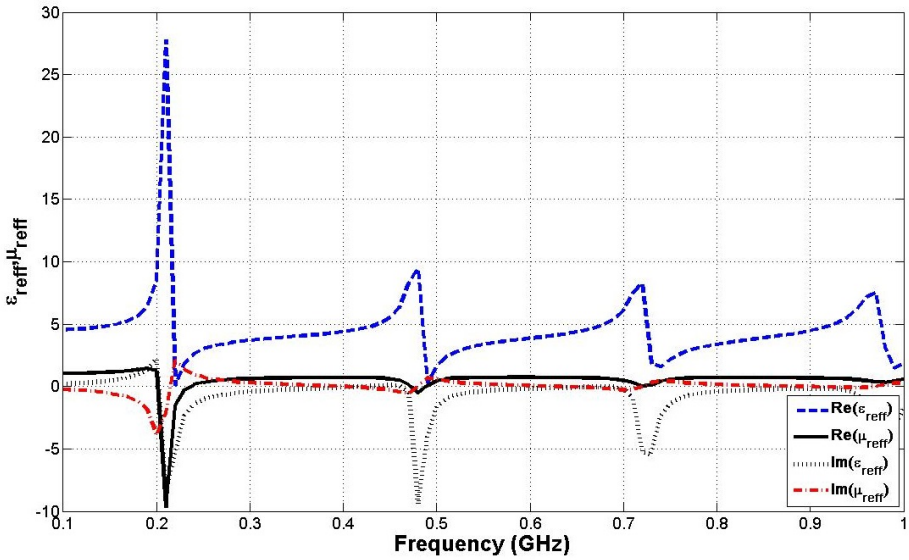

Figure 4.28: Extracted graph of ϵ and μ v/s frequency for spiral structure shown in Fig.4.26

CHAPTER 5: PATCH ANTENNAS LOADED WITH METAMATERIAL

Development and increasing demand for mobile communication, handheld devices, wearables such as smart phones, tablets, laptops, smart watches, WiFi routers has initiated an interest in novel techniques for minimizing the size of antennas embedded into these wireless devices. Resonating antenna structures such as the microstrip patch antenna typically have dimensions on the order of half a wavelength (in free space). As such, antennas required to operate at lower frequencies tend to be considerably larger in size. This calls for an investigation on different techniques that can be applied to the existing antenna topologies that can in return achieve miniaturization of their dimensions.

As we know, microstrip antennas have gained popularity in wireless communication due to its low profile planar and robust structure. The patch antenna is known to exhibit modest gain and directivity, among other radiation characteristics. Many modifications have been proposed to the patch antenna topology to reduce the dimensions of the antenna without compromising its gain and efficiency. The most common modification of the microstrip patch antenna is in the form of a Planar Inverted F Antenna (PIFA) whose dimensions are approximately on the order of $\lambda/4$ [10], which has found extensive use, especially in cellular phones. Metamaterials have also been incorporated into the patch antenna architecture to achieve miniaturization [5] [17] [20].

This chapter involves the use of metamaterial unit cells which are incorporated into the substrate for the patch antenna design. Different metamaterial cells have been placed in the empty space between the patch and the ground plane. Multiple metamaterial cells have been placed in different locations beneath the patch to observe the effects of negative permittivity and permeability on the fields in the cavity of the

patch. The patch antenna configurations proposed in the sections that follow, have been fed with a coaxial cable (probe feed).

5.1 Patch Antenna Loaded with Split Ring Resonator Metamaterial

The first proposed antenna model uses a metamaterial cell from Section 4.2. The dielectric substrate over which a patch antenna is designed is replaced with two split ring resonators. As shown in Fig.5.1 the space between the patch and the ground is filled with a substrate which is made up of a combination of air, which is an isotropic material, and split ring metamaterial cells exhibiting negative permeability. The split ring resonators are placed under one of the radiating slots of the patch to influence the fringing fields which in turn will give rise to a subwavelength resonant frequency corresponding with the resonant frequency of the split rings. The patch is probe fed with a coaxial cable, whose outer conductor is connected to the ground plane and the inner conductor is connected to the patch. A detailed description of the design and performance analysis of the antenna model is given below.

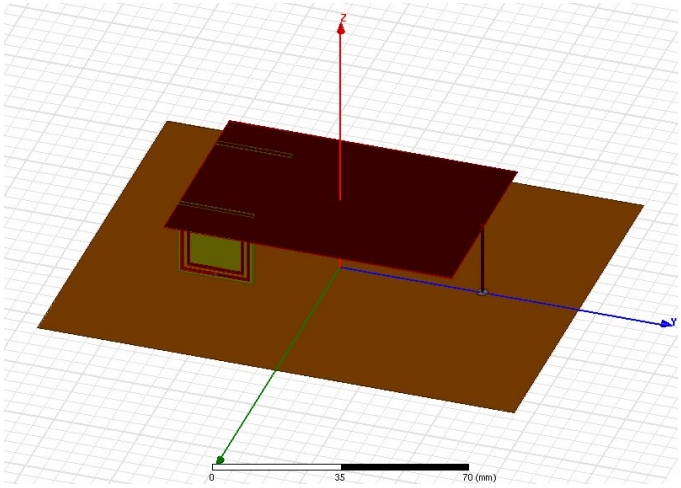

Figure 5.1: Model of Patch Antenna loaded with split ring resonators

5.1.1 Design and Simulation

Two split ring resonator cells are sandwiched between a metal patch and the ground plane as shown in Fig.5.1. Thus, the space between the patch and the ground is filled

with air and two metamaterial cells exhibiting negative permeability at 300MHz. This topology is modeled in HFSS and the dimensions of the patch are optimized to obtain resonance at 300MHz. This subwavelength resonance of 300MHz is obtained when the length of the patch L_p is 84mm and width W_p is 58mm. To ensure that adequate power is fed into the patch antenna, the coaxial cable is connected 0.7mm away from one of the radiating slots of the patch. The location of the split rings also influence the fields in the cavity of the patch antenna and as a result affects the resonance of the patch. The split rings are placed 11mm from the longer sides of the patch as shown from the top view of the antenna model given in Fig.5.2. Ideally, the ground plane should extend infinitely from the radiating surface of the antenna. However, to make the antenna model practical, the ground plane is truncated such that it extends from the patch up to a distance of 2.5 times the height of the metamaterial.

The presence of negative permeability along with positive permittivity at 300MHz influences the fields in the cavity of the patch, thus exciting a modified TM mode in the cavity. The resonant frequency of this dominant modified TM mode of the antenna corresponds with that of the split rings. This causes the patch to radiate at 300 MHz even though the dimensions of the patch are very small to support this

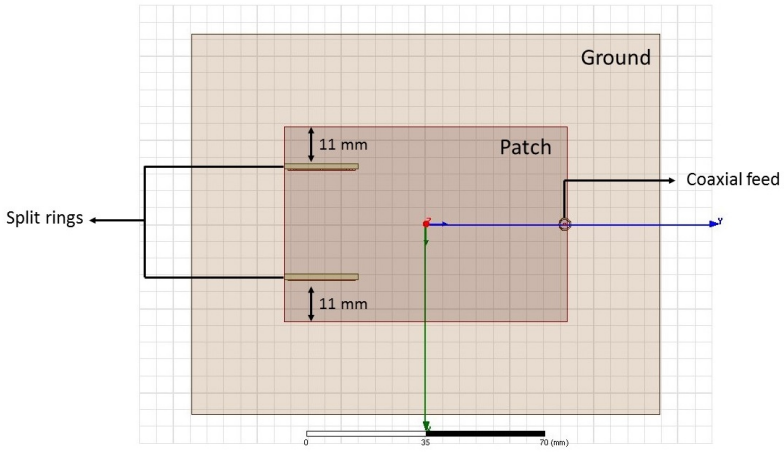

Figure 5.2: Top view of patch antenna model

subwavelength resonant frequency. The antenna model is simulated in HFSS and S-paramaters and far-field radiation results are obtained. It is observed from Fig.5.3 that at 300MHz, the antenna has a return loss of -11.6dB. From this figure, it can also be seen that the antenna exhibits resonance at 1.3GHz, which approximately corresponds with the actual dimensions of the patch. The antenna operates at dual frequencies wherein it is narrowband around 300MHz and considerably wider band at the second resonant frequency i.e 1.3GHz. To investigate the operation of the patch

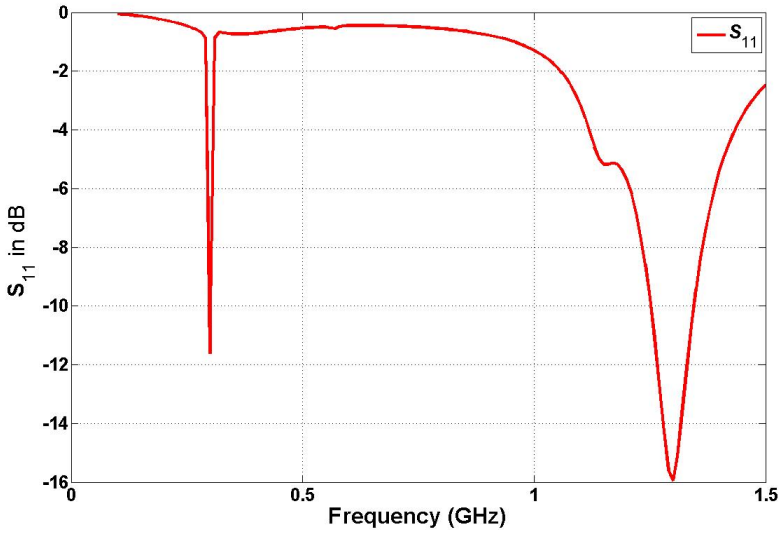

Figure 5.3: Return Loss of simulated antenna design

antenna at the subwavelength frequency of 300MHz, electric fields in the cavity of the patch are studied. The E fields that exist under the patch are plotted in HFSS to determine the transverse magnetic mode which causes the patch to radiate as shown in Fig.5.4(a). The E fields plotted under the radiating slot appear to be a modified combination of TM_{010} and TM_{020} modes. The magnitude of E field is maximum at the location of the two split rings and minimum at the edges and the center. Observing the E fields plotted along the nonradiating slot of the patch antenna shown in Fig.5.4 (b), we observe that the E fields change direction rapidly at the end of the slot where split rings are placed. These modified E fields produce fringing fields where the patch

is terminated. This causes the patch to radiate at 300 MHz.

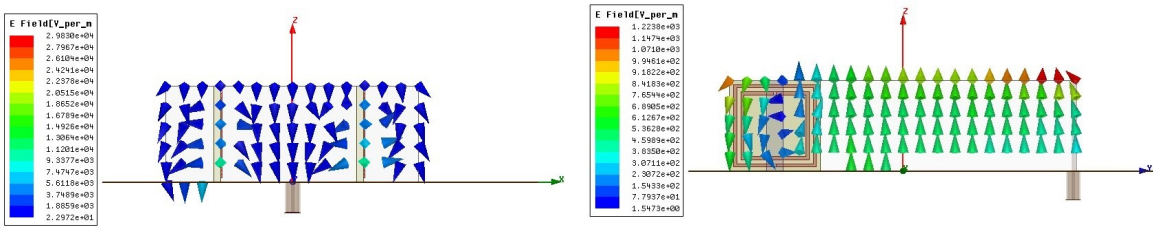

(a) Fields plotted along the width (b) Fields plotted along the length

Figure 5.4: Fields in the cavity under the patch plotted at 300 MHz

Similarly, at the second resonant frequency (1.3GHz) E fields are plotted in the cavity under the radiating and nonradiating slot of the patch antenna. Fig.5.5 (a) shows the E fields plotted along the width of the patch. To do so a non-model rectangular sheet was placed at the end of the patch where the split rings were placed. The fields plotted on this sheet resemble that of a TM_{020} mode. However,the pattern of the E field at this slot appears a little modified as compared to a normal TM_{020} mode of propagation. The second non-model sheet was placed along the length of the patch between the ground plane and the patch. The E fields on this sheet were uniform except in the area near the split rings. Hence, the second resonant frequency 1.3 GHz can be attributed to the modified TM_{020} mode.

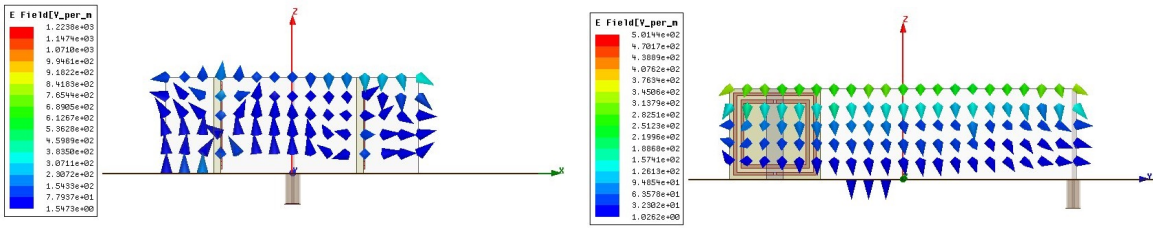

(a) Fields plotted along the width (b) Fields plotted along the length

Figure 5.5: Fields in the cavity under the patch plotted at 1300 MHz

The resulting antenna model is electrically small at 300MHz and hence its input impedance will be poorly matched which is evident from the plot shown in Fig.5.6.The input impedance of the proposed antenna at 300 MHz is 69.65-27.1132jΩ and The

input impedance at the secondary frequency 1.3 GHz is 41.44+10.99j. Ideally, the input impedance of the antenna has to be resistive at resonance frequency. But the proposed antenna shows finite non-zero reactance, in the input impedance of the patch antenna at the resonant frequencies.

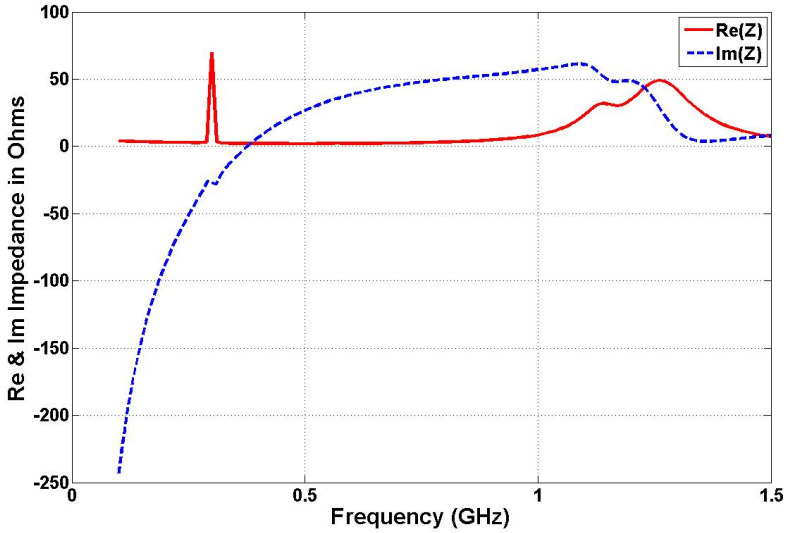

Figure 5.6: Input Impedance of simulated antenna design

Fig.5.7 shows the radiation pattern of the patch antenna described above. It can be observed from the figure that the antenna radiates away from broadside contrary to a conventional patch antenna which radiates primarily perpendicular to the plane of the antenna. The negative permeability exhibited by the split ring resonators forces radiation away from the metamaterial cells (i.e in the negative Y direction). Some amount of radiation is also observed near the horizon of the antenna. Fig.5.7 (a) describes the 3D polar plot of the far field radiations which shows that the maximum radiation occurs almost 90° from the Z axis. Fig.5.7 (b) represents the 2D polar plot of radiation pattern in the principal E and H plane plotted at ϕ=0° and 90° with theta ranging from 0° to 360°. As we know, gain of an antenna is related to its effective area and therefore the maximum gain is observed to be −12.7dB since the patch is electrically small.

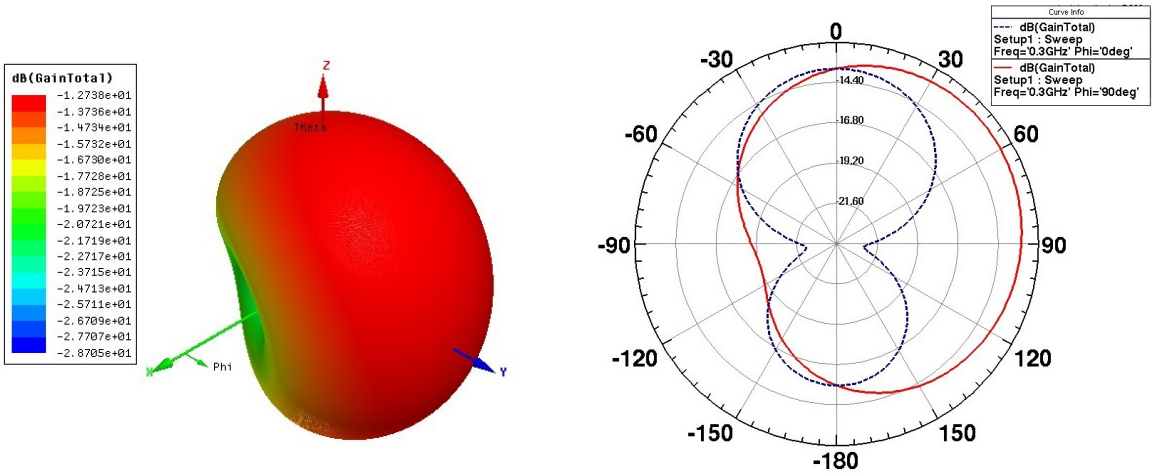

(a) 3D polar plot at 300 MHz (b) E and H plane 2D radiation pattern

Figure 5.7: Far field radiation pattern of the antenna at 300 MHz

The far field radiation pattern of the antenna at 1.34 GHz is shown in Fig.5.8. At this frequency, the antenna radiates normally at broadside (positive Z direction). The maximum gain at this frequency is observed to be 4.6dB, which is decent for a microstrip patch antenna.

As we know, the location of the split rings under the patch plays an important role

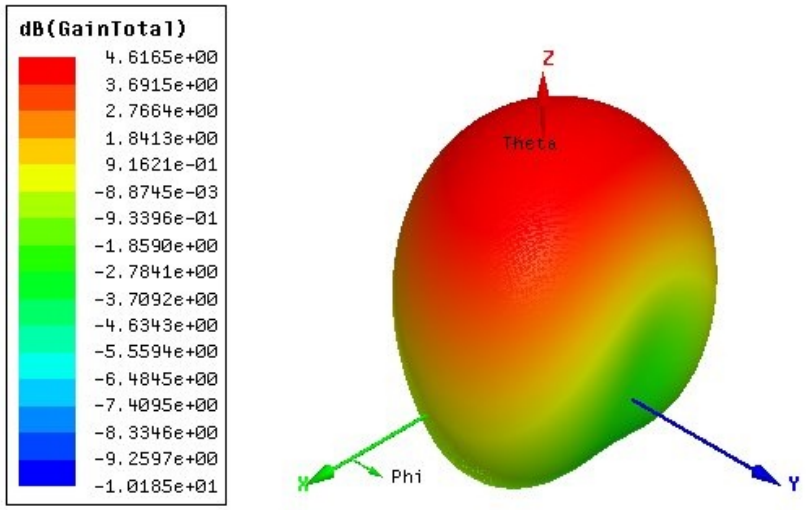

Figure 5.8: 3D polar plot of far field radiations at 1.3 GHz

in achieving subwavelength frequency of the patch. The split rings are now moved to

a distance of 17.35mm away from the lengths of the patch. Increasing the width to 60mm and moving feed point 10mm away the other free end of the patch, we obtain resonance at 300MHz. This model is shown in Fig.5.9.

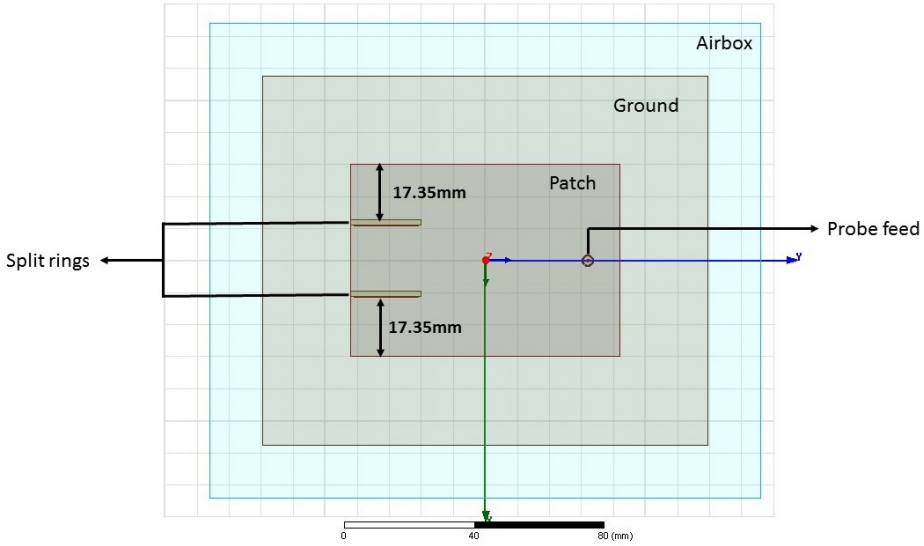

Figure 5.9: Top view of patch antenna when distance between split rings is decreased

As in the previous design, a second resonant frequency is observed at 1.25 GHz. The return loss of the antenna is given in Fig.5.10, which shows that the antenna structure has a return loss of -21.6dB at 300MHz and -13.55dB at 1.25 GHz. Similar to the previous design the antenna is extremely narrow band at 300MHz and broadband at 1.25GHz.

Fig.5.11 shows the input impedance of the antenna as a function of frequency. The input impedance of the antenna at 300 MHz is 44.65-3.88jΩ. The reactance of the impedance of the antenna is seen to have improved with these modifications in the antenna structure. It can also be seen that at 1.25 GHz, the input impedance is observed to be 38.84+14.43jΩ.

The far field radiation patterns of the simulated antenna structure are given in Fig.5.12. The figure shows 3D polar plots of radiation in terms of gain of the antenna. The radiation patterns are observed to be similar to the previous design. At

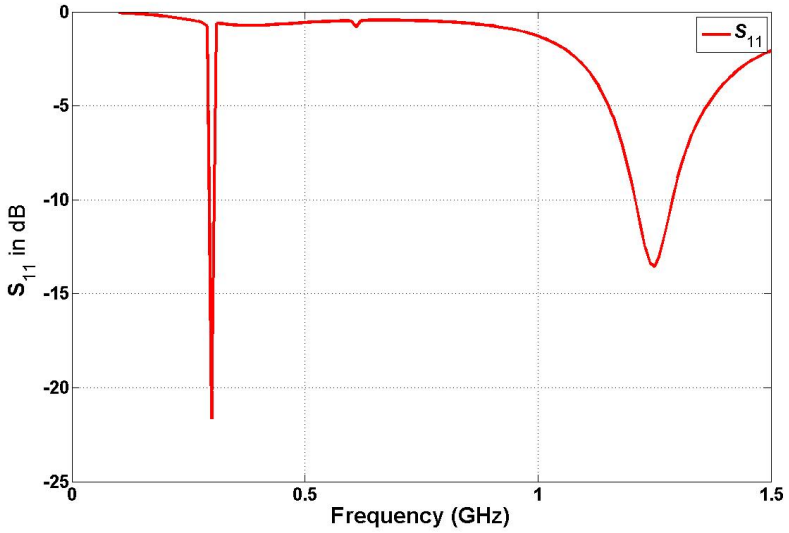

Figure 5.10: Return Loss of antenna structure shown in fig. 5.9

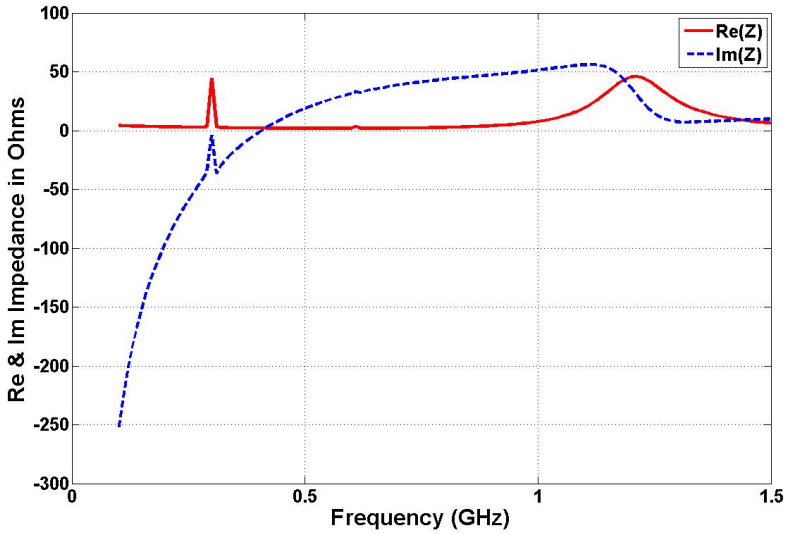

Figure 5.11: Input impedance of antenna structure shown in Fig.5.9

300MHz, the radiation pattern has been rotated by almost 90° from the Z direction and significant radiation occurs near the horizon. The maximum gain of this antenna design is also approximately −12dB since the effective area of radiation is electrically small. At 1.25GHz, the antenna radiates at broadside with a maximum gain of 3.75dB and the main beam appears much norrower.

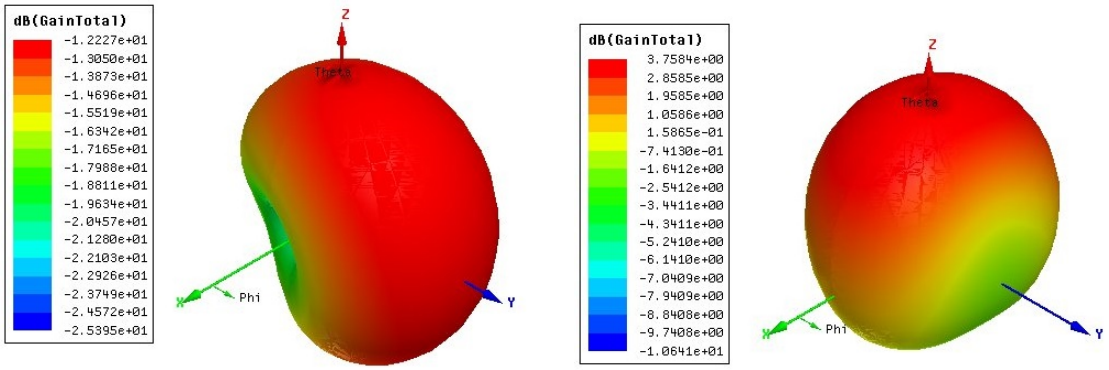

(a) 3D polar plot at 300 MHz (b) 3D polar plot at 1.25 GHz

Figure 5.12: Radiation pattern of antenna shown in Fig.5.9

Thus, we can observe that the resulting patch antenna structure that has been loaded with metamaterial cells has achieved dimensions on the order of approximately $\lambda_0/12 \times \lambda_0/19$. The resonance of the antenna is controlled by the MNG (Mu-negative) metamaterial cell used. The location of the metamaterial cells along with other factors such as dimensions of the patch and ground plane as well as the location of the feed, all contribute to the existence of this electrically small patch antenna model. Along with miniaturization, the antenna also achieves dual resonant frequencies; one frequency corresponding to the resonance frequency of the meta-structure and second related to the actual dimensions of the patch.

The next microstrip patch antenna is designed by replacing the split rings with the spiral structure described in Section 4.3.1. This spiral structure exhibits negative permittivity as well as permeability.

5.2 Patch Antenna Loaded With Spiral Resonator Metamaterial

The next antenna model proposed in this section consists of spiral metametarials described in Section 4.3.1 embedded into the patch antenna model. Two metamaterial cells shown in Fig.4.13 are placed between a metal patch and a ground plane. The metamaterial cells are placed such that the cavity under the patch mimic the rectangular waveguide in which the metmaterials have been simulated. The patch and the

ground behave as electric boundaries for the extraction of effective permittivity and permeability. To obtain negative permittivity response the vertical trace is shorted to the ground plane. Fig.5.13 provides a visual depiction of the proposed antenna structure. The location of the metamaterials, dimensions of the patch, ground plane, and location of the feed are optimized to ensure the patch resonates at the same frequency as the metamaterials.

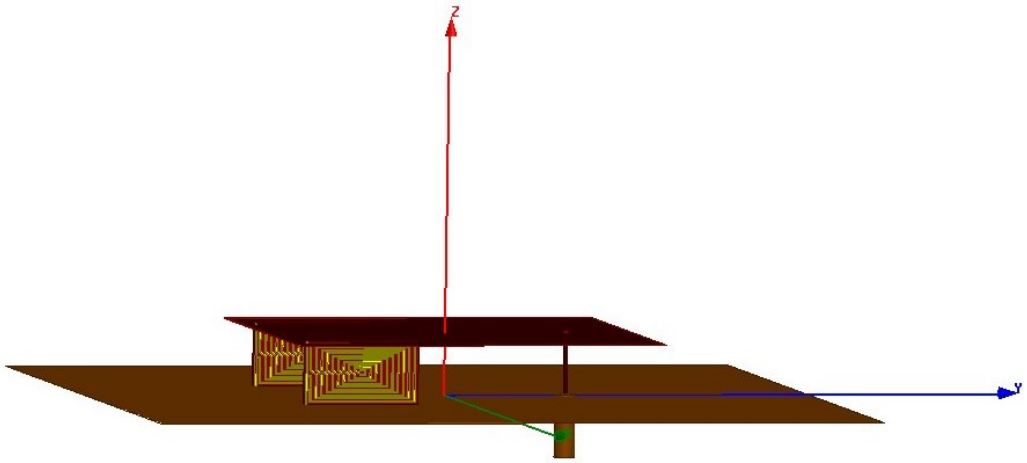

Figure 5.13: Antenna loaded with spiral metamaterial cells

5.2.1 Design and Simulation

Two spiral metamaterial cells described in Fig.4.13 are placed between a metal patch and a finite ground plane. The proposed antenna structure is 65mm long and 60mm wide and its ground plane is truncated at 112.5mm×117.5mm. As explained in in Fig.5.14, the two cells are placed at the two extreme ends of the patch under one of the radiating slots of the antenna. The edges of the cells were placed at a distance of 9.288mm from the longer edges and 3.05mm from the shorter edge of the patch, under which they are placed. The proposed antenna model is fed with a coaxial cable at a distance of 11.25mm from the second shorter edge of the metal patch. The distance between the ground and the patch is 10.85mm i.e the height of the metamaterial unit cell. The area between the patch and the ground is comprised of a combination of

spiral resonators and air, which act as a substrate for the proposed antenna structure. The model of the antenna is designed and simulated in HFSS to perform scattering and radiation analysis. In order to obtain far field radiation patterns, the antenna is placed in an airbox having dimensions 144mm×149mm×150mm. The antenna was excited using a waveport assigned to the free end of the coaxial cable. The antenna is simulated over frequencies ranging from 100MHz to 1GHz, similar to the simulation setup used for the metamaterial cells.

Fig.5.15 shows a simulated graph of return loss associated with the antenna when swept from 0.1 to 1 GHz. Observing the figure given below, we see the antenna achieves resonance at three frequencies i.e 0.26, 0.58 and 0.86 GHz. Note that these frequencies correspond to locations where the spiral metamaterial cells exhibit negative permittivity.

Input impedance of the simulated antenna is displayed Fig.5.16. All three resonances obtained can be referred to as subwavelength resonant frequencies, since they are not supported by the current dimensions of the patch. At 0.26 GHz, the antenna is somewhat poorly matched with its impedance equal to 46.03+j43.55 Ω. At the second

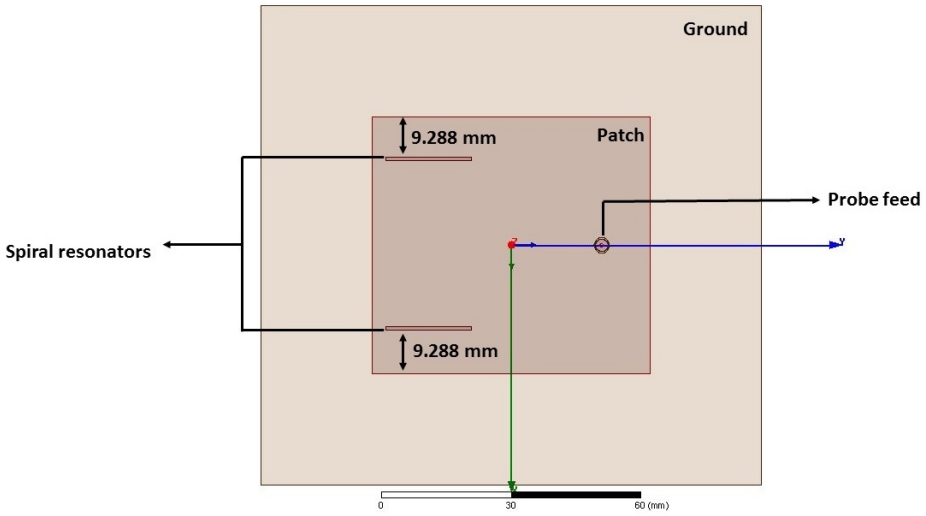

Figure 5.14: HFSS model of antenna with patch dimensions 65mm×60mm

resonant frequency of 0.58 GHz, the input impedance of the antenna is 49.9-j33.42Ω. And lastly, at 0.86 GHz, the input impedance is 33.36+j1.97Ω.

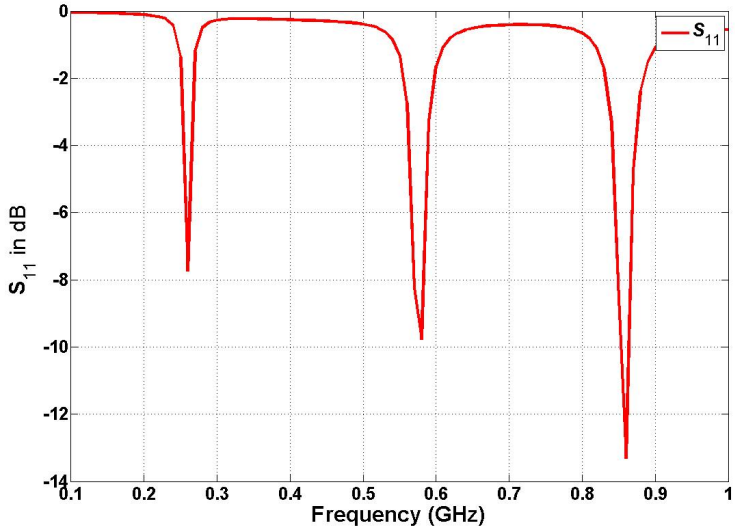

Figure 5.15: Return Loss (dB) of patch antenna shown in Fig.5.14

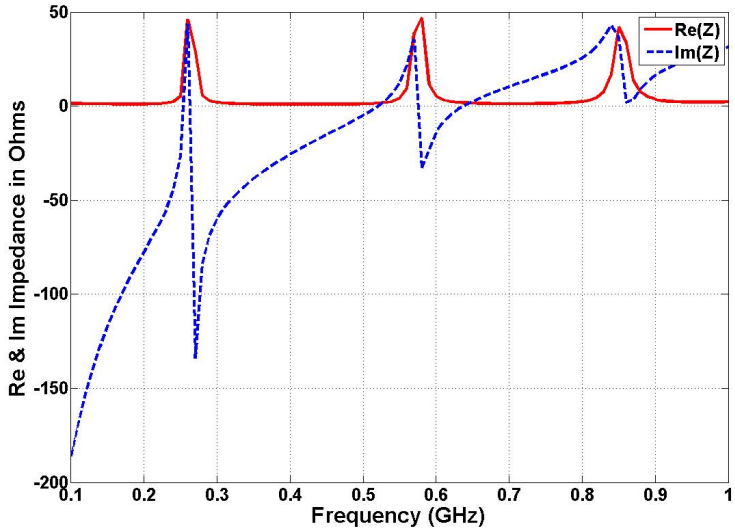

Figure 5.16: Input Impedance of patch antenna shown in Fig.5.14

To obtain the far field radiation pattern of the antenna, an infinite sphere is defined in HFSS where $0° \leq \phi \leq 360°$ and $0° \leq \theta \leq 180°$. A 3D polar plot describing the radiation pattern at the three resonant frequencies is shown in Fig.5.17. Fig.5.17 (a)

shows the radiation pattern at 0.26 GHz. The antenna at this frequency radiates off broadside, in fact it radiates along the plane of the antenna. The maximum radiation has deviated almost 90° from broadside. Since the antenna appears electrically small at this frequency, the gain and directivity are very small. At the second and third resonant frequencies, the antenna behaves more like a monopole with an omnidirectional radiation pattern. However, increased radiated power is observed at these frequencies. The gain of the antenna appears to improve as the resonant frequency increases. This behavior in antenna performance can be observed since the antenna appears to the electrically larger with increase in the resonant frequency.

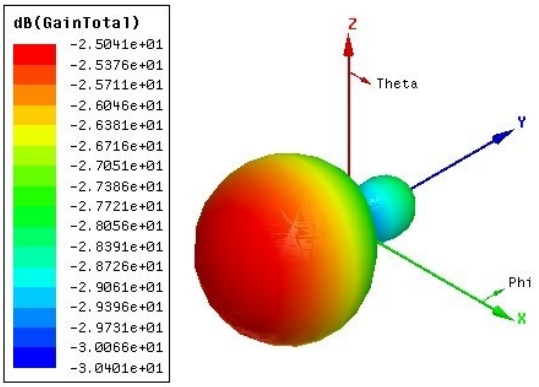

(a) 3D polar plot at 0.26 GHz

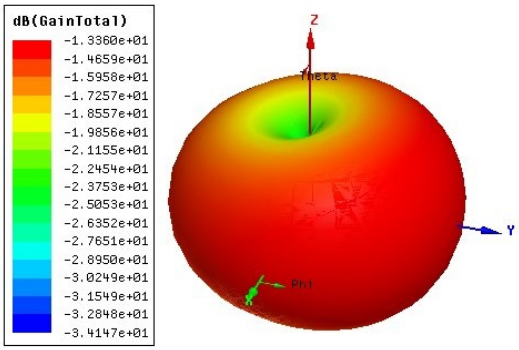

(b) 3D polar plot at 0.58 GHz

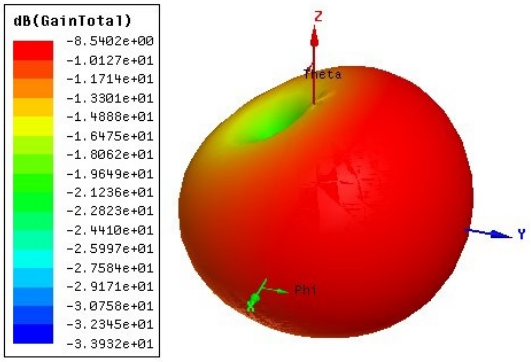

(c) 3D polar plot at 0.86 GHz

Figure 5.17: Far field radiation pattern of antenna(Fig.5.14) representing gain as a function of θ and ϕ obtained on simulation from HFSS

The performance of the antenna at the lowest subwavelength resonant frequency is closely analyzed. The antenna model shown in Fig.5.14 is now simulated with

an increased resolution from 240 MHz to 270 MHz with a step size of 1 MHz. The dimensions of the patch, location of the metamaterial cells and probe feed are the same as mentioned in the discussion above. We obtain the return loss and input impedance of the antenna shown in Fig.5.18. From Fig.5.18 (a), it can be observed the best return loss is approximately −10dB at 258MHz. The input impedance at this frequency is also obtained and is represented by Fig.5.18 (b). At 258 MHz, the input impedance obtained on simulation is 34.6+j22.13Ω.

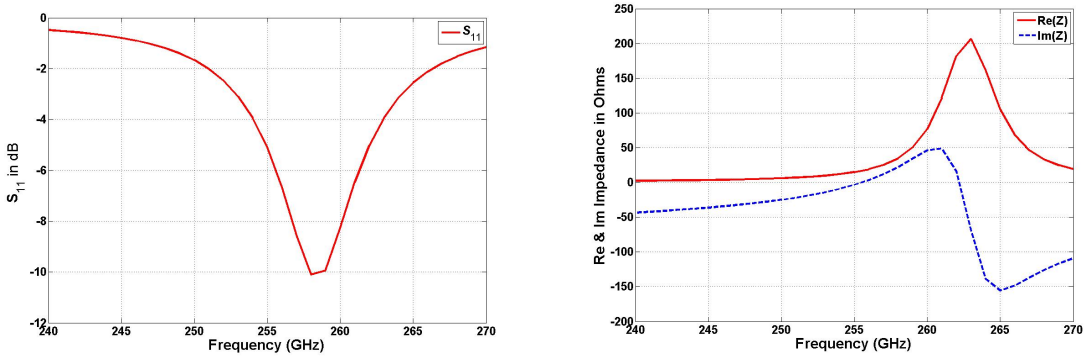

(a) Return loss in dB (b)Input impedance around 0.26 GHz

Figure 5.18: Simulation results of Fig.5.14 around 0.26 GHz with increased resolution

The radiation pattern of the antenna at 258 MHz is given by the 3D polar plot shown in Fig.5.19. Maximum radiation is directed away from from the vertical trace section of the spiral metamaterial cells in the negative Y direction. The main beam appears broader at 258MHz and the antenna radiates near the horizon of the antenna.

The dimensions of the copper rectangular patch are now increased such that the length and width are 75mm and 70mm respectively. The size of the ground plane is also increased to 138mm×133mm. The two spiral metamaterial cells are now placed 15.5mm from the two longer sides of the patch as shown in Fig.5.20. The antenna is fed using a coaxial cable at a distance of 13.75mm from the second radiating slot of the metal patch.

The antenna model was simulated in HFSS and the return loss and input impedance

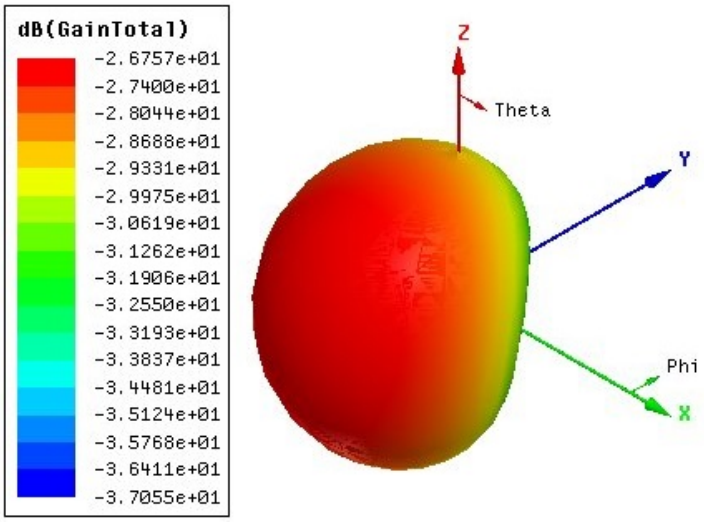

Figure 5.19: 3D polar plot of radiation at 258 MHz

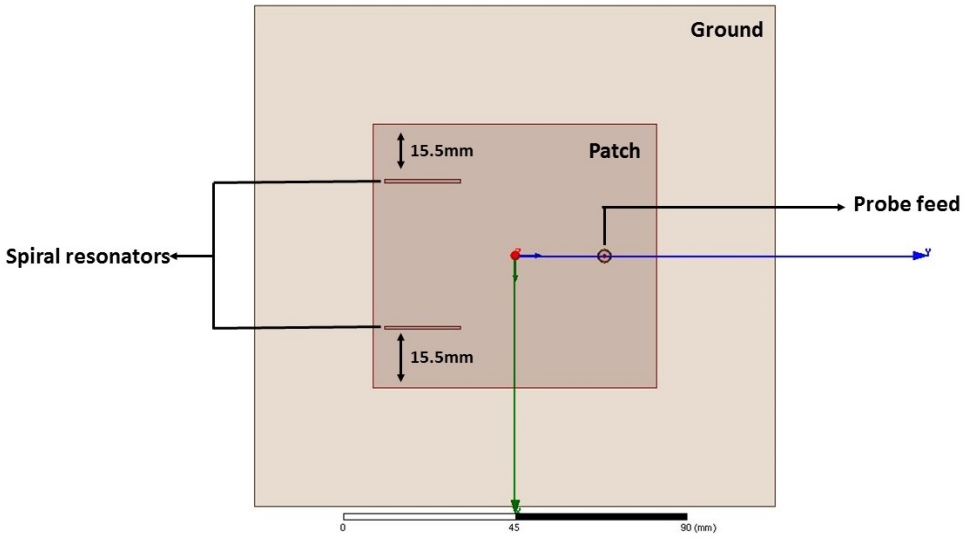

Figure 5.20: HFSS model of antenna with patch dimensions 75mm×70mm

of the antenna were obtained. Fig.5.21 (a) shows the plot of return loss which varies over a range of frequencies (0.1GHz to 1GHz) obtained from simulation. The graph shows three resonant frequencies at which the return loss is better than −10dB, i.e 0.26, 0.57 and 0.85 GHz. It can be observed that these three frequencies correspond with the frequencies at which the spiral resonator exhibits peak negative permittivity

values (refer Fig.4.17).

Input impedance of the antenna is shown in Fig.5.21 (b). The input impedance at all three resonant frequencies is poorly matched since the antenna is electrically small. Better impedance match may be obtained by optimizing the location of the feed point. The reactive component of the input impedance at 0.26GHz is the maximum in comparison to the other resonant frequencies.

Fig.5.22 shows the far field radiation of the patch antenna at the three resonant frequencies. Observing Fig.5.22 (a), we see that at 0.26 GHz, the main beam of the antenna is narrow. The main beam has deviated 90° from broadside in the negative Y direction, opposite to the location of the vertical trace section of the metamaterials placed beneath the patch. At the second and third resonant frequencies, we observe that the main beam is wide and directed in the positive Y direction as can be observed in the 3D polar plots shown in Fig.5.22 (b) and (c). Owing to its small radiation aperture size, the antenna exhibits low gain at the resonant frequencies, with the lowest gain exhibited at 0.26GHz.

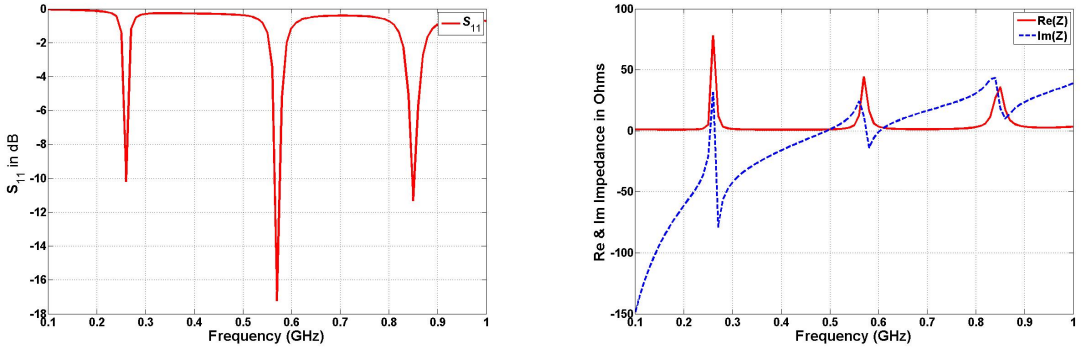

(a) Return loss (b) Input impedance

Figure 5.21: Simulation results of return loss and impedance of Fig.5.20.

The antenna characteristics at the lowest subwavelength frequency is observed more closely simulating the antenna model with more frequency points between 240 MHz and 260 MHz. The simulation results shown in Fig.5.23 (a), show the best return loss of −11.8dB obtained at 259 MHz. Coincidentally, it can be observed that the

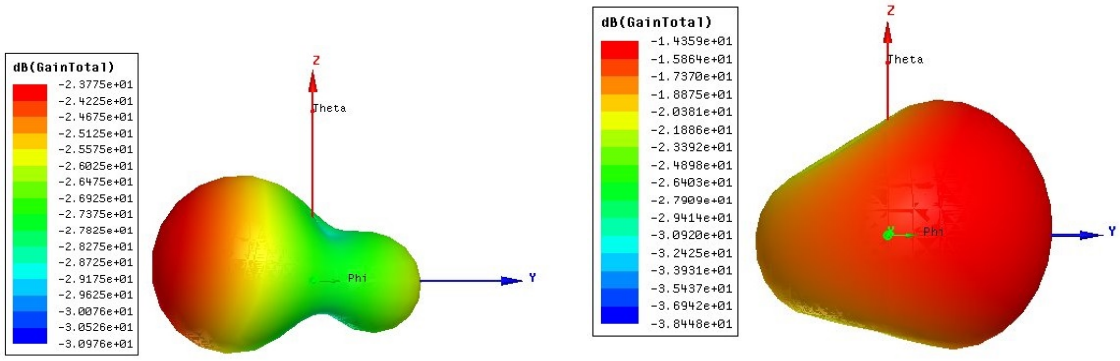

(a)3D polar plot of radiations at 260 MHz (b)3D polar plot of radiations at 570 MHz

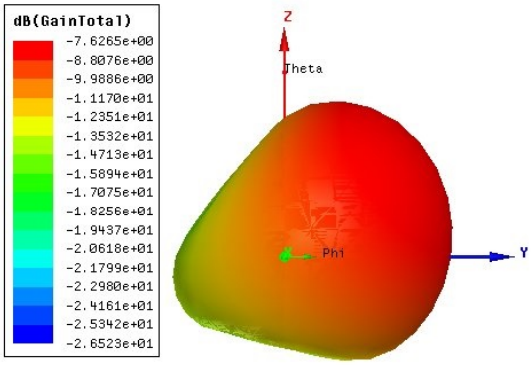

(c)3D polar plot of radiations at 850 MHz

Figure 5.22: Far field radiation pattern of patch antenna in Fig.5.20

metamaterial unit cell exhibits simultaneous negative values of permeability and permittivity at 259 MHz.

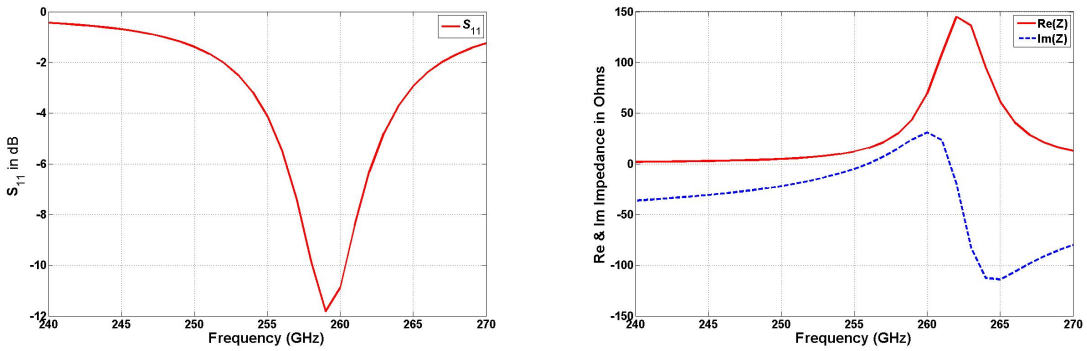

(a) Return loss in dB v/s frequency (b) Input impedance v/s frequency

Figure 5.23: Simulation results from HFSS at lowest subwavelength frequency (0.26GHz)

The radiation pattern of the antenna shown in Fig.5.20 at 259 MHz is shown in Fig.5.24. The radiation pattern of the antenna at 259 MHz is very similar to the 3D polar plot of the antenna at 260 MHz. It can be also noticed that the gain is lower by a small factor at 259MHz.

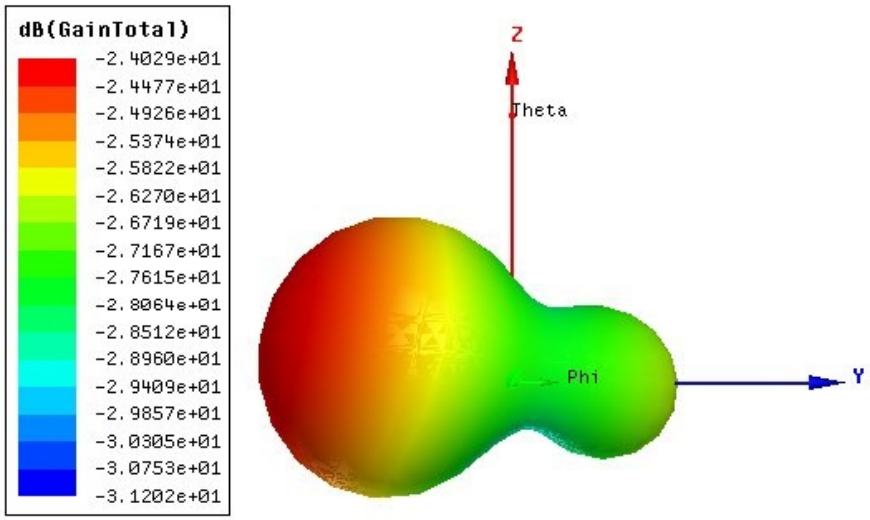

Figure 5.24: 3D polar plot of radiation at 259 MHz

The effect of spiral metamaterial cells when embedded into the patch antenna topology in the form of substrates is analyzed in the section so far. The dimensions of the patch, the location of the spiral structures beneath the patch greatly influence the resonance exhibited by the patch antenna. Loading patch antennas with metamaterials achieves miniaturization greater than the order of $\lambda_0/20$. Moreover, these proposed antenna models exhibit radiation near the horizon which is very difficult to achieve in a traditional patch antenna. Also, the patch antennas can be made to operate over dual or triple frequencies, by simply tuning the resonance of the metamaterial cells. These characteristics may be found useful in mobile handheld devices and wearables.

The concept discussed so far involving the notion of replacing a dielectric substrate by multiple metamaterial cells is next extended towards the development of an electrically small patch antenna array. The antenna array will be designed to operate at

200MHz and as such the spiral metamaterial unit cell is further modified to resonate at around this frequency. The patch antenna array is designed to achieve the goal of steering the main beam from broadside toward the plane of the antenna (horizon). The next section describes in detail, the construction of this phased array antenna from a single patch element, the modeling and simulation of the entire array in HFSS and demonstrate beam steering toward the horizon.

5.3 Electrically Small Phased Array Patch Antenna

An electrically small patch antenna array is designed on a ground plane that is half wavelength long at 200MHz (i.e. 750mm). A single square patch is placed on an FR-4 epoxy substrate that is one-eighth inch thick. The single element is then duplicated along X and Y axes to form a symmetric square array. A detailed description of the construction of a metamaterial embedded single element patch antenna and the construction of a phased array antenna is described in the sections that follow.

5.3.1 Description of a Single Element

An aperture coupled microstrip patch antenna was initially designed to operate at 200MHz. A copper ground plane of length 750mm is placed between two FR-4 epoxy dielectric slabs as shown in Fig.5.25 (a). The substrate above the ground plane is $\frac{1}{8}$" thick, whereas the dielectric slab below the ground is $\frac{1}{16}$". A square metal patch of length 50mm is printed on the top substrate and the microstrip transmission feed line is located on the bottom substrate, isolated from the radiating patch. To drive the energy from the feed line, a non resonant rectangular aperture is introduced in the ground plane.

Fig.5.25 (b) shows a close view of the single patch antenna element modeled in HFSS. The open circuit microstrip transmission feedline does not make a direct contact with the patch. A rectangular slot introduced in the ground plane, located under the patch, allows electromagnetic energy to travel through the dielectric substrate.

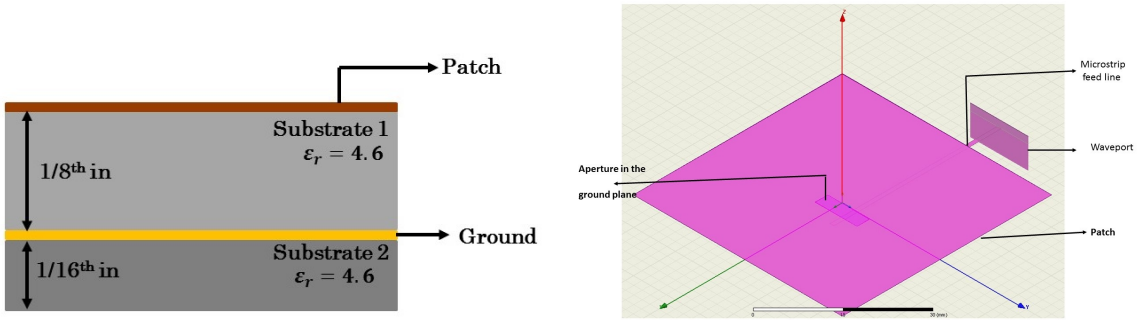

(a) Side view of a single patch (b) Close view of a single patch

Figure 5.25: Detailed description of a single patch antenna structure

The main idea behind this topology is that the energy from the transmission feedline is coupled through the bottom dielectric slab, passing through the aperture, into the top substrate. The bottom substrate is thinner in order to tightly couple the E-field absorbed from the microstrip line. This configuration is suitable for the construction of phased array antennas, which require the addition of an active feed network. The use of aperture coupling technique provides isolation of the feed network from the patch and hence less spurious radiation from the feed network affect the main radiation of the antenna. In order to simulate the antenna model and obtain its radiation characteristics, the whole structure is enclosed in an airbox assigned with radiation boundaries. The airbox is extended by a distance of $\lambda/4$ from all conducting surfaces of the ground plane. Fig.5.26 shows the HFSS model of a single element.

This antenna is designed to operate at 200 MHz. However, for the patch to effectively radiate at such low frequency, the dimensions of the patch has to be greater than designed. Moreover, the size of the aperture is too small to couple energy well at such low frequencies. The concept of using metamaterials that has been discussed in the previous sections of this chapter will be applied in order to decrease the size of the antenna and make it radiate efficiently. As per our previous discussion in Chapter 4, we will use a spiral resonator that has been designed to have its lowest resonant freqency closest to 200 MHz. Recalling, we have modified our spiral resonator con-

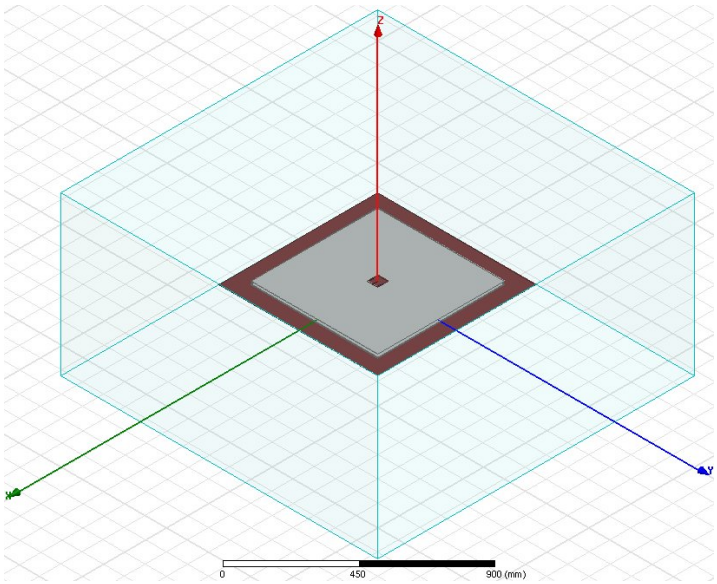

Figure 5.26: Single element of patch antenna array built in Ansys HFSS

sisting of partially polarized vertical trace, by extending the lengths and the widths of the rings to attain a resonant frequency lying in the vicinity of 200 MHz. This modified spiral shown in Fig.4.26 is loaded into the patch antenna structure which is described in great detail in the next section.

5.3.2 Metamaterial Embedded Single Patch Element

Instead of replacing the FR-4 epoxy dielectric slabs completely, spiral metamaterial unit cells are added to it as part of the substrate. The top substrate which is $\frac{1}{8}$ of an inch thick is made of two dielectric slabs having thickness $\frac{1}{16}$ of an inch. The two slabs are separated and two metamaterial cells are placed between them, such that they lie at the two extreme ends of the patch. Since the patch is assigned fixed dimensions, other parameters such as number and location of metmaterial cells beneath the patch and modification of the feed will have to be explored to ensure good antenna performance.

Three metamaterial cells have been sandwiched between the two halves of the top substrate as shown in Fig.5.27. The dielectric slabs and the metamaterial cells together behave as an inhomogeneous substrate for the single patch element. Two

metamaterial cells are placed at the extreme edges of patch, and one is placed in the center. In order for the spiral resonators to exhibit periodic negative permittivity, the structure has to be excited with E fields. Due to the absence of direct contact with an electric boundary, the vertical trace of the spiral resonator is shorted with the metal patch by drilling a hole through the top half of the thicker dielectric slab. The antenna is initially fed by an aperture coupled microstrip line. Introducing metamaterials into the substrate leads to some empty space filled with air between the dielectric slabs. The energy coupled from the microstrip feed line is lost due to the air gap between the two dielectric slabs. Therefore, the metal patch and the feed line are directly connected together by a copper wire to drive maximum energy into the antenna.

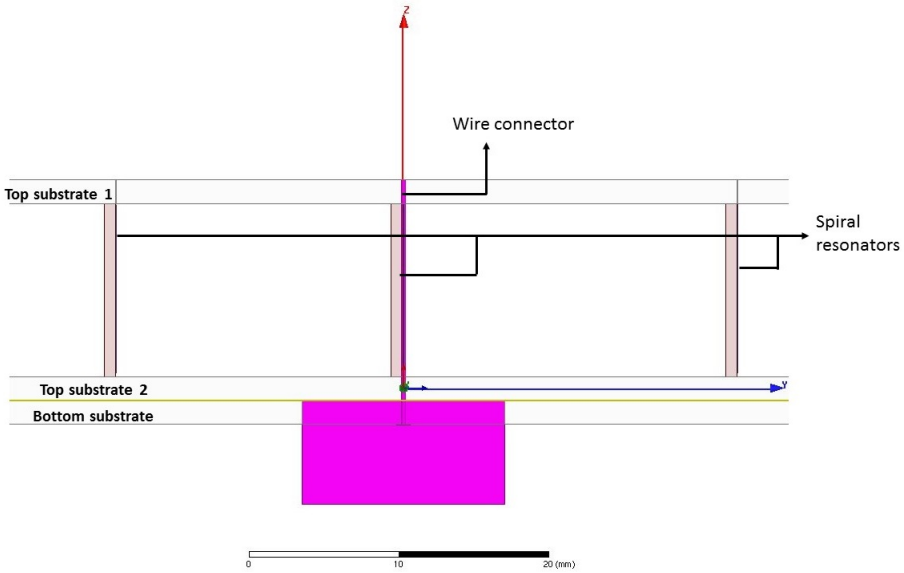

Figure 5.27: Side view of metamaterial loaded single patch element

This model of a single patch element is simulated at a single frequency of interest i.e. 200MHz. Upon simulation, the antenna is found to be very poorly matched with a very small resistive component of approximately 5Ω and a very high reactive component. This indicates that this antenna structure does not resonate at 200MHz and radiates very poorly. Also the main beam of radiation pattern of the antenna is observed to have deviated by almost 30° off broadside as shown in Fig.5.28. In

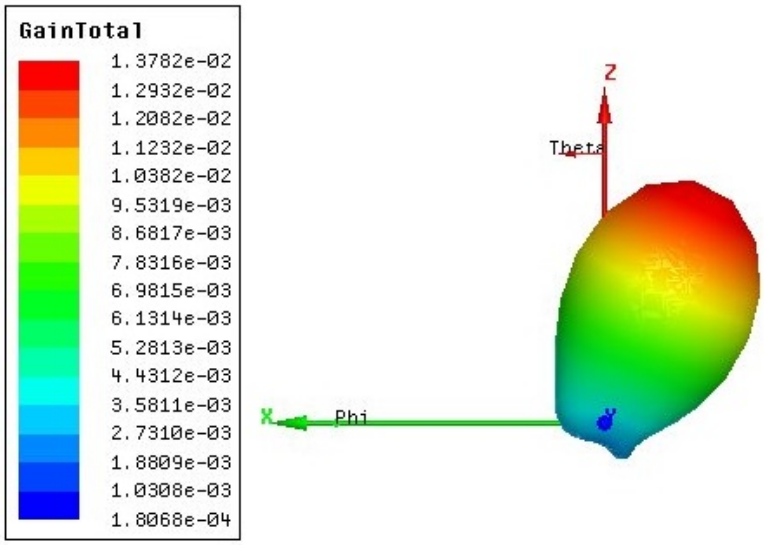

Figure 5.28: 3D polar plot of single element shown in Fig.5.27

order to improve the input impedance of the single element and shift the resonance of the antenna closer to the desired frequency of 200MHz, the spacing between the metamaterial cells is decreased by moving the unit cells at the extreme ends closer to the center as can be seen in Fig.5.29.

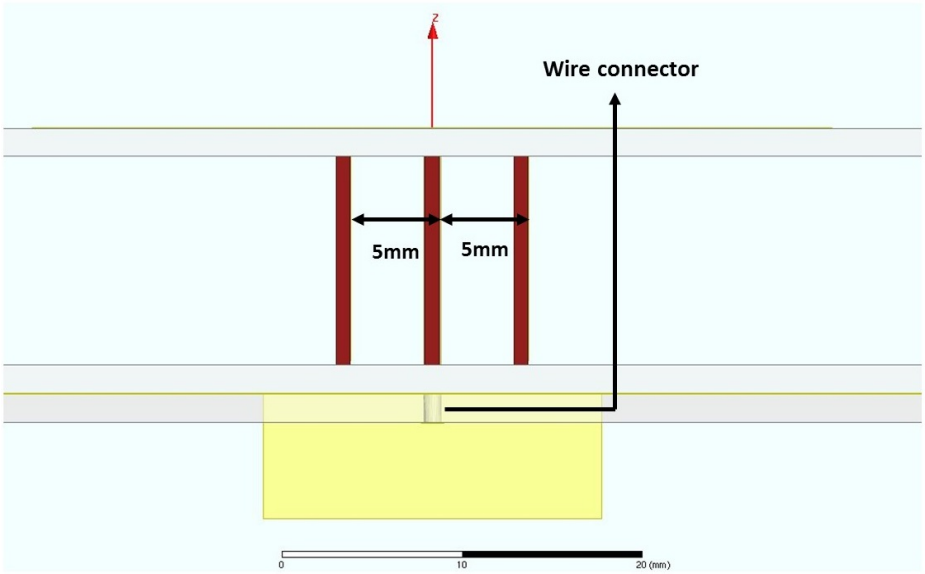

Figure 5.29: Single patch with distance between metamaterials decreased

The single patch element is simulated over a frequency range from 100 MHz to

500 MHz to observe the variation of input impedance of the antenna over frequency. Since the distance between the metamaterials has been reduced, the fields under the patch now vary rapidly due to the thinly spaced spiral structure. This increases the computation time taken by HFSS to simulate the antenna model. The plot of input impedance versus frequency is given in Fig.5.30. At 200MHz, the input impedance of the single element is 44.59+88.33j.

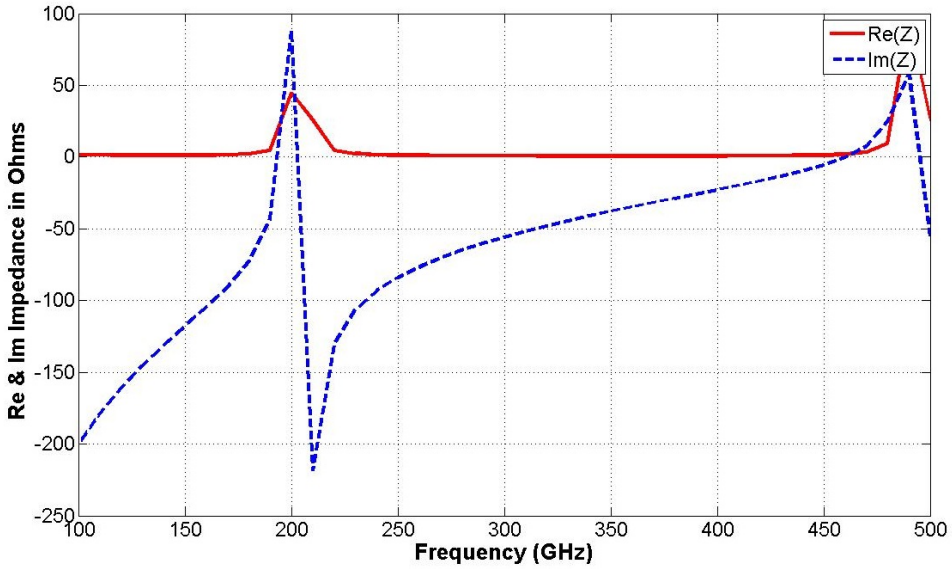

Figure 5.30: Input impedance of a single element

Having small effective radiation area, the single patch element radiates with a very small gain. In comparison with other patch antennas loaded with metamaterial cells that have been discussed previously, this proposed design provides an electrically small patch antenna which radiates with a comparatively higher gain. Moreover, this single patch element is also observed to radiate in the broadside similar to a traditional patch antenna. Fig.5.31 shows the radiation pattern of the antenna representing gain in dB (figure (a)) and linear scale (figure (b)). As you can see from Fig.5.31 (a), the maximum gain the single element achieves is -17dB.

Loading the single antenna element with metamaterial unit cells, results in a miniaturized patch of dimensions of the order of $\lambda_0/30 \times \lambda_0/30$. An electrically small phased

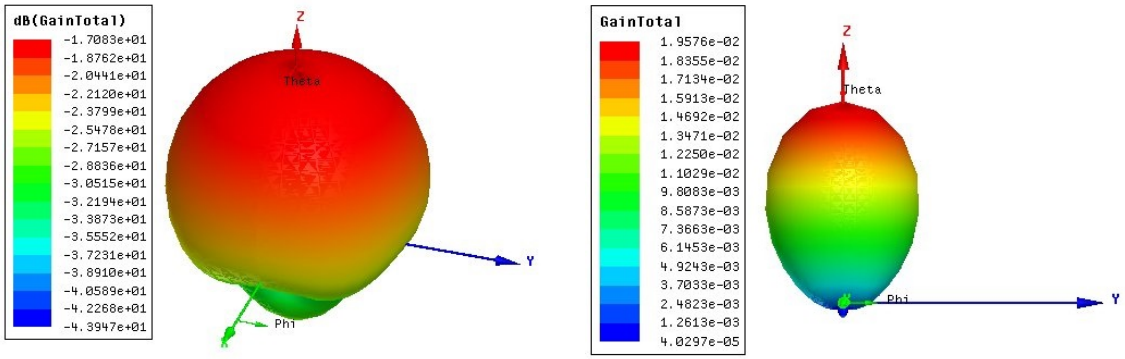

(a) Gain in dB (b) Gain in linear scale

Figure 5.31: 3D polar plot of radiation pattern at 200 MHz

array patch antenna is constructed from this single element. The planar antenna array proposed in the next section attempts to electrically steer its main beam from broadside toward the horizon.

5.3.3 Design and Simulation of Phased Array Patch Antenna

The electrically small single patch element is duplicated along the X and Y axis to form a planar array as can be seen in Fig.5.32a. An 8×8 element planar array is designed on a $\lambda/2$ ground plane (750mm) using HFSS. The center to center distance between two adjacent elements along the X and Y axis was $\lambda_0/20$ (i.e. 75mm). Fig.5.32b show the top view of the phased array patch antenna model, where 64 individual patches are placed in a symmetric arrangement of 8 rows and 8 columns. The 64 elements are placed on the top dielectric substrate of length 600mm and each individual element consists of three metamaterial unit cells placed beneath them.

The phased array electrically small antenna array is modeled and simulated in HFSS (high frequency structural simulator) which is an electromagnetic simulator which employs the finite element method to analyze electric and magnetic fields in the region of electromagnetic structure. The simulator divides the entire structure into many small tetrahedra, creating a geometric mesh. HFSS provides two types of initial mesh options, the TAU mesh and the classic mesh. The TAU mesh option

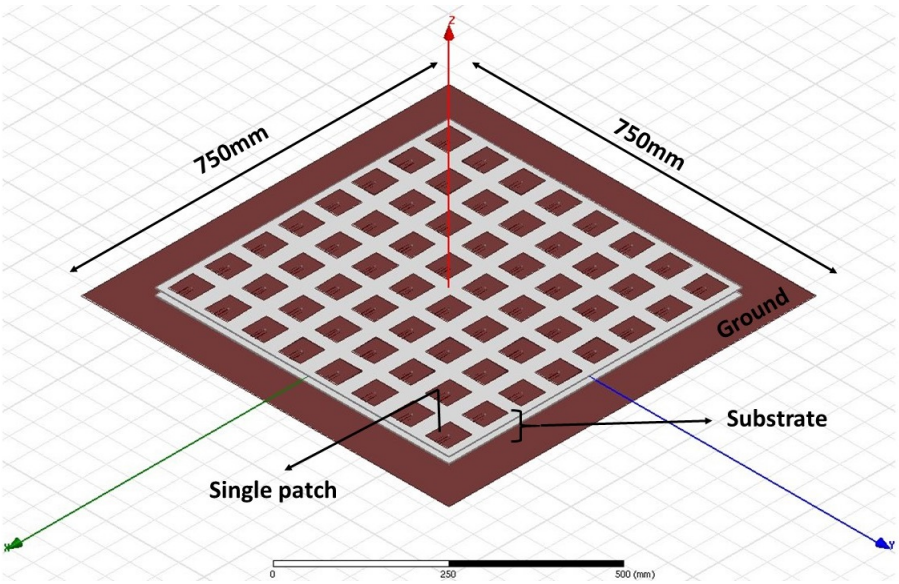

(a) HFSS model of phased array antenna

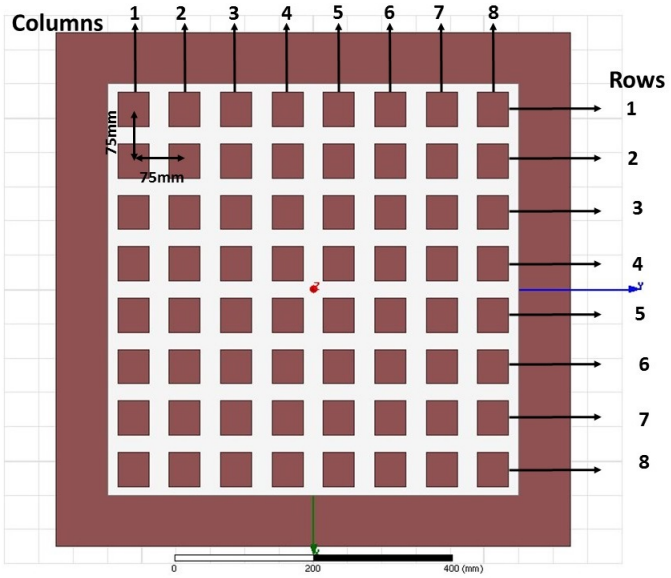

(b) Top View of phased array antenna

Figure 5.32: Planar phased array antenna consisting of 8×8 elements centered around the origin

creates a very tight mesh while coarser mesh can be obtained from the classic mesh option. Next, an electric mesh is created which consists of pre-processing option likes seeding and lambda refinement. Seeding influences the initial mesh formation and also reduces the number of adaptive passes. Lambda refinement ensures that the first adaptive mesh is refined to a fraction of a wavelength. HFSS solves electric fields in

each tetrahedra and stores the solution associated with it in a basis function; zero, first, second and mixed order basis function. Once the initial mesh is formed, HFSS calculated fields in each tetrahedra, using adaptive refinement. With each adaptive pass the accuracy of the solution improves and more tetrahedrons are added to the initial mesh. This increases the RAM utilization and the CPU computation time. HFSS continues solving the fields inside the closed structure until a specific convergence criteria ('delta-S') is met. Training manual provided by Ansys explains this computation and simulation process [12].

The patch antenna array embedded with spiral metamaterial unit cells is a complex structure and the fields in the cavity of the antenna vary rapidly. The initial mesh of the structure generated by HFSS contains more than seven million tetrahedrons. To reduce computation time and memory utilization, certain changes were made to the 'Initial Mesh Settings' which can be found under the 'Mesh Operation' settings. A classic mesh, which is coarser was chosen instead if the TAU mesh. Additional surface approximation settings were also applied where in the 'Maximum Surface Normal Deviation' angle was changed to 60°. The values of 'Maximum Surface Deviation' and 'Aspect Ratio' can also be changed to form a coarser mesh. The changes made to the 'Initial Mesh Settings' are summarized in Fig.5.33a.

Since the single patch element was simulated accurately with a tighter convergence criteria (delta-S=0.02), accurate results of input impedance was obtained. To enable convergence in the solution, the adaptive passes were increased to 30 and the delta-S value was changed to 0.03. Iterative solver was used to solve E and H fields instead of the direct solver, since the iterative solver is known to consume less RAM. Additionally, the maximum refinement per pass is reduced to 20% from the default 30%. The 'mixed order' basis function is used, which assigns basis function elements depending on the level of accuracy needed in different parts of the antenna model. These changes made to the solution setup are shown in Fig.5.33. Even though the

time consumed by the solver was high (approximately 20 hours), converged solutions were obtained without exceeding the available RAM limit. The patch antenna array was simulated at a single frequency of 200MHz.

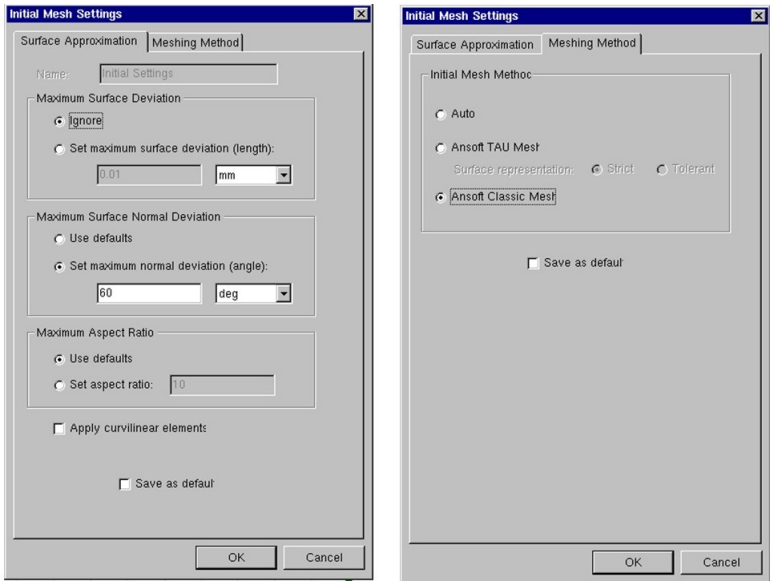

(a) Initial mesh settings

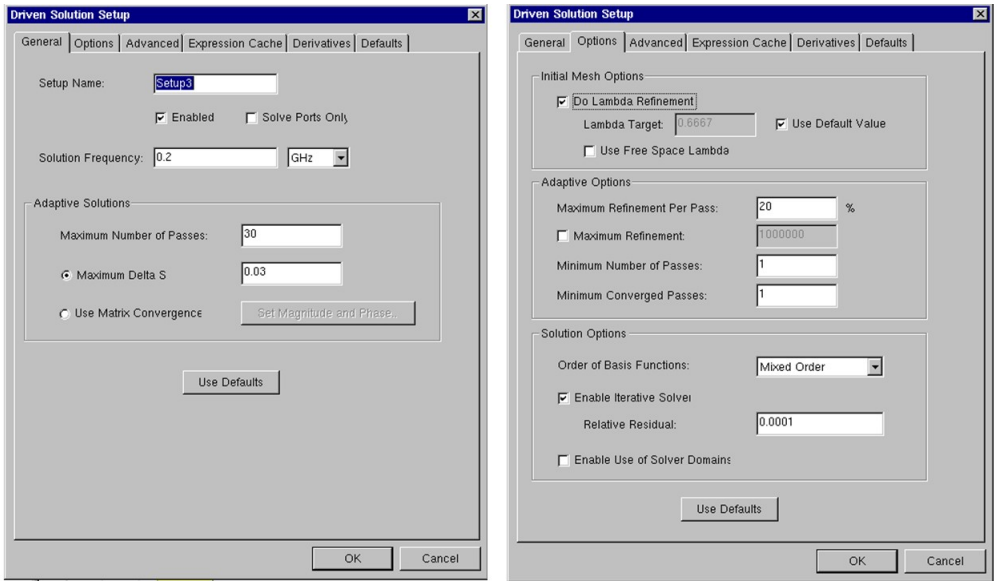

(b) Setup settings

Figure 5.33: HFSS settings to reduce RAM consumption

Upon simulation, an infinite sphere was defined to obtain far field radiation patterns in terms of gain and other parameters of the antenna. Fig.5.34 shows the 3D polar

plot of the radiation pattern of the antenna in terms of gain in dB. As can be seen from Fig.5.34a., the gain of the entire patch antenna array has seen a drastic increment by almost 10 dB and the maximum gain of the phased array patch antenna is observed to be -1.3dB, which is very high considering that the antenna array is electrically small. Even though a single patch is approximately $\lambda/30$ at 0.2 GHz, the entire antenna array structure is half wavelength long which also contributes to this increase in total gain of the antenna. Fig.5.34b. represents the radiation pattern of the antenna with its gain in linear scale.

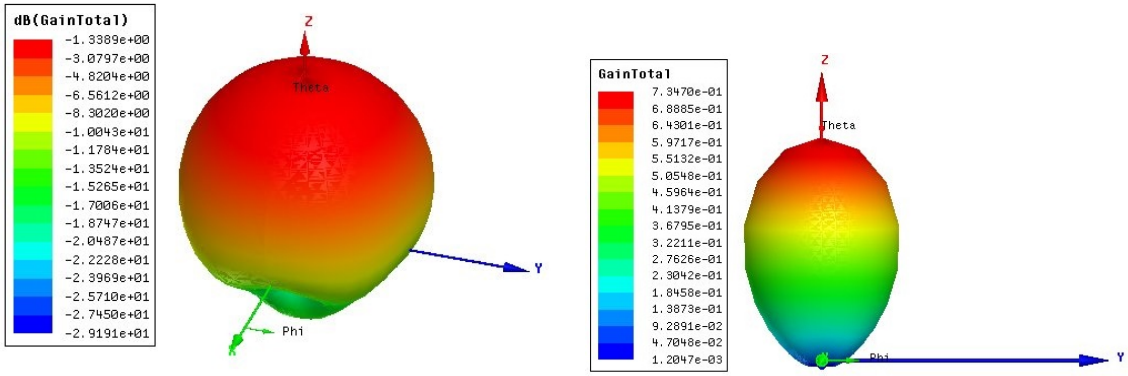

(a) Gain in dB (b) Gain in linear scale

Figure 5.34: 3D polar plot representing radiation pattern of 8×8 planar phased array patch antenna

To avoid grating lobes in the radiation pattern of a broadside array, the spacing between individual elements has to be less than $\lambda/2$. However, the spacing between neighboring elements in the proposed phased array antenna structure is $\lambda/20$, which may produce mutual coupling between patches. Keeping these dimensions in mind, an array factor of the antenna is designed, such that a side lobe level of -20dB is obtained.

5.3.3.1 Calculating Magnitudes of Array Factor

The array factor for elements placed along the X axis is calculated as given in equations below. Since the planar array consists of an even number of elements, the

array factor (AF_x) is computed as follows:

$$AF_x = \sum_{n=1}^{4} a_n \cos(2n-1)u_x \tag{5.1}$$

Expanding the array factor in the X direction, we get

$$\begin{aligned} AF_x &= a_1\cos(u_x) + a_2\cos(3u_x) + a_3\cos(5u_x) + a_4\cos(7u_x) \\ AF_x &= 64a_4\cos^7 u_x + [-112a_4 + 16a_3]\cos^5 u_x + [56a_4 - 20a_3 + 4a_2]\cos^3 u_x \\ &+[-7a_4 + 5a_3 - 3a_2 + a_1]\cos u_x \end{aligned} \tag{5.2}$$

To determine the coefficients a_n of the expanded array factor AF_x, Equation 5.2 is equated to the Tchebycheff polynomial of the order $N-1$.

The level of sidelobes in the radiation pattern have to be below -20dB. The array factor is equated to Tchebycheff polynomial $C_7(z_0)$. To find z_0, $C_7(z_0) = r_0$, and therefore $r_0 = 10^{\frac{SLL}{20}}$=10. Equating r_0 to Tchebycheff polynomial $C_7(z_0) = \cosh[7cosh^{-1}(z_0)]$, z_0 is calculated to be equal to 1.0928.

Next, $\cos(u_x)$ is replaced with z/z_0 in Equation 5.2. Since the planar array consists of rows of 8 elements, seventh order Tchebycheff polynomial is chosen to compute the coefficients a_n. The seventh order Tchebycheff polynomial is given by,

$$C_7(z) = 64z^7 - 112z^5 + 56z^3 - 7z \tag{5.3}$$

Comparing the coefficients of Equation 5.3 with the coefficients having same powers of $cos(u_x)$ in Equation 5.2, $a_1,\ a_2,\ a_3,\ a_4$ are calculated. The calculated coefficients and their normalized values are given in the Table 5.1. Similarly, the coefficients of array factor functions for elements placed along Y axis are calculated and tabulated in Table 5.2. The normalized coefficients given in Tables 5.1 and 5.2 are multiplied and the resulting values of coefficients given in Table 5.3 are provided to individual antenna elements to obtain sidelobe levels below -20dB. When coefficients were given as

inputs of the magnitude to the individual sources, the main beam appeared unaffected, which can be attributed to the $\lambda/20$ spacing between elements of the array.

Table 5.1: Coefficients of array factor along X axis

a_n	Calculated values	Normalized values
a_1	1.86116	1
a_2	2.11871	1.138381
a_3	2.8078	1.508629
a_4	3.20837	1.723855
a_5	3.20837	1.723855
a_6	2.8078	1.508629
a_7	2.11871	1.138381
a_8	1.86115	1

Table 5.2: Coefficients of array factor along Y axis

b_n	b_1	b_2	b_3	b_4	b_5	b_6	b_7	b_8
Calculated value	1.86116	2.11871	2.8078	3.20837	3.20837	2.8078	2.11871	1.86116
Normalized values	1	1.13838	1.5086	1.7238	1.7238	1.5086	1.1383	1

Table 5.3: Coefficients of array factor obtained on calculation

	b_1	b_2	b_3	b_4	b_5	b_6	b_7	b_8
a_1	1	1.138381	1.508629	1.723855	1.723855	1.508629	1.138381	1
a_2	1.138381	1.295912	1.717395	1.962405	1.962405	1.717395	1.295912	1.138381
a_3	1.508629	1.717395	2.275962	2.600658	2.600658	2.275962	1.717395	1.508629
a_4	1.723855	1.962405	2.600658	2.971676	2.971676	2.600658	1.962405	1.723855
a_5	1.723855	1.962405	2.600658	2.971676	2.971676	2.600658	1.962405	1.723855
a_6	1.508629	1.717395	2.275962	2.600658	2.600658	2.275962	1.717395	1.508629
a_7	1.138381	1.295912	1.717395	1.962405	1.962405	1.717395	1.295912	1.138381
a_8	1	1.138381	1.508629	1.723855	1.723855	1.508629	1.138381	1

5.3.3.2 Phases to Provide Progressive Phase Shift to the Main Beam

Individual patches when arranged in a linear or a planar array are capable of steering the main beam in a desired direction. This can be achieved by electrically

steering the main beam with the help of external phase shifter circuitry applied to the feeding section of the antenna. The input signal, after being amplified, is fed to each element with a phase shift. The angle by which the input signal is shifted is different for each patch and the tilt in the main beam from the Z axis can be associated with angles θ_0 and ϕ_0. Here, θ_0 is measured from the Z axis and ϕ_0 is measured from X axis in the X-Y plane. To calculate progressive phase shift that has to be provided to the elements of the phased array antenna, the following formulas are used, where β_x provides the angles for elements in the X axis and β_y provides angles for elements in the Y axis. Adding the two phases for the respective elements, an 8×8 matrix is obtained which provides the exact angle by which the input signal has to be phase shifted before feeding to the elements of the phased array patch antenna.

$$\begin{aligned} \beta_x &= \mp(n-1)kd_x \sin\theta_0 \cos\phi_0 \\ \beta_y &= \mp(n-1)kd_y \sin\theta_0 \sin\phi_0 \end{aligned} \tag{5.4}$$

d_x and d_y in Equation 5.4 are the center to center inter-element spacing in the X and Y direction respectively. To keep the level of grating lobes in the radiation to a minimum, the inter-element spacing has to be less than λ. Similarly, in order to avoid mutual coupling between neighboring elements, the inter element distance cannot be less than a quarter of a wavelength. The proposed design of the phased array patch antenna has an center to center distance between neighboring elements equal to $\lambda/20$, which may result in strong mutual coupling between the array elements.

The main beam of the antenna which radiates broadside is now steered away from the Z axis. To steer the main beam 30° off broadside, phases are calculated using relations of progressive phase shift angles β shown in Equation 5.4. When these angles were provided to each source in the 'Field Overlay' menu provided by HFSS it was observed that the main beam did not deflect from broadside. Hence, random values of angles were provided by trial and error method. The angle provided in the Tables 5.4

and 5.5 allowed the beam to be steered off broadside progressively at angles 30°, 45°, 60°, 70° and 80° from the Z axis. It is interesting to note that the main beam of the proposed antenna could be steered up to 80°, thus enabling radiation near the horizon.

Table 5.4: Phase shifts applied to individual elements of the phased array patch antenna

(a) To shift beam 30° from broadside

	b_1	b_2	b_3	b_4	b_5	b_6	b_7	b_8
a_1	180	180	180	180	180	180	180	180
a_2	90	90	90	90	90	90	90	90
a_3	45	45	45	45	45	45	45	45
a_4	0	0	0	0	0	0	0	0
a_5	0	0	0	0	0	0	0	0
a_6	−45	−45	−45	−45	−45	−45	−45	−45
a_7	−90	−90	−90	−90	−90	−90	−90	−90
a_8	−180	−180	−180	−180	−180	−180	−180	−180

(b) To shift beam 45° from broadside

	b_1	b_2	b_3	b_4	b_5	b_6	b_7	b_8
a_1	180	180	180	180	180	180	180	180
a_2	100	100	100	100	100	100	100	100
a_3	70	70	70	70	70	70	70	70
a_4	10	10	10	10	10	10	10	10
a_5	−10	−10	−10	−10	−10	−10	−10	−10
a_6	−70	−70	−70	−70	−70	−70	−70	−70
a_7	−100	−100	−100	−100	−100	−100	−100	−100
a_8	−180	−180	−180	−180	−180	−180	−180	−180

(c) To shift beam 60° from broadside

	b_1	b_2	b_3	b_4	b_5	b_6	b_7	b_8
a_1	180	180	180	180	180	180	180	180
a_2	100	100	100	100	100	100	100	100
a_3	90	90	90	90	90	90	90	90
a_4	10	10	10	10	10	10	10	10
a_5	−10	−10	−10	−10	−10	−10	−10	−10
a_6	−90	−90	−90	−90	−90	−90	−90	−90
a_7	−100	−100	−100	−100	−100	−100	-100	−100
a_8	−180	−180	−180	−180	−180	−180	−180	−180

Table 5.5: Contd. from Table 5.4

(a) To shift beam 70° from broadside

	b_1	b_2	b_3	b_4	b_5	b_6	b_7	b_8
a_1	180	180	180	180	180	180	180	180
a_2	120	120	120	120	120	120	120	120
a_3	90	90	90	90	90	90	90	90
a_4	10	10	10	10	10	10	10	10
a_5	−10	−10	−10	−10	−10	−10	−10	−10
a_6	−90	−90	−90	−90	−90	−90	−90	−90
a_7	−120	−120	−120	−120	−120	−120	−120	−120
a_8	−180	−180	−180	−180	−180	−180	−180	−180

(b) To shift beam 80° from broadside

	b_1	b_2	b_3	b_4	b_5	b_6	b_7	b_8
a_1	180	180	180	180	180	180	180	180
a_2	130	130	130	130	130	130	130	130
a_3	90	90	90	90	90	90	90	90
a_4	10	10	10	10	10	10	10	10
a_5	−10	−10	−10	−10	−10	−10	−10	−10
a_6	−90	−90	−90	−90	−90	−90	−90	−90
a_7	−130	−130	−130	−130	−130	−130	−130	−130
a_8	−180	−180	−180	−180	−180	−180	−180	−180

Feeding the angles shown in Tables 5.4 and 5.5 and applying post processing to the solutions in HFSS, the steered radiation patterns of the antenna were obtained. Fig.5.35 shows the 2D polar plot representing the gain radiation pattern obtained on simulation which is obtained by varying θ when $\phi = 0°$, since this represents the principal E-plane of the antenna. When all sources are provided with a phase of 0°, the radiated beam of the antenna points in the $\theta = 0°$ indicating that the radiation is maximum in the broadside. Next, the angles given in Table 5.4 (a) were assigned to the individual respective elements in the array and the main beam deflected 30° from the Z axis. Similarly, providing the sources with angles from Table 5.4 (b), the main beam was directed 45° from Z axis. Hence, by applying phases from Table 5.4 and 5.5 we can direct the beam at angles 60°, 70° and 80° from Z axis. Fig.5.36 represents the 3D polar plot showing the far field radiation pattern in terms of gain in dB

achieved by the proposed antenna structure. As mentioned earlier, the coefficients of the array factor obtained on calculation do not affect the sidelobe levels of the radiation pattern. Hence, in order to observe the behavior of the radiated beam, the gain of the radiation pattern is observed in linear scale. The maximum gain exhibited by the antenna at broadside is $-1.3dB$. As the beam moves away from the Z axis, the gain starts decreasing. The lowest gain exhibited by the antenna is $-19dB$ near the horizon, observed at θ=80°. From Fig.5.36, it can also be observed that as the beam approaches the plane of the antenna, the level of side lobes in the negative X direction increases. This can be ignored since the electrically small phased array antenna can achieve beam steering from broadside all the way to the plane of the antenna which is very difficult for a traditional patch antenna array.

The effects of embedding metamaterials in the simple patch antenna topology have been discussed so far. Two metamaterial structures, split rings and spiral resonators with capacitively loaded strips have been used as substrates in the microstrip antenna topology. Placing multiple meta-material unit cells between metal patch and a sufficiently large ground plane, resulted in an antenna structure that can be referred to as electrically small. The resulting antenna structures have achieved more than 70% reduction in their physical dimensions. The patch antennas discussed in this chapter are known to radiate off-broadside. Employing this concept, an electrically small phased array patch antenna which radiates at 200MHz has been developed. The quarter wavelength array is a planar structure of 64 elements. A combination of spiral metamaterial cells and FR-4 epoxy dielectric slab formed the substrate for the patches. A total of 192 spiral resonators with CLS have been integrated in the substrate beneath the patch. The location of these unit cells play an important role in controlling the input impedance of the antenna. The resulting antenna structure radiates broadside and each indiviual element of this array has been provided with progressive phase shifts to steer the main beam off broadside. The phased array an-

tenna thus designed is capable of electrically steering the main beam from broadside toward the plane of the antenna.

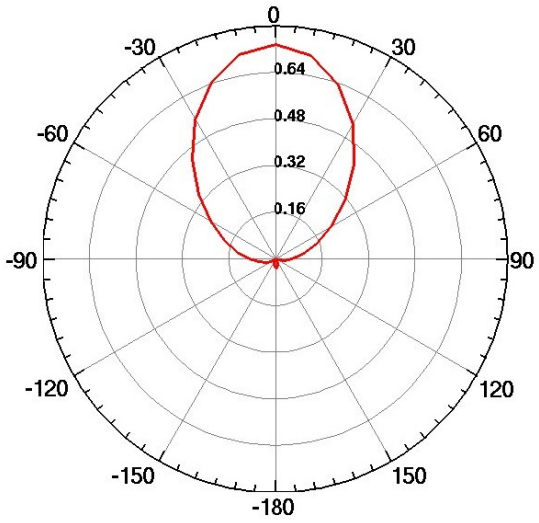

(a) Beam pointing in $\theta = 0°$

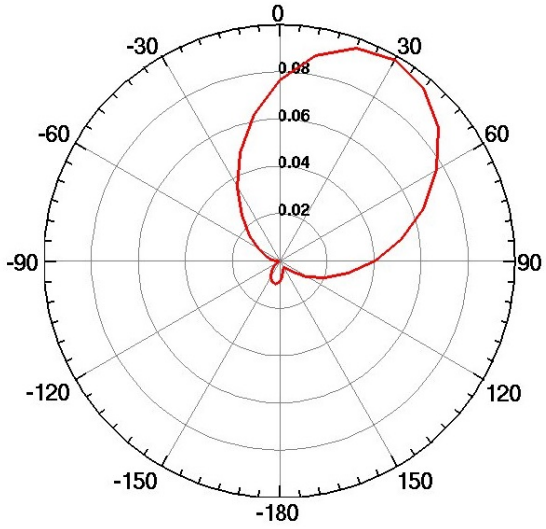

(b) Beam steered to $\theta = 30°$

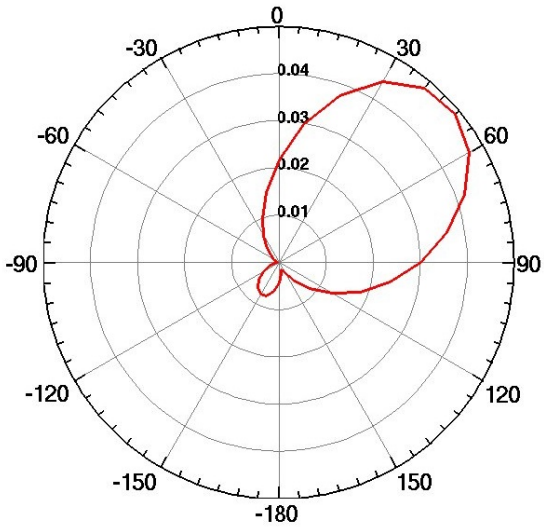

(c) Beam steered to $\theta = 45°$

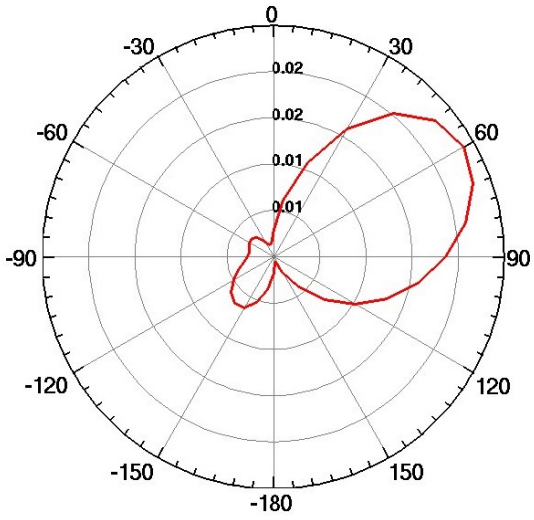

(d) Beam steered to $\theta = 60°$

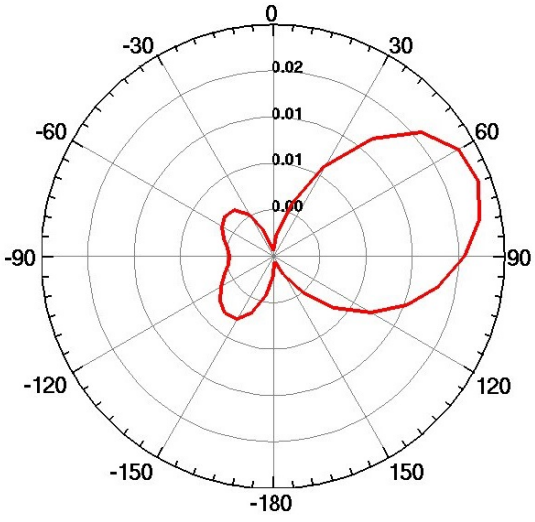

(e) Beam steered to $\theta = 70°$

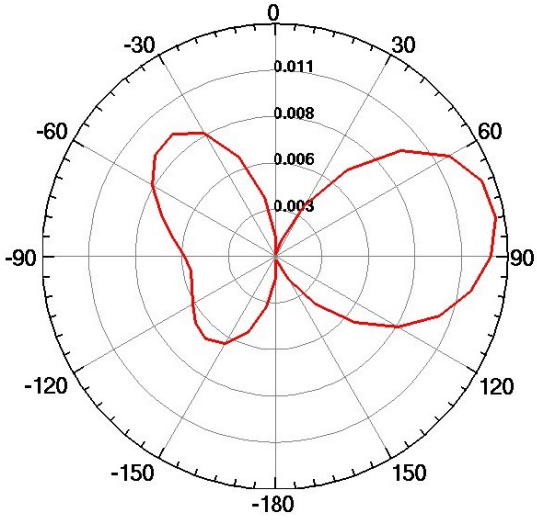

(f) Beam steered to $\theta = 80°$

Figure 5.35: 2D polar plot plot of radiation pattern in $\phi = 0°$ plane

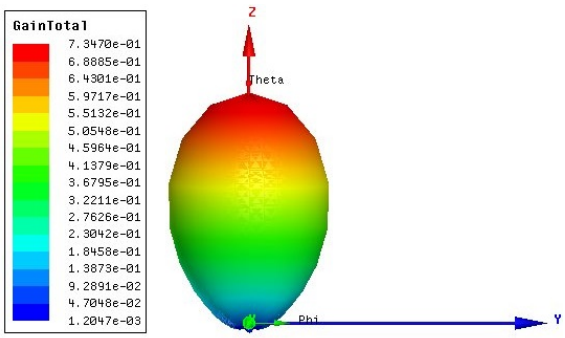

(a) Beam radiating in broadside

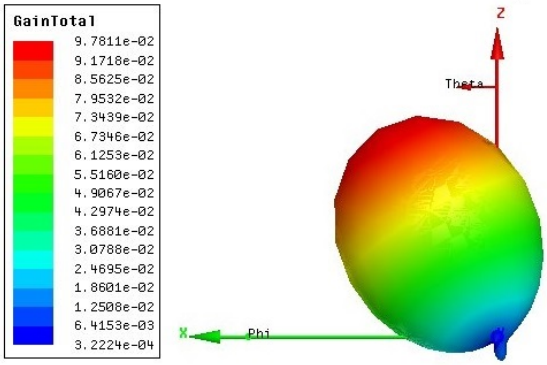

(b) Beam steered at $\theta = 30°$ off broadside

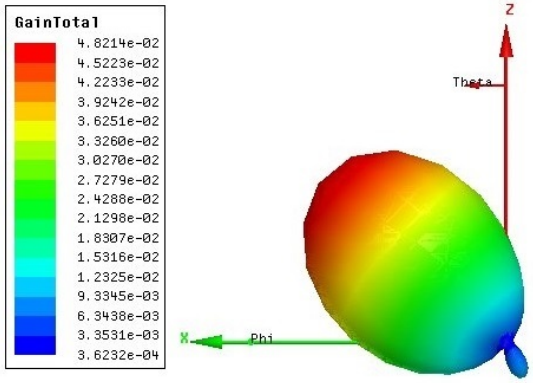

(c) Beam steered at $\theta = 45°$ off broadside

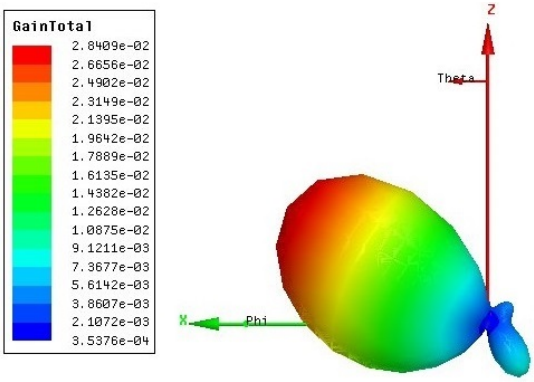

(d) Beam steered at $\theta = 60°$ off broadside

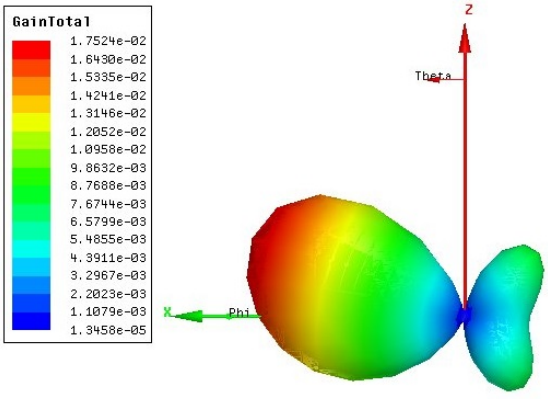

(e) Beam steered at $\theta = 70°$ off broadside

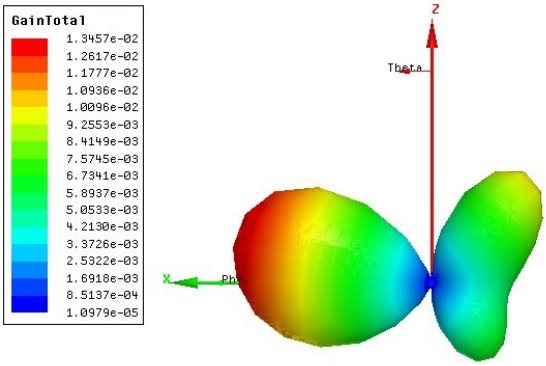

(f) Beam steered at $\theta = 80°$ off broadside

Figure 5.36: 3D polar plot showing gain (linear scale) of far field radiation with varying θ when ϕ=0°

CHAPTER 6: CONCLUSIONS

6.1 Summary of Developed Metamaterials

In this thesis research, two types of metamaterial structures were designed and discussed in detail. The first structure that is proposed is a double square split ring resonator, which is two concentric square shaped split ring resonators placed on an FR-4 epoxy dielectric substrate. The lengths of the rings and the gap between the two rings were optimized to achieve the desired resonant frequency. Additional capacitance of 4.7pF were added to the gaps in each ring to attain resonance at 300MHz. The designed structure was placed in a parallel plate waveguide in order to extract the relative permittivity and permeability exhibited by the proposed unit cell. At 300MHz, the split ring resonator metamaterial exhibited a strong negative permeability at 300 MHz.

The second structure that was designed was a combination of spiral rings having multiple turns and a vertical strip that was either shorted at both ends or capacitively loaded. A single sided metamaterial structure comprised of a spiral trace of ten turns and a vertical trace, which was modified to obtain variations in the behavior of permittivity exhibited by the structure. The first version of the spiral metamaterial cell consisted of a capacitively loaded vertical trace. The vertical trace was shorted at one of its ends to the PEC wall of the parallel plate waveguide. A small gap was introduced between the other end of the trace and the second PEC wall. The structure attained multiple resonances and negative permittivity was observed at these frequencies. Negative permeability was observed around the lowest resonant frequency. In the second version of the spiral metamaterial, the vertical trace was

shorted at both ends to the two PEC walls of the rectangular waveguide. A very wide band negative permittivity was obtained over most of the simulated frequency range. A small negative permeability was also observed near the lowest frequency of resonance. The last version of the spiral resonator unit cell consisted of a vertical trace that was not shorted at either ends. As such, the structure did not exhibit negative permittivity. However, a weak negative permeability was observed close to 300MHz. The first version of spiral metamaterial was chosen to be used as a replacement for dielectric substrate. This proposed metamaterial cell was further modified in dimensions to shift the resonance of the structure closer to 200MHz.

6.2 Summary of Developed Electrically Small Patch Antennas

Metamaterial unit cells designed in Chapter 4 have been used in a patch antenna structure to achieve miniaturization. The metamaterials were sandwiched between a metal patch and a ground plane. The dimensions of the patch and location of the metamaterials beneath the patch were optimized to achieve resonance at subwavelength frequencies.

The double split ring resonator and the spiral resonator structure were loaded into a patch antenna as substrates. The metamaterials were sandwiched between a metal patch and a ground plane. The antenna structures were fed with a coaxial cable. The first proposed design consisted of two split ring resonators placed under one of the radiating slots of the patch antenna. The dimensions of the patch and location of the probe feed point is optimized to obtain a good return loss. The resulting dimension of the patch at which sub resonance was achieved at 300MHz was 84mm×58mm. In order to improve matching, the distance between the split rings under the patch was reduced and the width was increased to 60mm, thus a return loss -21.6dB was achieved. The proposed antenna design loaded with split ring resonator structures exhibited a radiation pattern that deviated from broadside. The negative permeability possessed by the split ring structures push the main beam of the antenna away from

broadside. The antenna also showed a second resonance at a higher frequency that was satisfied by the actual dimensions of the antenna. The lower resonant frequency corresponds with the resonance of the split ring resonators and was referred to as subwavelength resonant frequency. This subwavelength resonance mode exhibited by the patch antenna was extremely narrow band and very poorly matched.

The second proposed design used spiral resonator structures with capacitively loaded strip with a combination of air as substrate for the patch antenna structure. When the dimensions of the patch were 65mm×60mm, three resonant frequencies were obtained between 0.1 and 1 GHz, which corresponded with the resonance of the spiral structure under the patch. The spiral structure excites a modified TM mode in the cavity of the patch to achieve these resonant frequencies. The dimensions of the patch and location of feed point were optimized to improve the return loss of the antenna. It was observed that at lowest resonant frequency, the antenna radiated off broadside and in the direction away from the vertical trace of the split rings. At the second and third frequency points, the antenna radiation pattern was omnidirectional and resembled that of a monopole antenna. Similar radiation patterns were observed when the distance between the spiral resonators was reduced. However, at the second and third resonant frequencies, the radiation patterns were more directional and pointing in the positive Y direction, away from the location of metamaterials. The antenna at these subwavelength frequencies appeared poorly matched with the reactive component decreasing as the resonant frequency increased.

This concept of loading a patch antenna with a spiral resonator structure metamaterial cell was extended to a design an electrically small phased array antenna that operates at 200 MHz. The entire antenna array structure was built on a ground plane that was half wavelength long (750mm). The patch size was fixed at 50mm×50mm and the interelement spacing between neighboring patches was 75mm. Since the array structure could not be drastically modified in dimensions, three metamaterial

structures were employed instead of two. The substrate used under the patch was a combination of FR-4 epoxy slabs and three spiral resonators. The three cells were placed close to each other under one radiating slot of the patch. Upon simulation, it was observed that a single element of the array radiated straight at broadside, as in a typical patch antenna.

The single element designed was then arranged in the X-Y plane to form an 8×8 planar antenna array structure. The gain of this 64 element antenna array was observed to be significantly higher than the gain of a single antenna element. The main beam of the antenna was then electrically steered. To steer the main beam off broadside, the elements of the antenna have to be fed with appropriate progressive phases. The distance between elements in proposed design of the patch antenna array is $\lambda/20$. This causes a high amount of mutual coupling between elements. Upon feeding the individual elements of the array with appropriate phases, the main beam could be successfully steered from broadside all the way to the horizon.

The antenna structures that were designed with metamaterials behaving as substrates were seen to achieve more that 75% reduction in size resulting in a very electrically small antenna structure. The proposed strcutures exhibited very small gain due to its small aperture size and maximum radiation was obtained in off-broadside directions. The subwavelength frequencies of the antenna were very narrowband and difficult to match. Metamaterial loading of the patch antenna structure enabled the patch to behave as a multiband antenna. The desired resonant frequency could be achieved by appropriately designing the metamaterial cell that is to the embedded into the patch antenna structure. The proposed patch antenna structures could produce radiation that was directed off broadside and also toward the horizon, which is difficult to obtain in a tradiational patch antenna.

REFERENCES

[1] *Antennas: Theory and Practice.* John Wiley & Sons, Inc., New York, 1952.

[2] *Small Antenna Handbook.* John Wiley & Sons, Inc., 2011.

[3] Constantine A.Balanis. *Antenna Theory, Analysis And Design, 3rd Ed.* John Wiley and Sons, Inc, 2005.

[4] Dr. Ryan S. Adams. Antennas, ECGR 4121/5121, Spring 2014. Lecture notes on microstrip patch antenna, University of North Carolina, Charlotte.

[5] Andrea Alù, Filiberto Bilotti, Fellow Nader Engheta, and Lucio Vegni. Subwavelength, compact, resonant patch antennas loaded with metamaterials. *IEEE transaction on antennas and propagation*, 55(1), 2007.

[6] B. A. Anicin. Reading hertz's own dipole theory. *European Journal of Physics*, 29.

[7] Juan D. Baena, Ricardo Marques, and Francisco Medina. Artificial magnetic metamaterial design by using spiral resonators. *Physical review B 69, 014402 (2004)*, 2004.

[8] Juan Domingo Baena, Jordi Bonache, Ferran MartÃn, Ricardo MarquÃ©s Sillero, Francisco Falcone, Txema Lopetegi, Miguel A. G. Laso, Joan GarcÃ-aâGarcÃa, Ignacio Gil, Maria Flores Portillo, and Mario Sorolla. Equivalent-circuit models for split-ring resonators and complementary split-ring resonators coupled to planar transmission lines. *IEEE Transaction on Microwave Theory and Techniques*, 53.

[9] Marek Bugaj, Rafal Przesmycki, Leszek Nowosielski, and Kazimierz Piwowarczyk. Analysis of different methods of microstrip antennas feeding for their electrical parameters. *PIERS Proceedings, Kuala Lumpur, Malaysia*, 2012.

[10] Jun-Chia Chen, Chang Hua Hsien, Hsiang-Jui Lin, and Kaohsiung Hsien. Planar inverted F antenna.

[11] G.A. Deschamps. Microstrip microwave antenna. *Presented at the Third USAF Symposium on Antennas*, 1953.

[12] Ansys Inc. Introduction to ansys hfss, 2014. Training Manual.

[13] Winston E. Kock. Metal-lens antennas. *Proceedings of the I.R.R and Waves and Electrons*, 34, 1946.

[14] Yoonjae Lee and Yang Hao. Characterization of microstrip patch antennas on metamaterial substrates loaded with complimentary split ring resonator. *Microwave and optical technology letters*, 2007.

[15] L.G.Chu. Physical limitation of omnidirectional antennas. *Jornal of Applied Physics*, 19(1163).

[16] Ismo V. Lindell, Ari H. Sihvola, and Juhani Kurkijarvi. Karl f. lindman: The last hertzian, and a harbinger of electromagnetic chirality. *IEEE Antennas and Propagation Magazine*, 34(3), 1992.

[17] M.R.C. Mahdy, M.R.A. Zuboraj, A.A.N. Ovi, and M.A Matin. A novel design algorithm and practical realization of rectangular patch antenna loaded with sng metamaterial. *Progress in Electromagnetic Research*, 17.

[18] H.A. Majid, M.K.A. Rahim, and T. Masri. Microstrip antenna's gain enhancement using left handed metamaterial structure. *Progress In Electromagnetic Research*, 8:235–247, 2009.

[19] Merih Palandoken, Andre Grede, and Heino Henke. Broadband microstrip antenna with left-handed metamaterials. *IEEE transaction on antennas and propagation*, 57(2), 2009.

[20] Shyam S. Pattnaik, J.G. Joshi, and M.R. Lohokare. Electrically small rectangular microstrip patch antenna loaded with metamaterial. *IETE Journal of Research*, 56.

[21] J. B. Pendry, A. J. Holden, D. J. Robbins, and W. J. Stewart. Low frequency plasmons in thin-wire structures. *J. Phys.: Condens Matter*, 10, 1998.

[22] J. B. Pendry, A. J. Holden, D. J. Robbins, and W. J. Stewart. Magnetism from conductors and enhanced nonlinear phenomena. *IEEE transaction on microwave theory and techniques*, 47(11), 1999.

[23] David M. Pozar. Microstrip antennas. *Proceedings of the IEEE*, 80(1), 1992.

[24] Walter Rotman. Plasma simulation by artificial dielectrics and parallel-plate media. *IRE Transaction on Antennas and Propagation*, January 1962.

[25] D.R. Smith, Willie J. Padilla, D.C. Vier, S.C. Nemat-Nasser, and S. Schultz. Composite medium with simultaneously negative permeability and permittivity. *Physical review letters*, 84(18), May 2000.

[26] D.R. Smith, W.J. Padilla, D.C. Vier, R. Shelby, S.C. Nemat-Nasser, N.Kroll, and S. Schultz. Left-handed metamaterials. *Photonic crystals and light localization*, 2000.

[27] Zsolt Szab*ó*, Gi-Ho Park, and Ravi Hegde. Metamaterial parameter extraction.

[28] Zsolt Szab*ò*, Gi-Ho Park, Ravi Hegde, and Er-Ping. A unique extraction of metamaterial parameters based on kramer's-kronig relationship. *IEEE Transaction on Microwave Theory and Techniques*, 58(10), 2010.

[29] V.G. Veselago. The electrodynamics of substances with simultaneously negative values of ϵ and μ. *Soviet physics Uspekhi*, 10(4), 1968.

[30] Martin Wegener and Nikolay I. Zheludev. Artificial chiral materials. *Journal of Optics A:Pure and Applied Optics*.

[31] Harold A. Wheeler. Small antennas. *IEEE transaction on antennas and propagation*, AP-23(11), 1975.

[32] Richard W. Ziolkowski. Design, fabrication, and testing of double negative metamaterials. *IEEE Transaction on Antennas and Propagation*, 51(7), 2003.